

Development and application of a hydrometeor
classification method for X-band polarimetric radar
focusing on solid hydrometeors

KOUKETSU, Takeharu

Development and application of a hydrometeor
classification method for X-band polarimetric radar
focusing on solid hydrometeors

(固体降水粒子を対象とした X バンド偏波レーダー用降水
粒子判別法の開発と適用)

KOUKETSU, Takeharu

(瀨瀬 丈晴)

Doctor of Science

Graduate School of Environmental Studies, Nagoya University

(名古屋大学大学院環境学研究科 博士 (理学))

2017

Abstract

To understand precipitation mechanisms, the demand of hydrometeor classification (HC) method for X-band polarimetric radar (X-pol), which is suitable for observation of solid hydrometeors under moist environments producing little or no hail, is increasing. To realize such a demand, a fuzzy-logic-based HC method for X-pol is developed in this study. This HC method identifies the most likely hydrometeor at each radar sampling volume from eight categories: (1) drizzle, (2) rain, (3) wet snow aggregates, (4) dry snow aggregates (DS), (5) ice crystals (IC), (6) dry graupel (DG), (7) wet graupel (WG), and (8) rain–hail mixture. The HC method uses radar reflectivity Z_h , differential reflectivity Z_{dr} , specific differential phase K_{dp} , and correlation coefficient ρ_{hv} as its main inputs, and temperature with some consideration of relative humidity as supplemental information. Membership functions for polarimetric radar variables are tuned by combining previous studies, and those for temperature are newly developed by taking account of the temperature that solid hydrometeors melt, which varies with relative humidity.

The method is validated against ground and in situ observations of solid hydrometeors (DG, DS, and IC) under a moist environment. Two cases of simultaneous observational data from a ground-based imaging system and an X-pol plan position

indicator scan with low elevation angle for convective snow clouds in winter Hokuriku in 2009 are used to validate the HC method for DG and DS. The HC method correctly distinguishes DG and DS corresponding to the periods that DG and DS were dominantly observed by ground-based imaging system, respectively. As IC is rarely observed on the ground, the HC method is validated for DS and IC using three cases of simultaneous observations from a balloon-borne instrument (hydrometeor videoprobe: HYVIS) and an X-pol range height indicator scan directed towards the HYVIS for precipitating clouds in Baiu-period Okinawa in 2011 and 2012. The HC method reasonably distinguishes DS and IC in the height where DS and IC were actually observed by HYVIS, respectively. Through the validation, the HC method distinguishes effectively between DG, DS, and IC, and is therefore valid for HC under moist environments.

After the development, the HC method was applied to isolated summer thunderclouds to demonstrate its performance. For the demonstration, the relationship between cloud-to-ground (CG) lightning polarity and the space–time distribution of solid hydrometeors for isolated summer thunderclouds in Japan is examined using the X-pol. HC was conducted to examine the space–time distribution of solid hydrometeor volumes for DS, IC, DG, and WG in thunderclouds. Two thunderclouds with different

composition of CG polarity were selected for analysis: 26 July 2010, which generated few positive CG strikes, and 25 August 2010, which generated positive CG strikes in the reflectivity cores. In both cases, negative CG strikes were observed in all reflectivity cores when a large volume of DG was identified above the -10°C level. This fact is consistent with previous studies showing that graupel particles have a negative charge below temperatures of -10°C . To focus on graupel particles, which play key role on electrification of the thunderclouds, solid hydrometeor distribution in reflectivity cores of the thunderclouds were examined. This analysis revealed that reflectivity cores with positive CG strike(s) had a large volume of DG up to high altitudes (around or above the -45°C level). Further, reflectivity cores that sustained large DG volumes at high altitudes had a relatively large number of positive CG strikes. The top height of the DG volume in reflectivity cores without positive CG strikes did not reach higher altitude (around or above than -45°C level) compared with those with positive CG strikes. These results suggest that the persistence of graupel particles in reflectivity cores at high altitude is a necessary condition for positive CG strikes in summer thunderclouds. This effect would be caused by the positively charged graupel particles under high rime accretion rates. The demonstration of HC for summer thunderclouds shows that the performance of the HC method is appropriate for examining solid hydrometeor

distributions.

Form the development and application parts, it is shown that the HC method effectively identifies solid hydrometeors (DS, IC, and DG) and is appropriate for examining hydrometeor distributions in summer thunderclouds. Thus, the HC method for X-pol is an useful tool for examining precipitation mechanisms associated with solid hydrometeors. The HC method will provide better understandings of severe weather associated with solid hydrometeors under moist environments providing little or no hail. In the near future, polarimetric radar observations with spatially and temporally higher resolution than today will be realized operationally and the HC method is expected to be applied to such high resolution observations.

Contents

1. Introduction	1
1.1. Polarimetric radar variables	2
1.2. Overview of HC method history	6
1.3. Necessity of HC method for X-pol	8
2. Observation with the Nagoya University X-pol	14
2.1. Data processing	14
2.2. Observation for validation and application	15
2.2.1. Observation in Hokuriku for ground validation	15
2.2.2. Observation in Okinawa for in situ validation	15
2.2.3. Observation in Tokai for application	16
3. Development of an HC method for X-pol	17
3.1. Reconstruction of HC components	17
3.1.1. Input variables	17
3.1.2. Hydrometeor categories	18

3.1.3. Membership functions	19
3.1.3.1. Radar variables	20
3.1.3.2. Temperature	22
3.1.4. Inference	24
3.1.5. Output	25
3.2. Validation focus points	25
4. Validation of the HC method	27
4.1. Validation method	27
4.1.1. Graupel and snow aggregates	27
4.1.2. Snow aggregates and ice crystals	30
4.2. Validation results	31
4.2.1. Graupel and snow aggregates	31
4.2.2. Snow aggregates and ice crystals	34
5. Application the HC method to summer thunderclouds	37
5.1. Background of thunderclouds	37
5.2. Observation of summer thunderclouds	42

5.2.1. Instruments	42
5.2.2. Analytical method	43
5.3. Overview of the summer thunderclouds	45
5.3.1. Case A: 26 July 2010	46
5.3.2. Case B: 25 August 2010	47
5.4. Reflectivity cores	49
5.4.1. Reflectivity cores A1	50
5.4.2. Reflectivity cores B2	51
5.4.2. Reflectivity cores B4	53
 6. Discussion	 55
6.1. Validity of the HC method	55
6.2. Validity of the validation of the HC method	56
6.3. Performance of the HC method	57
 7. Summary and conclusions	 62
 Acknowledgements	 67

References	69
-------------------------	-----------

Tables and Figures	80
---------------------------------	-----------

1. Introduction

Weather radar is a remote sensing tool to detect precipitation areas and measure the intensity of the precipitation systems. It has been used since just after the World War II and has revealed the structures of precipitation systems (e.g., Workman and Reynolds 1948; Reynolds and Brook 1956). Later, Doppler weather radar was developed in order to observe the airflow in precipitation systems. For estimation of rainfall rate and examination of hydrometeor distribution in precipitation system, polarimetric radar has been developed in the last three decades. It provides information of microphysical properties of hydrometeor (size, shape, canting angles, and so on) as polarimetric radar variables, and thus notable improvement of quantitative precipitation estimate and deducing hydrometeor types.

To comprehend the structures of precipitation systems, observation of hydrometeor distribution is needed. Conventional weather radar only provides rough information of precipitation intensity but it does not provide the information of the hydrometeor type and its distribution. Polarimetric radar has the ability of discrimination of hydrometeor types by obtaining microphysical information of hydrometeors (size, shape, canting angles, and so on) from polarimetric radar variables. This information is very useful especially in severe weather (e.g., lightning and hail falling), which is often brought by precipitation system containing different types of solid hydrometeors. Thus, the hydrometeor classification (HC) from polarimetric radar variables is an important subject to understand precipitation mechanisms. To cover solid hydrometeors including snow aggregates and ice crystals, which are a little difficult to observe with longer

wavelength radar (S- or C-bands), the demand of HC for X-band polarimetric radar (X-pol) is increasing. To realize this demand, development of a new HC method for X-pol is the subject of this study.

For the basis of developing the HC method, polarimetric radar variables are briefly introduced first. Then, history of HC is overviewed, and the recent necessity of HC method for X-band polarimetric radar (X-pol) and the purpose of this study are given.

1.1 Polarimetric radar variables

There are several kinds of hydrometeors with various shapes: raindrop, snow aggregates, ice crystals, graupel and hail. For raindrops, small sized one (drizzle) is almost spherical by its surface tension. As raindrop becomes larger, it has more oblate shape because of large air resistance coming from its large fall velocity (e.g., Beard and Chuang 1987). Snow aggregates have quasi-isotropic shapes consisting of ice crystals, which have various ice habits: plate, column, needle, and dendrite (e.g., Magono and Lee 1966; Kikuchi et al. 2013). Graupel particles have lump, conical, and hexagonal shapes with various aspect ratios (Knight and Knight 1973; Locatelli and Hobbs 1974). Hailstones have more irregular shapes; some has conical shape and other has lobed shape.

The conventional radar utilizes single polarimetric wave, with which cannot distinguish particle shapes, to measure radar reflectivity Z (unit in dBZ) for each radar sampling volume assuming Rayleigh scattering:

$$Z = 10\log_{10}z \quad (1)$$

$$z = \int D^6 N(D) dD \quad (2)$$

where, z is radar reflectivity factor in unit of $\text{mm}^6 \text{m}^{-3}$, D is diameter of hydrometeor in mm and $N(D)$ is number concentration of hydrometeor ($\text{mm}^{-1} \text{m}^{-3}$) with diameter D in the radar sampling volume. Thus, the radar enables us to roughly estimate hydrometeor mass and precipitation intensity.

In contrast with conventional radar, polarimetric radar measures the intensity of precipitation with dual polarized waves and obtains polarimetric radar variables, which give us the microphysical information of hydrometeors: shape, canting angle, and homogeneity. Among the polarimetric radar variables, differential reflectivity (Z_{dr}), differential propagation phase shift (ϕ_{dp}), specific differential phase (K_{dp}), and correlation coefficient between horizontally and vertically polarized wave signals (ρ_{hv}) have been widely utilized to examine the microphysical structures of precipitating clouds.

The differential reflectivity Z_{dr} (unit in dB) is defined as

$$Z_{\text{dr}}(r) = 10 \log_{10} \left[\frac{z_h(r)}{z_v(r)} \right] \quad (3)$$

where $z_h(r)$ and $z_v(r)$ is radar reflectivity factors of horizontal and vertical waves (units in $\text{mm}^6 \text{m}^{-3}$), respectively, at the distance of the radar sampling volume from the radar r . The value of Z_{dr} gives us the information of averaged hydrometeor shape weighted by sixth power of diameter. If the averaged hydrometeor shape is oblate (horizontally long), the value of Z_{dr} becomes positive because $z_h > z_v$ in Eq. (3) for oblate hydrometeor. If hydrometeor is prolate (vertically long), the value of Z_{dr} becomes negative. If

hydrometeor is isotropic, the value of Z_{dr} is zero. For raindrops, the value Z_{dr} becomes positively larger value as raindrops become larger and consequently, their shape becomes more oblate (e.g., Wakimoto and Bringi 1988; Thurai et al. 2007).

The differential propagation phase shift φ_{dp} (unit in $^{\circ}$) at the distance of r of the radar sampling volume from the radar is defined as

$$\varphi_{dp}(r) = \varphi_h(r) - \varphi_v(r) \quad (4)$$

where, $\varphi_h(r)$ ($^{\circ}$) and $\varphi_v(r)$ (unit in degree) are phase shift of horizontally and vertically polarized waves, respectively, through the propagation in air containing hydrometeors from the wave that would propagate in in the vacuum space. If oblate hydrometeors are dominant in the path of the propagation, horizontally polarized wave “slows down” relative to vertically polarize wave, which produces phase shifts as $\varphi_h > \varphi_v$, and the value of φ_{dp} increases monotonically with the distance from the radar.

The value of φ_{dp} is utilized as specific differential phase (K_{dp} , unit in $^{\circ}\text{km}^{-1}$) by differentiating with respect to distance:

$$K_{dp}(r) = \frac{d\varphi_{dp}(r)}{dr} \quad (5)$$

where r is the distance of the radar sampling volume from the radar. The value of K_{dp} is proportional to mass (third power of diameter, bulk density, and number concentration) and the value of $1-r_{ax}$ of hydrometeors in the radar sampling volume, where r_{ax} is the particle axis ratio (vertical/horizontal length dimension ratio). For raindrops, K_{dp} can be written as

$$K_{dp} = \left(\frac{180}{\lambda}\right) 10^{-3} CW(1 - \bar{r}_{ax_m}) \quad (6)$$

where $C \approx 3.75$ is both dimensionless and independent of radar wavelength λ , W is liquid

water content (g m^{-3}), and \bar{r}_{ax_m} is mass-weighted mean axis ratio (Bringi and Chandrasekar 2001, in their Eq. (7.17)). Similarly, K_{dp} can be written for ice particle as

$$K_{dp} = \left(\frac{180}{\lambda}\right) 10^{-3} C' \rho_p (\text{IWC})(1 - r_{ax}) \quad (7)$$

where $C' \approx 1.6 (\text{g m}^{-3})^{-2}$, IWC is ice water content (g m^{-3}), and the aspect ratio r_{ax} and density ρ_p (in g cm^{-3}) of particles are assumed to be independent of particle size (Bringi and Chandrasekar 2001, in their Eq. (7.101)). Thus, K_{dp} becomes larger positive value as mass (W or IWC) and oblateness (the value of $1-r_{ax}$) of particles becomes larger.

The correlation coefficient between horizontally and vertically polarized wave signals (ρ_{hv}) is expressed as

$$\rho_{hv}(r) = \frac{|\langle n S_{hh} S_{vv}^* \rangle|}{\langle n |S_{hh}|^2 \rangle^{\frac{1}{2}} \langle n |S_{vv}|^2 \rangle^{\frac{1}{2}}} \quad (8)$$

where S_{hh} and S_{vv} are signal intensity of horizontally and vertically polarized wave, respectively, and these in an angle bracket with n represent an expectation weighted by the number of particle. The value of ρ_{hv} depends on the shape, canting angle, and phase of particles. If particles in the radar sampling volume is homogeneous (e.g., drizzle), the value of ρ_{hv} becomes close to 1.0. In contrast, in the melting layer or hail shaft, where hydrometeor have irregular shape, random orientation and/or mixed phase, the value of ρ_{hv} decreases down to around 0.8.

Polarimetric radar variables described above can be utilized in various kinds of research. For example, the drop size distribution can be estimated using the information of raindrop shape from Z_h , Z_{dr} and K_{dp} (e.g., Seliga and Bringi 1976, 1978). This provides accurate quantitative estimation of precipitation intensity (e.g., Sachidananda

and Zrnić 1986; Gorgucci et al. 1994). Zero or negative Z_{dr} and K_{dp} in large reflectivity area can be used for hail detection (e.g., Aydin et al. 1986). The decrease of ρ_{hv} is indicator of melting layer or hail shaft.

Combination of microphysical information from polarimetric radar variables described above enable for us to deduce hydrometeor type in precipitating clouds by HC. Because polarimetric radar variables depends on wavelength of radar (e.g., inversely proportion of K_{dp} , as in Eqs. (6) and (7), and irregular values of Z_h and Z_{dr} by Mie scattering from large particles with respect to the wavelength), it is necessary to develop HC method for each radar wavelength. In the next subsection, HC history including development for radar wavelength is briefly reviewed in the following subsection.

1.2. Overview of HC method history

Polarimetric radar has been used for HC during the past three decades. In the early days of HC history, hydrometeor type was deduced roughly from polarimetric measurements. For example, Hall et al. (1980) showed the roughly expected range of Z_h and Z_{dr} values for several types of rain and hail as “large or small” and “positive or negative” in their Table 1. As time passes, the range of polarimetric radar variables became more specific by accumulation of knowledge from observations and scattering calculation of polarimetric radar variables (e.g. Hall et al. 1984). Based on these knowledge, the decision tree method with predefined boundaries of polarimetric measurement values was widely utilized for HC in 1990s (e.g., Doviak and Zrnić 1993; Straka and Zrnić 1993; Höller et al. 1994; López and Aubagnac 1997). One of them,

Doviak and Zrnić (1993) listed up the range of polarimetric radar variables for 10 hydrometeor categories, including rain, snow aggregates, ice crystals, graupel, and hail in their Table 8.1. The table was widely referred in literatures of HC studies.

For the last two decades, fuzzy-logic-based HC methods have been developed (e.g., Straka 1996; Vivekanandan et al. 1999; Liu and Chandrasekar 2000, hereafter, L00; Lim et al. 2005). As noted in L00, hydrometeor type identification from radar observations cannot be obtained as a simple lookup table because the polarimetric radar signature for different hydrometeors is not mutually exclusive and unique. To overcome this problem, a fuzzy logic technique is well suited for HC due to its ability to identify hydrometeor types with the overlapping and noisy measurements (Chandrasekar et al. 2013).

The key component of fuzzy-logic-based HC method is membership function (MBF). MBFs convert the precise input radar measurements to fuzzy sets with corresponding membership degree (L00), which corresponds to the degree of existence possibility of a certain hydrometeor for the input variable. Thus, it is necessary to specify a total of *(the number of input radar variables) \times (the number of output hydrometeor categories)* MBFs. By considering membership degree from MBFs, fuzzy-logic-based HC have ability to reach distinct decisions based on "overlapping" and "noise contaminated" data (L00). Because of this robustness, fuzzy-logic-based HC methods are widely used recently and the framework of them is followed in this study. The details of the fuzzy-logic-based HC components are described in subsection 3.1.

As mentioned previous subsection, the polarimetric radar variables depend on wavelength of radar. Thus, it is necessary to develop MBFs for every wavelength. For

longer wave lengths (S- and C- bands), the MBFs were developed the early days of fuzzy-logic-based HC, often targeting hail detection. On the other hand, there were few MBFs for X-band because of attenuation of heavy precipitation and Mie scattering from hail. However, the demand of HC using X-band is increased because of the usefulness of X-pol, which covers solid hydrometeors with weak signals (e.g. snow aggregates and ice crystals) as well as rain and graupel. Thus, there appears HC method for X-pol recently (e.g., Dolan and Rutledge 2009, hereafter D09; Snyder et al. 2010, hereafter S10, Thompson et al. 2014).

1.3. Necessity of HC method for X-pol

Previous studies of HC have been conducted mainly in the United States, Europe, and Australia using S-band polarimetric radar (S-pol) (e.g., L00; Lim et al. 2005; Park et al. 2009) and C-band polarimetric radar (C-pol) (e.g., Keenan 2003; Marzano et al. 2006, 2008); the targets were mainly severe convective precipitation systems under continental dry environments, often producing hail. However, there have been few studies of HC or validations in the moist environments such as occur in East Asia.

Although hail is rarely observed in East Asia, as the convective available potential energy (CAPE) is low resulting in weaker updrafts, solid hydrometeors such as graupel, snow aggregates, and ice crystals exist above the freezing level. During the pre-summer rainy season, known as the “Baiu” period in Japan (Matsumoto et al. 1971; Ninomiya 1984; Ninomiya and Akiyama 1992), the sub-cloud layer is very moist. In such an environment, although cumulonimbi rarely develop into deep convection with radar

echo-tops reaching the tropopause, they sometimes extend above the freezing level by a few kilometers and contain solid hydrometeors (e.g., Oue et al. 2010). In fact, Suzuki et al. (2012, 2014) made in situ observations of graupel in the Baiu frontal zone using videosondes developed by Takahashi (1990). During the winter season, graupel as well as snow aggregates are observed on the ground in some regions, such as on the west coasts of Japan (Mizuno 1992).

Most HCs have been adjusted for S- and C-pols, because these radars are suitable for detection of hail regions in severe convective precipitation systems. For example, Doviak and Zrnić (1993) listed a range of possible values of S-pol measurements for 10 hydrometeor categories including hail, as mentioned in the previous subsection. Until several years ago, there were few studies of HC using X-band polarimetric radar (X-pol), mainly because of the non-Rayleigh scattering and significant attenuation of X-band radar, both of which are negligible for S-band radar (D09).

Compared with longer-wavelengths (S- or C-band), X-band radar has several advantages. Notably, it can observe smaller solid hydrometeors such as ice crystals up to a few millimeters in size, which are subject to Rayleigh scattering, than longer-wavelengths radars because the scattering cross section in the Rayleigh region is inversely proportional to the fourth power of wavelength (e.g., Doviak and Zrnić 1993). In addition, X-band radar has greater sensitivity of specific differential phase (K_{dp}) than longer wavelengths (e.g., D09; Bechini et al. 2013; Thompson et al. 2014) because the value of K_{dp} is inversely proportional to radar wavelength (Bringi and Chandrasekar 2001). These are useful properties for understanding microphysical processes in clouds

containing ice crystals. As X-band radar can also observe larger solid hydrometeors such as snow aggregates and graupel as effectively as S- or C-band radar, X-pol can be used for HC of solid hydrometeors under moist environments producing little or no hail.

Graupel, snow aggregates, and ice crystals have different sizes and densities, and so different fall velocities (Locatelli and Hobbs 1974; Khvorostyanov and Curry 2005; Ishizaka et al. 2013), and therefore contribute differently to the amount and horizontal distribution of solid precipitation on the ground. Graupel particles have high densities and fall velocities, resulting in heavy precipitation in localized areas. Snow aggregates drift with the wind and fall over a wider area because of their low densities and small fall velocities. Ice crystals have even lower fall velocities and contribute even less to precipitation amounts. Thus, it is very important to distinguish between graupel, snow aggregates, and ice crystals to understand the microphysical processes in precipitating clouds that contain solid hydrometeors. X-pol has the potential to identify the types and distributions of these solid hydrometeors.

In recent years, several HC methods for X-pol have been proposed, some of which are based on T-matrix scattering simulations. D09 developed a theory-based X-band HC method for several kinds of hydrometeors. They did not include melting snow and hail because of the associated significant attenuation and non-Rayleigh scattering. S10 conducted several kinds of attenuation correction and attempted HC for severe convective storms that produced hail. They adapted the S-pol HC method (Park et al. 2009) for use with X-pol based on disdrometer observations and T-matrix scattering simulations with idealized drop size distributions, and attempted to identify big drops,

light-to-moderate rain, heavy rain, and rain–hail mixture well below the freezing level. Al-Sakka et al. (2013) proposed an HC method that discriminates between rain, wet snow, dry snow, ice, and hail, for X-pol and also for C- and S-pol based on radar observations and T-matrix simulations. Thompson et al. (2014) used T-matrix and Mueller-matrix scattering models to create membership beta functions for X-, C-, and S-pol for various winter hydrometeors: plates, dendrites, aggregates, sleet, and rain. However, each of these studies was restricted to a small number of hydrometeor types and there is no HC method for X-pol that covers all the hydrometeors listed in HC methods for S-pol (e.g., Doviak and Zrnić 1993). Therefore, combining existing studies to reconstruct a unified HC method for X-pol covering all solid hydrometeors will help the classification of hydrometeors that are likely to exist under moist environments.

Once combined, the HC method must be validated. D09 and S10 validated their HC method indirectly by comparison with HC from S-pol data, assuming that the HC method for S-pol was correct. However, observational validation of the HC method for X-pol is still limited.

In this study, the goal is to develop an HC method for X-pol with validation using ground and in situ observations of solid hydrometeors, including graupel. Radar data for these validations were collected with X-pol of Nagoya University installed at different locations during successive campaigns, as described in Section 2. The HC method for X-pol is developed by reconstructing previous studies in Section 3 and validated it in Section 4. The validation of the HC method is conducted under a moist environment, using ground observational data in Hokuriku (west coast of Japan, Fig. 1b) during the

winter, where both graupel and snow aggregates are observed on the ground. Because ice crystals are rarely observed and therefore difficult to validate on the ground, balloon-borne in situ data in Okinawa (southwest Japan, Fig. 1c) during the Baiu period for validation of snow aggregates and ice crystals are also used for the validation.

After the development part with reconstruction and validation of the HC method, it is applied to summer thunderclouds to demonstrate its performance in Section 5. Summer thunderclouds are considered to produce cloud-to-ground (CG) lightning with their electrification via non-inductive charging mechanism; graupel particles and ice crystals collide and have opposite charge polarity (e.g., Takahashi 1978). The charging polarity of solid hydrometeors varies under the condition of temperature and cloud water content (or rime accretion rate), and it may control the polarity of CG lightning polarity. Thus, it is important to examine the relationship between solid hydrometeor distribution and lightning polarity in thunderclouds. For this purpose, the HC method in this study, which is validated for solid hydrometeors (snow aggregates, ice crystals, and graupel), is a valid tool to examine the relationship in summer thunderclouds. For the representative, two cases of summer thunderclouds with different composition of CG polarity in reflectivity cores are selected for the analysis; one had only negative CG lightning strikes in its reflectivity cores (case on 26 July 2010), which is typical summer thundercloud, and the other had some positive CG strikes in addition to negative ones.

After the demonstration of the HC method with application to summer thunderclouds, the validity of reconstruction, validation and application of the HC method for X-pol are discussed in Section 6. Finally, we present a summary and

conclusions in section 7.

2. Observation with the Nagoya University X-pol

In this study, X-pol of Nagoya University, which installed at different locations during successive campaigns (Fig. 1), was used for data collection for the validation and application. In this section, radar specifications and data processing are described in Section 2.1. Then, the observation site and operating mode of the X-pol for each observation for the validation and application are given in Section 2.2.

2.1. Data processing

The specifications of the Nagoya University X-pol are listed in Table 1. The X-pol can measure Z_h , Z_{dr} , K_{dp} , and ρ_{hv} , which are required for the HC. First, the radar sampling volumes with 1-km standard deviation of differential propagation phase shift greater than 30° are regarded as non-meteorological echo and excluded from the analysis (the threshold is determined empirically in order to include the melting layer but to exclude ground clutter). Then, the Z_{dr} bias is corrected using vertical (elevation = 90°) PPI or low elevation PPI for drizzle regions; Z_{dr} should be 0 dB under these conditions. The value of K_{dp} is calculated from differential propagation phase shift by piecewise linear regression using a least-squares fit over an interval that varies with the level of Z_h following the conventional algorithm described in Section 2 of Wang and Chandrasekar (2009):

$$\begin{cases} 11 \text{ bins (1.5 km)} & \text{for } 45 \text{ dBZ} \leq Z_h \\ 21 \text{ bins (3.0 km)} & \text{for } 35 \text{ dBZ} \leq Z_h < 45 \text{ dBZ} \\ 31 \text{ bins (4.5 km)} & \text{for } Z_h < 35 \text{ dBZ} \end{cases} \quad (9)$$

Once K_{dp} has been determined, Z_h and Z_{dr} are corrected for rainfall attenuation with K_{dp} following Jameson (1992). Also, ρ_{hv} is corrected using the SNR as described in the appendix of Shusse et al. (2009). To avoid noisy data, radar sampling volumes with SNR lower than 10 dB are excluded from the analysis.

2.2. Observation for validation and application

2.2.1. Observation in Hokuriku for ground validation

To explore the polarimetric characteristics of solid hydrometeors, polarimetric radar observation with the Nagoya University X-pol was conducted in Hokuriku District from December 2008 to February 2009. The X-pol was installed at Oshimizu (36.82°N, 136.76°E, Fig. 1b). Volume scans with 12 plan position indicator (PPI) scans at elevation angles from 0.6° to 20° were conducted every 5 minutes. The details of the Hokuriku Observation can be found in Ohigashi et al. (2014).

During the observation period, various types of solid hydrometeors were observed on the ground: wet (melting) snow, snow aggregates, and graupel. Data from the case of rain-to-snow transition from late night on 23 to the wee hours on 24 January 2009 was used for the verification of the performance of the HC method in discrimination between rain, wet snow and dry snow in its construction process in Section 3. For the validation of the HC method, snow and graupel falling cases in January and February 2009 were used as described in Section 4.

2.2.2. Observation in Okinawa for in situ validation

To examine the structures of precipitating clouds in pre-summer, Baiu-period,

polarimetric radar observation with the X-pol were conducted in Okinawa during the Baiu periods in 2011 and 2012 (Oue et al., 2015). The X-pol was installed at Aguni Island (26.58°N, 127.23°E, Fig. 1c). Volume scans with 15 PPI scans at elevation angles from 0.6° to 33.5° were conducted every 6 minutes and range height indicator (RHI) scans were conducted when the precise vertical observation of precipitating cloud was needed. For the validation of the HC method, precipitating clouds with snow aggregates and ice crystals above the freezing level in 2011 and 2012 Baiu-periods were used as described in Section 4.

2.2.3. Observation in Tokai for application

To examine the structures of precipitating clouds, the X-pol was deployed at Nagoya University (35.15°N, 136.97°E, Fig. 1d) from 2007 to 2011. Volume scans with 15 PPI scans at elevation angles from 0.6° to 33.5° were conducted every 6 minutes with some exception. To demonstrate the performance of the HC method, it was applied to isolated summer thunderclouds in July and August 2010, as described in Section 5.

3. Development of an HC method for X-pol

The existing framework of fuzzy-logic-based HC methods that have been widely used in the last two decades (e.g., Vivekanandan et al. 1999; L00; Keenan 2003; Lim et al. 2005; Park et al. 2009) is followed to construct an HC method for X-pol. After the description of the HC method in Section 3.1, the key validation points are listed in Section 3.2.

3.1. Reconstruction of HC components

The fuzzy-logic-based HC method in this paper has three major components: fuzzification, inference, and defuzzification (Lim et al. 2005; Chandrasekar et al. 2013). In the fuzzification part, input variables and hydrometeor categories for HC are selected, and membership functions (MBFs) for each hydrometeor and input variable are constructed using previous studies. Then, the inference and defuzzification (output) parts based on previous studies are described.

3.1.1. Input variables

Several variables measured by polarimetric radar have been used for HC of hydrometeor types in precipitating clouds: radar reflectivity for horizontally polarized waves, Z_h ; differential reflectivity, Z_{dr} ; linear depolarization ratio, LDR; specific differential phase, K_{dp} , and correlation coefficient between horizontally and vertically polarized signals, ρ_{hv} . All of them except for LDR are introduced in Section 1.1 and the details of these variables are discussed in Bringi and Chandrasekar (2001). The HC method uses four input radar variables: Z_h , Z_{dr} , K_{dp} and ρ_{hv} . The HC method is assumed

to be applied to each radar sampling volume, with range and azimuthal resolutions typically between one hundred to a few hundred meters and 1° to 1.5° , respectively. High elevation angles should be avoided because differential measurements, such as Z_{dr} and K_{dp} , depend on the viewing angle as mentioned by D09; they conducted scattering simulations for elevation angles of 1° and 30° . The HC method in this paper is designed for regions where the elevation angle is less than or equal to 30° .

The HC requires the temperature at the radar sampling volume or the altitude of the 0°C level to distinguish between liquid and solid hydrometeors. In this paper, vertical profiles of temperature for the HC are assumed to be available from soundings or numerical models.

3.1.2. Hydrometeor categories

Our goal was to develop an HC method for X-pol to identify solid hydrometeors under moist environments, including graupel, snow aggregates, and ice crystals. Although hail is rarely observed in moist environments, it is useful to include hail as a reference. Therefore, the list of hydrometeor categories in Doviak and Zrnić (1993) is followed except for hail categories. For the hail category, we follow S10, who attempted HC including hail using X-pol. The hydrometeor categories adopted in this study are (1) drizzle (DZ), (2) rain (RN), (3) wet snow aggregates (WS), (4) dry snow aggregates (DS), (5) ice crystals (IC), (6) dry graupel (DG), (7) wet graupel (WG), and (8) rain–hail mixture (RH). The WG category may contain some small hail as the polarimetric characteristics are similar and can be difficult to distinguish in radar observations (Straka et al. 2000; D09). Thus the WG category is assumed to consist of high density

particles that can be water-coated via wet growth or melting. Large hail or rain–hail mixture may have extremely large Z_h and low ρ_{hv} values that are different from those of WG. Thus the RH category is added in preparation for a possible future improvement of the HC method.

3.1.3. Membership functions

The determination of the MBF is an important part of the fuzzy-logic-based HC method. In this paper, the beta function β used by L00 is employed for the MBF:

$$\beta(x, a, b, m) = \frac{1}{1 + \left[\left(\frac{x - m}{a} \right)^2 \right]^b}, \quad (10)$$

where x is the input variable, and the three parameters are the half-value width a , the beta function slope b , and the midpoint m .

Having chosen the function type for the MBF, we determine the parameters in Eq. (10) for each input variable and hydrometeor type. The curvature of the beta function depends on the value of b in Eq. (10); the beta function becomes more step-function-like with larger b . Different values of b have been used in the previous studies and it is therefore difficult to determine the most suitable value. To avoid too wide a spread in the MBFs, which increases the overlap of MBFs for different hydrometeors, the values of b are empirically tuned. Consequently, $b = 12.6$, which sets $\beta = 0.01$ in Eq. (10) when $|x - m| = 1.2a$, is used for the four radar variables (Z_h , Z_{dr} , K_{dp} , and ρ_{hv}), except for the MBFs of Z_{dr} ($b = 27.9$) and K_{dp} ($b = 58.6$) for RN. Both of these MBFs have large a in Eq. (10), resulting in a wide spread in the MBFs. In the temperature MBFs, the value of a varies considerably with hydrometeor category and

the value of b ranges from 3.9 to 58.6, as listed in Table 2.

The determination of m and a in Eq. (10) is the main task in MBF construction. Previous studies have given the lower and upper thresholds of the range of polarimetric variables, corresponding to the values of $m - a$ and $m + a$, respectively, for various hydrometeors (e.g., Doviak and Zrnić 1993; Straka et al. 2000). In addition, some studies (e.g., Straka et al. 2000; Keenan 2003; Tessendorf et al. 2005) have given the lower and upper thresholds of the range of temperature. In this study, the thresholds of the radar variables and temperature are determined on the basis on previous studies (see Table 3), modifying them where necessary as described below.

3.1.3.1. Radar variables

To determine the lower and upper thresholds of MBFs of radar variables, we follow L00 (HC for S-band), Dolan et al. (2013, hereafter “D13”, C-band) and D09 (X-band), all of whom use beta functions for MBFs. The thresholds in L00 are close to those for S-pol listed by Doviak and Zrnić (1993). The thresholds in D13 and D09 are based on theoretical scattering simulations for C- and X-band, respectively. D09 pointed out that larger hydrometeors (for example, raindrops larger than 2 mm) are subject to the non-Rayleigh effect. This suggests that most solid hydrometeors, including large ice crystals, are in the non-Rayleigh regime. Therefore, D09 is broadly followed for the lower and upper thresholds (Fig. 2), except for RH and WS, which were not considered by D09. S10 (X-band) is followed for RH, choosing beta functions with the same half-value width as their trapezoidal MBFs, and L00 (S-band) is followed for WS except for K_{dp} because Al-Sakka et al. (2013) showed almost the same MBFs of WS for

S- and X-band based on real radar observations.

For Z_h (Fig. 2a), the lower and upper thresholds are relatively insensitive to wavelength. For DG, the lower thresholds of D13 (C-band) and D09 (X-band) are much lower than L00 (S-band). This is because D13 and D09 allow DG (referred to as “low-density graupel”) to have a minimum median volume diameter D_0 as small as 1.5 mm. Such small graupel particles are difficult to distinguish from snow aggregates because they have similar polarimetric characteristics: lower Z_h , near-zero Z_{dr} and K_{dp} , and high ρ_{hv} . In this study, graupel particles with D_0 larger than a few millimeters are identified as the hydrometeor category of “graupel”. Such graupel particles have relatively large fall velocities. Yamada et al. (2004) suggested that reflectivity cores with $Z_h \geq 30$ dBZ can contain such fast falling graupel, based on the descending speeds of reflectivity cores estimated from dual-Doppler radar observation. Thus, the value of 30 dBZ in Z_h is adopted as the lower threshold of DG. The Z_h value for WG should be larger than for DG because it has higher density and dielectric constant. Therefore, the lower threshold of Z_h for WG is set as 35 dBZ.

For Z_{dr} (Fig. 2b), the upper thresholds become higher at shorter wavelengths for large hydrometeors (RN and WG). For K_{dp} (Fig. 2c), D09 (X-band) is broadly followed. However, for IC, D09 assumed small sizes (up to 1.5 mm), whereas we intend the IC category to cover non-aggregated snow particles including dendritic particles, which can be up to several millimeters in size and have the largest value of K_{dp} of the non-aggregated snow particles. Large K_{dp} values corresponding to dendritic particles have been reported by Kennedy and Rutledge (2011) (up to $0.4^\circ \text{ km}^{-1}$ with S-pol, which

corresponds to $\sim 1.5^\circ \text{ km}^{-1}$ with X-pol) and Bechini et al. (2013) (more than 3° km^{-1} with X-pol). Therefore, the upper threshold of IC is increased to $1.5^\circ \text{ km}^{-1}$ in this study. For WS, L00 is followed, assuming the K_{dp} values are inversely proportional to the wavelength. For ρ_{hv} (Fig. 1d), L00 for WS, S10 for RH, and D09 for the other hydrometeors are simply followed.

3.1.3.2. Temperature

The lower and upper thresholds of MBFs for temperature are also determined from previous studies. The temperatures at which solid hydrometeors begin to melt and then completely melt depend on the relative humidity because of evaporative cooling. Matsuo and Sasyo (1981) obtained numerically a relation between the temperature and relative humidity at which snowflakes begin to melt. Since this relation does not depend on the size and type of solid hydrometeor, the temperature at which solid hydrometeors begin to melt (hereafter, T_1 [$^\circ\text{C}$]) is approximated in this study from Matsuo and Sasyo (1981):

$$T_1 = 0.07(100 - rh), \quad (11)$$

where rh is relative humidity (%). The T_1 is used as the upper threshold for MBFs of temperature for dry solid hydrometeors (DS, IC, and DG) and as the lower threshold for WS. The T_1 is also used as the lower temperature threshold for DZ, assuming that once small solid hydrometeors such as ice crystals begin to melt, they form drizzle immediately.

Matsuo et al. (1981) used statistical analysis of ground observations to show that the critical humidity above which all precipitation is rain, containing no snow particles, is a

function of surface temperature. From this relation, the temperature at which snow aggregates completely melt (hereafter, T_2 [°C]) is approximated as:

$$T_2 = 6.2 - \left(\frac{rh}{46} \right)^2, \quad (12)$$

where $rh > 23\%$. The T_2 is used as the upper threshold of the temperature MBF for WS and as the lower threshold for RN in this study. The temperature at which graupel particles completely melt may be less sensitive to relative humidity than that for snow aggregates because graupel particles are denser than snow aggregates and harder to melt. From previous studies of HC (Straka et al. 2000; Keenan 2003; Tessendorf et al. 2005), the upper threshold of MBF for WG is determined as 10°C. For the RH category, Keenan (2003), who conducted HC for tropical convective clouds producing hail, is simply followed. The lower and upper thresholds of MBFs for temperature are listed in Table 2.

To examine the impact on HC of considering relative humidity in MBFs of temperature, observational data of rain-to-snow transition case was used; for the case, the hydrometeors on the ground were transitioning from rain to snow on 23 to 24 January 2009, which was observed with the X-pol of Nagoya University located at Oshimizu in Hokuriku District (Fig. 1b).

Figure 3 shows Z_h , ρ_{hv} and the HC results for surface relative humidity of 100% and 80% in plan position indicator (PPI) at an elevation of 1.2° at 0000 Japan Standard Time (JST = UTC + 9 hours) 24 January 2009. Results without considering relative humidity, assuming $T_1 = 0^\circ\text{C}$ and $T_2 = 5^\circ\text{C}$ based on a previous study (Keenan 2003),

are also shown. Below the 0°C level (within ~15 km from the X-pol), relatively large Z_h (~30 dBZ) and low ρ_{hv} ($\lesssim 0.97$) corresponding to the melting layer are observed. At that time, rain–snow mixture (or melting snow) was observed at Kanazawa local meteorological observatory (6 m MSL), where the temperature and relative humidity were 1.8°C and 81%, respectively. Similar surface temperatures (~2°C) and relative humidities (~80%) covered a wide region over the coastal area of Hokuriku District according to the mesoscale reanalysis data from Japan Meteorological Agency (not shown). Thus, the hydrometeor type near the surface is expected to be WS.

All the HCs (Fig. 3c, 3d and 3e) identify WS near the surface corresponding to the melting layer with low ρ_{hv} (< 0.97). For HC without relative humidity (Fig. 3c), DZ is identified above the region where WS is identified and up to the 0°C level. However, DZ is not identified above the WS region for HC with a surface relative humidity of 80% (Fig. 3e). Thus, the results of HC become more realistic when relative humidity is taken into account. The results also depend on the value of relative humidity. For HC with a surface relative humidity of 100% (Fig. 3d), RN is identified up to the 0°C level, whereas with a value of 80%, RN is identified close to the surface (Fig. 3e). The latter is more realistic given that rain–snow mixture was observed at Kanazawa local meteorological observatory. Thus, considering actual relative humidity allows the HC to discriminate better between rain and solid hydrometeors near the surface in winter.

3.1.4. Inference

In the inference part of the algorithm, MBFs are aggregated and the likelihood of the existence of each hydrometeor type is evaluated. In this study, the methods for

aggregating MBFs (referred to as rule strengths) proposed by L00 is followed. They chose the products of individual MBFs as the rule strengths:

$$RS_j = \prod_i \mu_{i,j} , \quad (13)$$

where i is the measurement variable index, j is the index of hydrometeor type, RS_j is the rule strength for hydrometeor type j , and $\mu_{i,j}$ is the MBF for measurement variable i and hydrometeor type j .

3.1.5. OUTPUT

The output of our HC method is the hydrometeor type that has the largest value of rule strength, in other words, is the most likely to exist, for each radar sampling volume. To avoid unreliable results, radar sampling volumes with rule strength below 1×10^{-10} are classified as “unclassified” (UC) in this study.

3.2. Validation focus points

Of the eight hydrometeor categories in the HC method, DZ and RN are expected to be identified correctly based on D09 and D13, and the HC method is not validated for these categories. WS can be identified effectively by taking into account the effect of relative humidity on T_1 and T_2 in Eqs. (11) and (12), respectively, as described in the previous sub-section. In addition, WS is easy to identify because of the significant decrease in the values of ρ_{hv} compared with other hydrometeors when the signal-to-noise ratio (SNR) is large enough.

Identification of WG is more difficult. From the radar signal, it is difficult to distinguish between large oblate raindrops, and wet graupel particles that have melted

significantly and are therefore covered by a thick water shell (Rasmussen and Hyslop 1987). Such particles are also difficult to observe for the validation. Hail is more difficult to validate because it occurs only rarely in moist environments and is difficult to observe by X-pol because of the significant attenuation for X-band radar behind the hail shaft. However, the categories of WG and RH have been included in the HC method in preparation for a possible future improvement of the HC method although they are not validated here.

The HC method needs to be validated for the remaining three solid hydrometeor categories, namely, DG, DS, and IC. The polarimetric characteristics of DG and DS partly overlap: $Z_h \sim 30$ dBZ, near zero Z_{dr} and K_{dp} , and a high value of ρ_{hv} . DS and IC also sometimes have similar characteristics. To confirm the applicability of the HC method to these three hydrometeors, the HC method is validated with ground and in situ observations in the following section.

4. Validation of the HC method

4.1. Validation method

Validation of the HC method focuses on three solid hydrometeors: DG, DS, and IC. To validate discrimination between DG and DS, ground observations in Hokuriku District, west coast of Japan (Fig. 1b) was used. The ground observations were conducted during winter, when these solid hydrometeors are observed on the ground in Hokuriku. The HC method was validated for DS and IC by using in situ observations from a balloon-borne instrument in Okinawa, southwest Japan (Fig. 1c) during the Baiu period.

4.1.1. Graupel and snow aggregates

To explore the polarimetric characteristics of solid hydrometeors, simultaneous observations in Hokuriku were conducted from the X-pol at Oshimizu (36.82°N, 136.76°E) and a ground-based imaging system (Muramoto 1995), referred to as an “image measuring system” in Kubo et al. (2009), at Kanazawa University (36.54°N, 136.71°E), which acquires two-dimensional images of solid hydrometeors. Volume scans with the X-pol were conducted every 5 minutes from December 2008 to February 2009. Ground observations with the imaging system were conducted in January and February 2009. Comparisons between the imaging system and the X-pol were conducted for conditions under which surface temperature was $\lesssim 0^{\circ}\text{C}$ and solid hydrometeors were expected to reach the ground without melting.

The imaging system photographs naturally falling graupel and snow particles with an IEEE1394 camera (1280 \times 960 pixels, each pixel corresponding to an area of 0.1 mm

$\times 0.1$ mm) with a shutter speed of $1/10,000$ s, which gives clear images of the particles. The particles are illuminated by a lamp against a black background and each pixel is initially recorded in 256 gray-levels, and then a binary (black and white) image is produced using a threshold brightness value (Kubo et al. 2009); in this study, a brightness threshold of 50 was adopted. In the binary image white pixels are regarded as the particle and black as background.

Individual particles are classified as graupel or snow using two parameters: “roughness” and “number of holes”, as described in Kubo et al. (2009). The first parameter, the roughness, R , is given by Eq. (14):

$$R = \frac{l}{L} = \frac{l}{2\sqrt{S\pi}}, \quad (14)$$

where l is the perimeter of the particle, S is the total area of pixels inside the outline of the particle and L is the perimeter of the equivalent-area circle with area S . If the outline of the particle is a circle, $R = 1$, and R increases as the shape of the particle becomes more complex. Since the snow outline is usually more complex than graupel, the particle is classified as snow if $R \geq 1.21$, where this threshold has been determined from a visual classification of graupel and snow particles. Another parameter, the number of holes within the particle (areas of black background in the particle image), is used to determine whether the particle is snow or not; if the particle has any holes, the particle is classified as snow. Thus, particles that have no holes, with $R < 1.21$, are classified as graupel. In this study, particles with $S < 10 \text{ mm}^2$ were eliminated from the analysis because it is difficult to measure R and detect holes correctly for small particles.

Therefore, for this analysis, snow particles are assumed to be snow aggregates. While it is impossible to distinguish between dry and wet particles in the binary image, the graupel and snow particles observed with the imaging system were expected to be dry (non-melted) because the temperature at Kanazawa University during the analysis for this study was expected to be approximately $\leq 0^{\circ}\text{C}$, as mentioned above. For each particle, the equivalent volume for a spheroid was calculated.

The analysis period for comparison between HC and ground observations was from 1300 to 1500 JST 15 January 2009 and from 2100 to 2359 JST 16 February 2009, when the imaging system on the ground clearly observed graupel and snow particles. Sounding data at Wajima, ~ 60 km north-northeast of the X-pol (Fig. 1b), at 0900 and 2100 JST 15 January 2009 and 2100 JST 16 February 2009 were used to estimate the vertical profiles of temperature and relative humidity required for the HC. During these periods, a northwest monsoon prevailed and the vertical profiles of temperature and relative humidity at Kanazawa University and Wajima sounding station, both of which are located in the coastal area, were expected to be approximately the same.

For the comparison, PPI scans with the X-pol at the lowest elevation (0.6°) of the volume scan every 5 minutes are used. It is necessary to take the advection of hydrometeors between the radar beam height and the ground into account. Hydrometeors that reach the imaging system may come from an area several kilometers wide within the radar scan. The area is determined by the prevailing wind direction and speed (northwesterly in both cases and at $\sim 5 \text{ m s}^{-1}$ for 15 January and $\sim 10 \text{ m s}^{-1}$ for 16 February, estimated from soundings at Wajima) and the terminal fall velocities of

graupel and snow aggregates (assumed to be $1\text{--}5\text{ m s}^{-1}$ and $0.5\text{--}1\text{ m s}^{-1}$, respectively, approximated from Ishizaka et al. 2013). This defines the “graupel reachable area” and the “snow reachable area” to the image measuring system at Kanazawa University as shown schematically in Fig. 4. The particles in the graupel or snow reachable area at the radar beam height ($\sim 250\text{ m}$ above the imaging system) are expected to fall to the ground within several minutes, before the next volume scan begins. The numbers of all radar sampling volumes within each of these reachable areas are counted for each hydrometeor type identified by the HC for comparison with the hydrometeor type observed by the imaging system.

4.1.2. Snow aggregates and ice crystals

To validate the HC for DS and IC, simultaneous observations from the X-pol and Hydrometeor Videosondes (HYVISs, which were developed by Murakami and Matsuo 1990) in Okinawa is used. The observation was conducted during the Baiu periods in 2011 and 2012, targeting solid hydrometeors above the freezing level (Oue et al. 2015). The X-pol was installed at Aguni Island (26.58°N , 127.23°E) and HYVISs were launched from the radar site.

A HYVIS includes cameras, film to catch hydrometeors, and a radio transmitter. Hydrometeors stick to the HYVIS film and are imaged in video with two types of camera: a close-up video camera and a microscopic video camera with $7\text{--}9\text{ mm}$ and 1.4 mm angle of view, respectively. These cameras enable HYVIS to image hydrometeors from $7\text{ }\mu\text{m}$ to 2 cm in size. The images are transmitted via a radio link to the ground station. The HYVIS was launched together with a GPS radiosonde (RS-06G by Meisei

Electric Co., Ltd.), which provided sounding data for the HC.

For the comparison between the HC and HYVIS, range height indicator (RHI) scans with the X-pol were conducted in the direction of the HYVIS. For each comparison point, radar variables were averaged over all radar sampling volumes of the X-pol within a volume of $1 \text{ km} \times 1 \text{ km} \times 0.2 \text{ km}$ centered on the HYVIS position at the RHI scan time and HC was performed for this volume. The dominant hydrometeor type in the volume from the HYVIS observation was determined by visual analysis of the video. In this analysis, the largest-sized particle observed by the HYVIS in the volume was regarded as the dominant hydrometeor type. Finally, the results of the HC from the X-pol data were compared with the dominant hydrometeor type observed by the HYVIS in the volume.

4.2. Validation results

4.2.1. Graupel and snow aggregates

To examine whether the HC method effectively discriminates between DG and DS, validation results using ground observations in Hokuriku during the winter season in 2009 is shown. Figure 5 shows 1-minute accumulated numbers and the total of the equivalent volumes of graupel and snow particles observed by the ground based imaging system at Kanazawa University from 1300 to 1500 JST 15 January 2009. From 1305 to 1312 JST, graupel was the dominant type and few snow particles were observed (hereafter, Period G1). From 1315 to 1322 JST (Period S1) and from 1347 to 1355 JST (Period S2), snow was dominant and a small number of graupel particles were observed.

In Period S2, both the total number and total equivalent volume of snow particles are larger than in Period S1. From 1415 to 1418 JST (Period G2) and from 1444 to 1449 JST (Period G3), graupel was dominant although total number and total equivalent volume were smaller than in Period G1.

The HC was applied for the period corresponding to the ground observation. To interpret the results of the HC, snapshots of Z_h , Z_{dr} , K_{dp} , and ρ_{hv} superposed on the results of HC for the PPI at the lowest elevation (0.6°), and examples of ground observation images at Kanazawa University are shown in Figs. 6, 7, and 8 for Periods G1, S1, and S2, respectively.

At times corresponding to Period G1, Z_{dr} and K_{dp} are near-zero or negative in both graupel and snow reachable areas (Figs. 6b and 6c). In these regions, relatively large Z_h ($\gtrsim 25$ dBZ: Fig. 6a) and high ρ_{hv} ($\gtrsim 0.99$: Fig. 6d) are observed and DG is identified both in the graupel and snow reachable areas. This result is consistent with ground observations: large numbers of graupel particles and few snow particles (Fig. 5). Many graupel particles were conical and as large as several millimeters in size during Period G1 (Fig. 6e).

Corresponding to Period S1, Z_{dr} and K_{dp} are near zero (Figs. 7b and 7c). For the snow reachable area, relatively small Z_h (< 25 dBZ: Fig. 7a) and moderate ρ_{hv} ($\gtrsim 0.98$: Fig. 7d) are observed and DS is identified. For the graupel reachable area, some DG is identified in the region where the value of K_{dp} is slightly negative and relatively large Z_h (~ 25 dBZ) and high ρ_{hv} ($\gtrsim 0.99$) are observed. This result is consistent with the fact that snow was dominant and small numbers of graupel particles were observed on the

ground (Fig. 5). Each snow particle was several to 10 millimeters in size (Fig. 7e). Graupel particles observed on the ground were conical and smaller than 5 mm (Fig. 7f), smaller than in Period G1. However, the differences in both number and total equivalent volume between snow and graupel particles were relatively small compared with Period S2 (Fig. 5). This can be explained by the existence of some radar sampling volumes in which graupel was dominant. In fact, some DG is identified in the graupel reachable area.

Corresponding to Period S2, Z_{dr} and K_{dp} are near-zero or positive in both graupel and snow reachable areas (Figs. 8b and 8c). In these regions, the value of Z_h is relatively small ($\lesssim 25$ dBZ: Fig. 8a) and ρ_{hv} is moderate ($\gtrsim 0.98$: Fig. 8d); DS is identified here, but not DG. This result is consistent with ground observations: snow particles were the dominant type and each snow particle was as large as those in Period S1 (Fig. 8e). Small numbers of graupel particles, which were even smaller than in Period S1, were observed (Fig. 8f). Such graupel particles are considered to be too small both in size and number density to be identified as DG by the HC method.

To confirm the temporal validity of the HC, the time series of the numbers of radar sampling volumes for DG and DS in the graupel and snow reachable areas are shown in Fig. 9. Corresponding to Periods G1, G2, and G3, DG was identified in a large number of radar sampling volumes in the graupel reachable area by HC (Fig. 9a), while DS was identified in the snow reachable area corresponding to Periods S1 and S2 (Fig. 9b). These HC results agree well with the hydrometeor types observed on the ground.

Similar comparisons are made for 16 February 2009 (Figs. 10–13). During the

periods when snow was dominant on the ground (Periods S3 and S4), DS is identified in the snow reachable area (Fig. 13b). During Period S3, for example, at 2115 JST 16 February 2009, radar variables are similar to Period S2 (Fig. 8); Z_{dr} and K_{dp} are near-zero or positive, the value of Z_h is relatively small ($\lesssim 25$ dBZ) and ρ_{hv} is moderate ($\gtrsim 0.98$) in both graupel and snow reachable areas (Fig. 11). At this time, snow particles were dominant on the ground and small numbers of graupel particles, all smaller than 5 mm, were observed (Fig. 11f). On the other hand, DG is identified in the graupel reachable area (Fig. 13a) during the periods when graupel was dominant (Period G4: Fig. 12). At 2245 JST 16 February 2009, during Period G4, radar variables are similar to Period G1 (Fig. 6); Z_{dr} and K_{dp} are near-zero or negative, the value of Z_h is relatively large ($\gtrsim 25$ dBZ) and ρ_{hv} is high ($\gtrsim 0.99$) in the reflectivity core in the graupel reachable area (Fig. 12). At this time, graupel particles were dominant on the ground (Fig. 12e) and few snow particles were observed.

4.2.2. Snow aggregates and ice crystals

To examine whether the HC method effectively discriminates between DS and IC, the results of the validation with HYVISs in Okinawa in 2011 and 2012 are shown. Out of a total of 17 HYVIS flights, three HYVISs launched into stratiform precipitating clouds with radar echo-top height well above the freezing level were used for validation of the HC method for DS and IC: HYVIS #1 launched at 1540 JST 1 June 2011, HYVIS #2 at 0746 JST 31 May 2012, and HYVIS #3 at 2315 JST 9 June 2012. For HYVIS #3, RHI scans were conducted every two minutes, corresponding to a height interval of ~500 m of the ascending HYVIS, and a quantity of good data for comparison

between HC and the HYVIS was obtained.

Figure 14 shows the Z_h in PPI, Z_h and the result of HC in RHI, the result of HC at the HYVIS position and an example of an image obtained by HYVIS at 2338 JST 9 June 2012 (HYVIS #3). The 0°C level inferred from sounding was at ~ 4.7 km (MSL) and a bright band was evident near the melting level (Figs. 14b and 14c). The HC results of RHI (Fig. 14d) identify WS near the melting level, RN or DZ below the melting level, and DS and IC above the melting level. IC is identified by HC (Fig. 14e) using averaged radar variables in a $1 \text{ km} \times 1 \text{ km} \times 0.2 \text{ km}$ volume (as described in Section 4.1) centered on the HYVIS. A few snow aggregates composed of column particles were observed in the HYVIS images (Fig. 14f).

Figure 15 shows the results of validation of the HC for the HYVIS #3 flight. For each comparison point between the HC and the HYVIS, HC was conducted as in Fig. 14. For the IC category, the HC results agree well with the hydrometeor types observed with the HYVIS well above the freezing level, and the polarimetric characteristics are reasonable for IC: small Z_h (< 20 dBZ), positive Z_{dr} , and high ρ_{hv} (> 0.97). At a height of ~ 6.5 km, a few snow aggregates were observed as mentioned above (Fig. 14f). Because the number concentration of snow aggregates at this height was very low, the HC result (IC: Fig. 14e) is reasonable.

DS and IC are also identified correctly for HYVIS #1 (Fig. 16) and #2 (Fig. 17), respectively. For the case of HYVIS #1 (Fig. 16), the value of Z_h around the HYVIS is larger than that of HYVIS #2 (Fig. 17). Thus, the HC results for these cases (DS for HYVIS #1 and IC for HYVIS #2) are reasonable. Unfortunately, since the RHI time

interval was coarse, data for comparison between the HYVIS and the X-pol were available only at one point for each of these HYVIS flights.

Well below the freezing level for the HYVIS #3 flight, rain was correctly identified. Around a height of 3 km, WG was identified by HC although raindrops were observed with the HYVIS (Fig. 15). This can be attributed to the local minimum of ρ_{hv} (< 0.97). Around the melting level, it is difficult to compare HC and HYVIS observations because solid hydrometeors attached to HYVIS may melt quickly. Although the HC method tends to over-identify WG, it effectively classifies rain and solid hydrometeors (DS and IC) within the cases considered for validation.

5. Application the HC method to summer thunderclouds

The HC method for X-pol has been developed through reconstruction of HC method based on previous studies, and validated by ground and in situ observations described in previous sections. In this section, the application of the HC method is considered. The HC method for X-pol can effectively identify solid hydrometeors: snow aggregates, ice crystals, and graupel. This is notably useful for understanding severe weathers, such as lightning, hail falling, downburst, and so on. Among them, lightning is produced by solid hydrometeors in thundercloud, which can be identified by the HC method developed in this study. Especially, previous laboratory and observational studies have revealed that the cloud-to-ground lightning polarity is relating to existence of solid hydrometeors in thundercloud. Thus, thundercloud is appropriate target for demonstration of the performance of the HC method. Because of simple structure, isolated summer thundercloud is application target of the HC method in this study.

5.1. Background of thundercloud

Summer thunderclouds produce cloud-to-ground (CG) lightning within a few ten minutes after appearing on radar echoes (Workman and Reynolds 1949; Reynolds and Brook, 1956). During this time, thunderclouds undergo electrification (Stolzenburg and Marshall 1998) with distinct positively- and negatively-charged regions. When the electric intensity between these charges exceeds the limit of insulation, electrical breakdown occurs as lightning to neutralize separated charges. CG lightning occurs in

order to neutralize charges in thunderclouds with the induced charge on the Earth's surface. Thus, CG lightning polarities should reflect charge distributions resulting from hydrometeor distributions in thunderclouds, which can change quickly as a result of dynamic motion.

CG lightning polarities have been examined in many previous studies. These studies have shown that the contribution of positive strikes to the total amount of CG lightning in summer thunderstorms is only a few percent (e.g., Rust et al. 1981a, b; Fuquay 1982). On the other hand, Stolzenburg (1994) reported high rates and high densities of positive CG lightning strikes in hail-producing thunderstorms at and near the beginning of active periods of CG lightning. This study also indicates that positive CG strikes may be associated with rapid increases in the top height of radar echoes.

Weather radar has been used to examine the relationship between lightning activity and the vertical extent of thunderclouds. Larsen and Stansbury (1974) showed a positive correlation between areas with strong reflectivity cores (radar reflectivity $Z > 43$ dBZ) at the -30°C level and the sferics rate for summer thunderstorms. Comparisons between time variations in radar echo height and lightning activity showed that lightning occurs after a period when the top of a strong reflectivity core (e.g., $Z \gtrsim 30$ dBZ) exceeds the -10 to -20°C level (Williams et al. 1989; Michimoto 1991).

Previous laboratory experiments show that graupel particles above the freezing level develop a charge through a “noninductive charging mechanism” caused by collisions between ice crystals and coexisting supercooled liquid water (SLW) droplets (Takahashi 1978; Saunders et al. 1991; Brooks et al. 1997; Saunders and Peck 1998). According to

these studies, graupel charge polarity has been shown to depend on ambient temperature and cloud water content. Further, studies of noninductive charging mechanisms have also shown that graupel particles have a negative charge below the “charge-reversal temperature” (−10 to −20°C) and a positive charge in warmer air (e.g., Houze 1993).

Brooks et al. (1997) and Saunders and Peck (1998) showed that the charge polarity of the graupel particles is a function of temperature and rime accretion rate (RAR) as follows:

$$\text{RAR} = \text{EW} \times V \quad (15)$$

where EW is the effective liquid water content and V is the crystal–graupel relative fall velocity (Saunders and Peck 1998). According to these experiments, graupel particles have a positive charge when the rime accretion rate is greater than a critical value that is a function of temperature. Positively charged graupel (with a high rime accretion rate) occurs under two conditions: 1) in an SLW-rich environment; i.e., high values of EW in Eq. (15), and 2) in the case of large graupel particles with large falling velocities, resulting in high values of V in Eq. (15). These conditions occur with strong updrafts and/or plenty of moisture in well-developed thunderclouds. According to the noninductive charging mechanism, the charge polarity of graupel particles depends on temperature and cloud water content (or rime accretion rate) in regions where graupel particles and ice crystals collide and acquire opposite charges. Thus, an examination of the relationships between the space–time distribution of solid hydrometeors in thunderclouds and lightning polarity is appropriate theme for the examination of the performance of the HC method and will improve our understanding of lightning

neutralization in the context of the noninductive charging mechanism.

To understand lightning mechanisms in thunderclouds using the principles of the noninductive charging mechanism, it is necessary to obtain information about hydrometeor types and their distribution in thunderclouds. Over the last few decades, polarimetric radar has enabled the identification of hydrometeor types and the investigation of their space–time distribution in thunderclouds using polarimetric radar variables (e.g., radar reflectivity Z_h , differential reflectivity Z_{dr} , specific differential phase K_{dp} , and correlation coefficient ρ_{hv}). Carey and Rutledge (1996) estimated the graupel echo volume in a multi-cell thunderstorm using an HC method (Doviak and Zrnić 1993). They suggested that maxima in hail rates are related to peaks in the CG lightning flash rate. They also suggested a strong correlation between the radar-inferred graupel echo volume and the in-cloud lightning flash rate. Carey and Rutledge (2000) estimated the graupel ice mass during tropical convection using the reflectivity Z_h and difference reflectivity Z_{dp} , showing a positive correlation between the CG lightning flash rate and polarimetric radar-inferred graupel ice mass.

Recent studies have compared polarimetric radar-inferred graupel or hail volumes with CG lightning polarity for positive CG-producing thunderclouds. Tessendorf et al. (2005) and Wiens et al. (2005) used HC methods to examine polarimetric radar-inferred graupel and hail echo volumes for a positive CG-dominant supercell storm. Large volumes of graupel and hail echoes were inferred from polarimetric radar when large numbers of positive CG lightning sources were detected using VHF radiation. From these results, Wiens et al. (2005) showed that the dominance of positive CG lightning in

a precipitation core might be caused by non-inductive charging mechanisms resulting in positively charged graupel particles in an SLW-rich environment. Previous studies have used polarimetric Doppler radar analysis to show that the occurrence of positive CG lightning in SLW-rich environments may occur in severe, hail-producing storms with strong updrafts (e.g., Lang and Rutledge, 2002).

Studies described above show that the relationship between CG lightning strike polarity and the volume of solid hydrometeors can be explained by the noninductive charging mechanism. However, this relationship has been examined mainly by using total graupel/hail volumes or radar-inferred ice mass (including both reflectivity cores and anvil areas) in severe thunderstorms with a long duration and steady state conditions. Few studies have examined the temporal variability of reflectivity cores in thunderclouds, which can exhibit rapid structural changes over a thundercloud life cycle. Reflectivity cores produce CG lightning strikes and their structure affects lightning activity in thunderclouds via the non-inductive charging mechanism of solid hydrometeors. Therefore, precise analysis that incorporates high spatial and temporal resolutions will be needed in order to improve our understanding of the relationship between lightning activity and thundercloud structures. Isolated summer thunderclouds are appropriate targets for this type of analysis because their structures are simple and so are suitable for examining the temporal variability of thunderclouds. The examination of the space–time distribution of solid hydrometeors in such thunderclouds would help our understanding of the charge distributions associated with solid hydrometeors in thunderclouds and demonstrate the performance of the HC method.

In this section, the relationship between CG lightning polarity and the space–time distribution of solid hydrometeors is examined to demonstrate the performance of the HC method and to improve the understanding of the charge distribution through lightning activity in thunderclouds using principles of the noninductive charging mechanism. The data used in the study were obtained from the X-band polarimetric radar (X-pol) of Nagoya University and Lightning Location System (LLS) of Chubu Electric Power Co., Inc., which covers the X-pol observational area in central Japan. Two isolated summer thunderclouds with different CG lightning polarities were selected from the dataset. The storm on 26 July 2010 produced almost solely negative CG strikes, and the other on 25 August 2010 produced some positive CG strikes in the reflectivity cores. For each storm, we examined the space–time distribution of solid hydrometeors using an HC method for X-pol. Section 5.2 outlines our data and methodology of the application of the HC method to the summer thunderclouds. Section 5.3 provides an overview of each case study to examine the relationships between CG lightning polarity and the space–time distribution of solid hydrometeors and confirm the performance of the HC method. Then, a precise examination of the relationship between the CG lightning polarity and the solid hydrometeor distribution in reflectivity cores of the thunderclouds, which is a great interest of this application, is given in Section 5.4.

5.2. Observation of summer thunderclouds

5.2.1. Instruments

The dataset from the Nagoya University X-pol was used to detect thunderclouds,

and the LLS operated by the Chubu Electric Power Co., Inc. was used to obtain the locations and polarity of the CG lightning. The specifications and observation range of the Nagoya University X-pol for the application observation are shown in Table 1 and Fig. 1d, respectively. During the analysis periods in summer 2010, the X-pol was operated every 6 minutes with a volume scan of plan position indicators (PPIs) at 15 elevations (from 0.5° to 33.5°). Data obtained from the X-pol was processed to eliminate non-meteorological echoes and make noise/attenuation corrections as described in Section 2.1. Processed polarimetric radar variables, for this application section, were then interpolated into constant altitude PPI (CAPPI) data onto a $0.5 \times 0.5 \times 0.5$ km Cartesian coordinate grid, following the interpolation method by Cressman (1959).

LLS data were used to obtain the location and polarity of the CG lightning (Momozawa et al. 2012). The accuracy of lightning locations in the X-pol observation area is about 0.5 km, which is comparable with the grid spacing of CAPPI from the X-pol. This resolution is sufficiently accurate to examine the relationships between solid hydrometeor distribution and lightning polarity.

5.2.2. Analytical methods

The numbers of positive and negative CG lightning strikes measured by LLS in each 6-minute period (the time step of the X-pol volume scan) were counted, and compared to the HC from the X-pol every 6 minutes. The HC method was applied to the X-pol data to examine the solid hydrometeor distribution in the thunderclouds. The HC method has been validated for graupel, snow aggregates, and ice crystals using ground

and *in situ* observations for these solid hydrometeors as described in Section 4, and is suitable for use in targeting thunderclouds that produce little or no hail.

The HC was conducted for each $0.5 \times 0.5 \times 0.5$ km CAPPI volume in each thundercloud using interpolated polarimetric radar variables and temperatures estimated from sounding data recorded at the site closest to the analysis area (Hamamatsu; Fig. 1d). The HC method identifies the most likely hydrometeor type for each CAPPI volume from eight hydrometeor categories, as described in Section 3.1: drizzle (DZ), rain (RN), wet snow aggregates (WS), dry snow aggregates (DS), non-aggregated ice crystals (IC), dry graupel (DG), wet graupel (WG), and rain–hail mixture (RH). DG is assumed to be low-density graupel particles with low temperatures and relatively low SLW contents. WG is assumed to be high-density and/or wet graupel produced via wet growth in an SLW-rich environment, resulting in larger Z_h values than for DG. As it is difficult to distinguish between WG and small hail using polarimetric radar observations, the WG category may include some small hail. Although DG and WG were not necessarily distinguished strictly according to the HC, the presence of WG indicates higher rime accretion rates than for DG volumes alone.

After identification of each hydrometeor type, CAPPI volumes ($0.5 \times 0.5 \times 0.5$ km) identified as DS, IC, DG, and WG were counted in each 6-minute volume scan. The temporal variation of each hydrometeor volume (the total volume and vertical distribution) was compared with the location and polarity of CG lightning obtained from the LLS.

To focus on graupel particles that undergo riming electrification via the

noninductive charging mechanism, HC and LLS were also compared in the thundercloud reflectivity cores. In this analysis, a reflectivity core is defined as a 5×5 km horizontal area centered on a reflectivity local maximum of greater than 40 dBZ. This reflectivity maximum must continue for at least two volume scan time steps at 7 km above sea level. Summer temperature in Japan at this elevation is about -10°C to -15°C (corresponding to the charge reversal temperature). Figure 18 is a schematic illustration of the method used to detect and track the reflectivity core. In the figure, time passes from 18a to 18c corresponding to the life cycle of the reflectivity core. First, the reflectivity local maximum > 40 dBZ was detected at 7 km (Fig. 18b), and the reflectivity core was delineated above the 0°C level (5×5 km) with vertical continuity assessed by visual analysis. Then, the reflectivity core was tracked forward (Fig. 18c) and backward (Fig. 18a) in time, and tracking was terminated when the reflectivity maximum above the 0°C level fell below 30 dBZ.

5.3. Overview of the summer thunderclouds

Two summer thunderclouds in central Japan were selected to examine the relationship between solid hydrometeor distribution and lightning polarity. One of the thunderstorms (26 July 2010; Case A) produced almost solely negative CG strikes, but the other (25 August 2010; Case B) produced some positive CG strikes in reflectivity cores. In both cases, the 0°C level was 4.9 km, which is typical for summer in Japan. The -10°C level, which corresponds to the charge reversal temperature, was 6.4 km in Case A and 6.9 km in Case B. The maximum 15-dBZ echo top heights were 12.0 km for

Case A and 16.5 km for Case B. The thunderclouds in cases A and B (Thunderclouds A and B) were composed of four and six reflectivity cores, respectively (Table 4).

5.3.1. Case A: 26 July 2010

Figure 19 shows a time series of radar reflectivity for Case A at 7 km (just above the -10°C level) from 2048 Japan Standard Time (JST = UTC + 9 hours) to 2136 JST. Thundercloud A was generated at 2030 JST with a radar echo greater than 15 dBZ below 7 km (not shown). It appeared at 7 km at 2048 JST (Fig. 19a), and then produced mainly negative CG strikes from 2054 to 2124 JST (Figs. 19b–e). Between 2100 and 2112 JST, a large number of negative CG strikes were produced in reflectivity cores (Figs. 19b–d). At 2112 JST (Fig. 19d), just one positive CG strike occurred in a reflectivity core. From this time, a weak reflectivity area spread gradually that corresponded to the shape and location of the anvil. At 2124 JST, Thundercloud A produced the last CG strike (Fig. 19e) and then dissipated (Fig. 19f).

To provide an overview of the relationship between solid hydrometeor volumes (DS, IC, DG, and WG) and lightning polarity in Thundercloud A, Figure 20 shows a time series of 6-minute accumulated CG strike numbers and the volume of solid hydrometeors estimated using the HC. Note that the number of CG strikes includes those in both the reflectivity cores and the anvil (black rectangle in Fig. 19). During a period with a negative CG strike from 2054 to 2124 JST, large volumes of graupel (DG and WG) were identified by the HC. After this period, the volume of graupel diminished rapidly. Volumes of DS and IC increased constantly between the generation of Thundercloud A at 2030 JST and around 2118 JST, and large volumes of DS and IC

remained in the late stages of Thundercloud A, corresponding to the spread of the anvil area.

To examine the vertical distribution of solid hydrometeors, Figure 21 shows solid hydrometeor volumes at height intervals of 0.5 km above the 0°C level. Just before the start of the negative CG strikes, a small volume of DG was identified above the -10°C level (Fig. 21a). The DG volume increased when the first (negative) CG strikes occurred (Fig. 21b), and a large volume of DG was identified above the -10°C level (Figs. 21c and d) during the period with a large number of negative CG strikes. At 2112 JST, large volumes of both WG and DG were identified at heights up to 9.5 km and 12.0 km (about -30°C and -45°C), respectively (Fig. 21d). This suggests that high rime accretion rates may have led to the formation of positively charged graupel. This is supported by the occurrence of a positive CG strike in reflectivity core A2 at that time (Table 5). At 2124 JST, the DG volume peak height declined and the last CG strike was observed (Fig. 21e). The DG volume then disappeared, and the DS and IC volumes remained above the 0°C level (Fig. 21f).

5.3.2. Case B: 25 August 2010

Figure 22 shows the time series of radar reflectivity at 7 km (around the -10°C level) from 1554 to 1654 JST for Case B. Thundercloud B was generated at 1530 JST with a radar echo greater than 15 dBZ below 7 km, and appeared at 7 km at 1548 JST (not shown). Reflectivity core A1 appeared at 1554 JST (Fig. 22a), and then produced negative CG strikes from 1600 JST (Fig. 22b). After this time, Thundercloud B developed successive reflectivity cores in its upwind (southwest) sector. Negative CG

strikes were observed in the reflectivity cores, and positive CG strikes were observed in weak reflectivity areas corresponding to the anvil (Figs. 22c–f). In addition, positive CG strikes were observed in reflectivity cores from 1612 JST. After that time, thundercloud activity decreased (Fig. 22f), but positive CG strikes continued within a few reflectivity cores (Tables 6 and 7).

Figure 23 shows a time series of 6-minute accumulated number of CG strikes and the volume of solid hydrometeors for Thundercloud B estimated by the HC. There are two peaks in CG strike numbers at 1612 and 1636 JST, which corresponds to peaks in lightning activity in reflectivity cores B2 and B4, respectively. Both DG and WG volumes were identified during the period of negative CG strikes. Large volumes of DG and WG were identified during the period of positive CG strikes after 1612 JST. As for Thundercloud A, the volumes of DS and IC also increased in the latter stage of Thundercloud B, corresponding to the spread of the anvil area.

Figure 24 shows the vertical distribution of solid hydrometeors in Thundercloud B. Before the start of CG strikes, almost no DG and WG volumes were identified above the -10°C level (Fig. 24a). At 1600 JST, the first negative CG strike occurred, and DG and WG volumes were identified above the -10°C level (Fig. 24b). From 1612 JST, positive CG strikes were observed (Fig. 23a) and large volumes of DG and WG were also identified well above the -10°C level (Figs. 24c–f), implying high rime accretion rates. In contrast to Case A (Figs. 20 and 21), a large volume of solid hydrometeors remained above the -10°C level, and CG strikes continued for a relatively long time (Figs. 23 and 24) as a result of the successive generation of reflectivity cores (B5 and

B6; Tables 4, 6, and 7).

5.4. Reflectivity cores

In both cases A and B, negative CG strikes were observed in all reflectivity cores where there were most probably graupel particles. For Case A, only one of the four reflectivity cores (A2) produced a positive CG strike (Table 4). For Case B, all reflectivity cores (B1–B6) produced one or more positive CG strikes. Compared with reflectivity cores without positive CG strikes (hereafter, NRCs), reflectivity cores with positive CG strikes (PRCs) developed more deeply in 30 and 40 dBZ echo top heights. These reflectivity cores also had greater DG and WG volume maximum heights (Table 4). According to the analysis of Case A, the necessary conditions for PRCs are heights equal to, or over, 11.5 km (ambient temperature of about -45°C) for the 30 dBZ echo top height, 8.5 km (about -25°C) for the 40 dBZ echo top height, 12.0 km (about -45°C) for the maximum DG volume height, and 9.5 km (about -30°C) for the maximum WG volume height. All reflectivity cores in Case B were PRCs and satisfied these conditions.

Data from reflectivity core A1 were further analyzed to investigate the characteristics of NRCs. This NRC had the longest duration and the highest echo tops (30 and 40 dBZ), as well as maximum DG and WG volume heights. Among the PRCs, reflectivity cores B2 and B4 had the first and second highest 30 and 40 dBZ echo top heights and the highest maximum DG and WG volume heights. Although echo top and maximum graupel volume heights of B4 were lower than those of B2, B4 had more

positive CG strikes (Table 4). Reflectivity core B2 had only two positive CG strikes, which is a typical PRC number in this study, whereas B4 had ten positive CG strikes. To examine the factors that control the number of positive CG strikes, we also analyzed the characteristics of reflectivity cores B2 and B4.

5.4.1. Reflectivity core A1

To provide an overview of the temporal variation of reflectivity core A1, a time series of Z_h at 7 km from 2042 to 2112 JST on 26 July 2010 is shown in Fig. 25. Reflectivity core A1 was initially detected at 2042 JST, but the radar echo had not reached 7 km at that time (Fig. 25a). At 2048 JST, a radar echo greater than 40 dBZ appeared at 7 km (Fig. 25b), and the first negative CG strike occurred in the reflectivity core at 2054 JST (Fig. 25c). After that time, reflectivity core A1 did not intensify significantly (Figs. 25d and e), and only negative CG strikes were observed in the reflectivity core before it dissipated (Fig. 25f).

Figure 26 shows the time series of echo top heights (15, 30, and 40 dBZ), maximum heights of graupel volumes (DG and WG), and the numbers of positive and negative CG strikes from 2042 to 2112 JST on 26 July 2010 for reflectivity core A1. Echo top and maximum graupel volume heights increased continuously from the generation of reflectivity core A1 at 2042 JST until 2054 JST when CG activity began. At 2100 JST, echo top and maximum graupel volume heights reached their peaks, as did CG activity. After that time, echo top and maximum graupel volume heights declined gradually, and the number of negative CG strikes decreased. Echo top heights of 30 and 40 dBZ did not exceed 12 km (ambient temperature of about -45°C) and 9 km (-25°C to -30°C),

respectively, throughout the lifespan of reflectivity core A1.

To examine the space–time distributions of solid hydrometeors (DS, IC, DG, and WG) in reflectivity core A1, Figure 27 shows a time series of the vertical cross section and vertical distributions of solid hydrometeor volumes in reflectivity core A1. At 2042 JST, solid hydrometeor volumes did not reach the -10°C level (Figs. 27a and g). At 2048 JST, just before the initiation of negative CG strikes, small volumes of graupel (DG and WG) were identified above the -10°C level (Figs. 27b and h). At 2054 JST, when negative CG strikes began, considerable volumes of DG and WG were identified above the -10°C level (Figs. 27c and i). At 2100 JST, when CG activity reached its peak, large volumes of DG and WG were identified above and around the -10°C level, respectively (Figs. 27d and j). After this time, the WG volume diminished above the -10°C level (Figs. 27e and k) and the height of the maximum DG volume declined gradually (Figs. 27f and l). The volumes of the solid hydrometeors identified out of the reflectivity core (red dashed boxes in Figs. 27a–f) remained small throughout the lifespan of reflectivity core A1.

5.4.2. Reflectivity core B2

The time series of Z_h in reflectivity core B2 at 7 km is shown in Fig. 28 from 1600 to 1624 JST on 25 August 2010. Reflectivity core B2 was initially detected at 1600 JST, but the radar echo had not reached 7 km at that time (Fig. 28a). At 1606 JST, a radar echo greater than 40 dBZ appeared at 7 km and the first negative CG strike was observed (Fig. 28b). At 1612 JST, CG activity in reflectivity core B2 reached its peak and a large number of negative CG strikes occurred (Fig. 28c). After that time,

reflectivity core B2 weakened (Fig. 28d) and reflectivity became indistinct (Fig. 28e).

Figure 29 shows the time series of echo top heights (15, 30, and 40 dBZ), maximum heights of graupel volumes (DG and WG), and the numbers of positive and negative CG strikes from 1600 to 1624 JST on 25 August 2010 for reflectivity core B2. After the generation of reflectivity core B2 at 1600 JST, it developed rapidly and the 30-dBZ echo top height reached 16.5 km at 1612 JST. A large number of negative CG strikes occurred at that time along with some positive CG strikes. Positive CG strikes also occurred during the next time step at 1618 JST. After this time, echo top heights diminished rapidly, and the number of negative CG strikes decreased at 1618 JST. At 1624 JST, the upper part of reflectivity core B2 become indistinct in the CAPPI radar reflectivity (Fig. 28e). To avoid possible contamination from another reflectivity core, B2 data over 6.5 km in height was excluded from the analysis. It is possible that the residue hydrometeors of reflectivity core B2 became part of reflectivity core B4, as discussed in the following subsection.

Figure 30 shows a time series of the vertical cross section and vertical distribution of solid hydrometeor volumes of reflectivity core B2. At 1600 JST, before the onset of lightning activity, there were no graupel volumes (DG and WG) identified above the -10°C level (Figs. 30a and f). At 1606 JST, negative CG strikes began, and DG and WG volumes were identified above the -10°C level (Figs. 30b and g). At 1612 JST, when echo top height and lightning activity peaks occurred, a large volume of WG was identified above the -10°C level and the DG volume reached over 15 km in height (Figs. 30c and h). The maximum WG volume height declined after this time (Figs. 30d and i).

As shown in the vertical cross section of reflectivity core B2 (Figs. 30a–e), hydrometeors at the edge of the radar echo were unclassified (UC). This indicates unreliable HC results caused by an extremely low rule-strength in the fuzzy HC (see HC studies for details of the fuzzy HC method; e.g., L00). In this case, the UC result relates to low values of ρ_{hv} (not shown), which can be attributed to Mie scattering in severe convective regions that possibly contain hail. The UC volume can affect the magnitude of the graupel volumes (DG and WG) at each height, but the tendency of graupel volumes (developing to high altitudes and diminishing rapidly) does not change. Thus, the UC volume was excluded from this analysis.

5.4.3. Reflectivity core B4

Figure 31 shows the time series of Z_h at 7 km from 1624 to 1654 JST on 25 August 2010 for reflectivity core B4. At 1624 JST, reflectivity core B4 was initially detected in a preexisting high reflectivity area (Fig. 31a). Negative CG strikes began at 1630 JST (Fig. 31b). A large number of negative CG strikes occurred at 1636 JST (Fig. 31c) and 1642 JST (Fig. 31d), and were accompanied by positive CG strikes. After that time, reflectivity core B4 gradually weakened and few additional CG strikes were observed (Figs. 31e and f).

Figure 32 shows a time series of echo top heights (15, 30, and 40 dBZ), maximum graupel volume heights (DG and WG), and the numbers of positive and negative CG strikes from 1624 to 1700 JST for reflectivity core B4. Reflectivity core B4 was initially identified at 1624 JST. At that time, the 30-dBZ echo top height was already as high as 12.0 km. As described in the previous subsection, reflectivity core B4 may have

contained residual hydrometeors from reflectivity core B2. At 1630 JST, the 15, 30, and 40 dBZ echo top heights, and maximum WG volume height increased. Peak lightning activity and echo top heights occurred in reflectivity core B4 at 1636 JST. Echo top heights and positive CG activity continued until 1642 JST, and then diminished.

Figure 33 shows the time series of the vertical cross section and vertical distribution of solid hydrometeor volumes of reflectivity core B4. At 1624 JST, when B4 was first detected, graupel (DG and WG) volumes were already identified above the -10°C level (Figs. 33a and g). The WG volume above the -10°C level increased at 1630 JST (Figs. 33b and h). Peak CG activity occurred at 1636 JST, and a large volume of DG was identified above the -10°C level (Figs. 33c and i). The DG volume above the -10°C level was persistent after this time, and positive CG strikes were observed until 1642 JST (Figs. 33d and j). At 1648 JST, a large volume of DG was identified up to 12.5 km, but the WG volume above the -10°C level diminished (Figs. 33e and k). After that time, reflectivity core B4 diminished and the DG volume height decreased at 1654 JST (Figs. 33f and l). Large volumes of solid hydrometeors were identified both in and out of the reflectivity core (red dashed boxes in Figs. 33a–f) throughout its lifespan.

6. Discussion

6.1. Validity of the HC method

The HC method developed in this study identifies hydrometeor type from eight categories including rain, wet snow, dry snow aggregates, non-aggregated ice crystals, graupel, and rain–hail mixture. These hydrometeor categories cover almost all hydrometeor types that previous HC studies identify with longer wavelengths (S- and C-bands) (e.g., Doviak and Znić 1993). This is useful properties for observing precipitation clouds that contain solid hydrometeor in various situations: summer thunderclouds, winter snow clouds, and so on. The HC method is developed targeting precipitation clouds under moist environments, such that occurs in East Asia, with little or no hail.

As described in Section 3.1, the HC method effectively identified rain, wet snow and dry snow aggregates in a rain-to-snow transition case by accounting for temperature and relative humidity on the ground, as seen in Fig. 3. This is important capability to prevent the weather disasters brought by melting snow. Because the HC method developed in this study takes account of the temperature that solid hydrometeors melt depends on relative humidity because of evaporation cooling, the HC method is expected to be valid for wet snow detection, especially near the surface (in the sub-cloud layer) in winter season.

For hail, it is difficult to observe with X-pol because of attenuation and Mie scattering from hail shaft in the wavelength of X-band, and thus identify precisely. The attenuation problem from the hail shaft could be partially solved by observation using

X-pol network from different side of the hail shaft.

The HC method is designed to identify the most probable, one hydrometeor type for each radar sampling volume, and it works effectively as shown in the appreciation in Section 5. The HC method identifying one hydrometeor type seems to have been completed by previous intense studies in the history of HC. The identification of multi-hydrometeor-type situation by polarimetric radar would be the next breakthrough technology in the future.

6.2. Validity of the validation of the HC method

The HC method developed in this study has been validated by ground and in situ observations of solid hydrometeors (DS, IC, and DG) in Section 4. These solid hydrometeors are needed to be validated as discussed in Section 3.2, and are sufficient constituent of the validation of HC for X-pol under present technology. The validation for DG and DS used Hokuriku ground observation. In general, graupel particles exist in limited environment (in the convective area) and are difficult to observe by in situ instrument. In this study, however, appropriate data of graupel particles for the validation were obtained from ground observations in Hokuriku, where graupel particles as well as snow aggregates are frequently observed on the ground in winter season, and validation showed appropriate performance of the HC for discriminating between DG and DS. The validation for DS and IC, precious in situ observational data of precipitating clouds with considerably thick in the vertical direction were obtained by HYVIs. Although the sampling number was not so many, the in situ data helped

effective validation of the HC method for DS and IC.

Out of the three hydrometeor categories, wet (melting) hydrometeors (WS and WG) are difficult to validate because the degrees of their melting varies case by case and they are hard to detect by in situ observation. This problem would be solved future improvement of performance of in situ observational instruments. From the X-pol side, HC accounting for spatial variability and history of hydrometeor category surrounding a certain radar sampling volume (e.g., DG change into WG, and then RN) would improve the HC performance and help the comparison between radar and in situ observations for the validation.

6.3. Performance of the HC method

The HC method was applied to isolated summer thunderclouds in Section 5. In general, summer thunderclouds contain solid hydrometeors for which the HC method was validated in Section 4, and they provide cloud-to-ground lightning discharge via riming electrification mechanism (e.g., Takahashi, 1978) by collision of these solid hydrometeors. Thus, the thunderclouds are appropriate target for examining the performance of the HC method.

In both cases A and B described in Section 5, a large volume of DG above the -10°C level corresponded to negative CG strikes in the cores of thunderclouds (Figures 20, 21, 23 and 24). On the other hand, both before and after CG activity, only small volumes of graupel (DG and WG) were identified. In the latter stage of CG activities, large volumes of DS and IC were identified when positive CG strikes were observed in the anvil area

(Figures 22d–f, 23, and 24d–f). These results are consistent with previous studies of the polarities of CG strikes in typical summer thunderstorms (e.g., Rust et al., 1981a, b; Marshall et al., 1989). In the reflectivity cores of the thunderstorms, graupel particles above the -10°C level generally obtain a negative charge through the noninductive charging mechanism (e.g., Takahashi, 1978) when the SLW content is relatively low, resulting in negative CG strikes in reflectivity cores. Then, after collision with graupel particles and charging positively in reflectivity cores, ice crystals would be blown into anvil areas and produce positive CG strikes. The results of HC are consistent with these processes of solid hydrometeors in thundercloud, and they indicate the appropriate performance of the HC method when applied to summer thunderclouds. Because of its performance, the HC can be used for the further examination of the relationship between lightning polarity and solid hydrometeor distribution in reflectivity cores of thundercloud, which change their structure rapidly and need precise observations with high spatial and temporal resolution.

Thunderclouds A and B were composed of several reflectivity cores (Table 4). These reflectivity cores were classified into three categories, summarized in the schematic diagram in Fig. 34. The first category (Fig. 34a) represents reflectivity cores that produced no positive CG lightning strikes (NRCs; reflectivity cores A1, A3, and A4). These cores had relatively low maximum graupel volume heights (less than the -45°C level). The second category (Fig. 34b) contains reflectivity cores that produced positive CG strike(s) (PRCs; reflectivity cores B1–B3, B5, and B6). These cores had higher maximum graupel volume heights than NRCs (up to about the -70°C level). The third,

category (Fig. 34c) contains reflectivity cores that produced several positive CG strikes (reflectivity core B4). This core had high maximum graupel volume heights with a relatively long duration.

All reflectivity cores in thunderclouds A and B produced negative CG strikes at some point in their life cycles. This is consistent with the noninductive charging mechanism, whereby the graupel volumes in reflectivity cores only have to exceed the -10°C level by a few kilometers to produce negative CG strikes. Indeed, the maximum DG volume height in reflectivity core A4 was only 9.5 km (ambient temperature was about -30°C).

As shown in Table 4, a major finding in the application of the HC method is that the PRCs (Figs. 34b and c) had greater echo top heights (30 and 40 dBZ) and maximum graupel volume heights (DG and WG) than the NRCs (Fig. 34a). The necessary conditions for PRCs in this study were heights equal to or over 11.5 km (ambient temperatures of about -45°C) for the 30 dBZ echo top height, 8.5 km (about -25°C) for the 40 dBZ echo top height, 12.0 km (about -45°C) for the maximum DG height, and 9.5 km (about -30°C) for the maximum WG height. It is considered that these conditions are valid in the case studies analyzed, although they are insufficient to determine a universal threshold. These results indicate that PRCs contain larger graupel particles with greater reflectivity values up to higher altitudes than NRCs, implying high rime accretion rates and graupel with positive charge polarity (Saunders and Peck, 1998) (dashed ellipses in Figs. 34b and c).

Among the PRCs, reflectivity core B2 (short-lasting) and B4 (long-lasting) had the

first and second highest echo tops and maximum graupel volume heights, respectively (Table 4). The former had only 2 positive CG strikes, whereas the latter had 10 positive CG strikes. Echo top heights increased and decreased rapidly during the life cycle of reflectivity core B2 (Fig. 29). The volumes of graupel (DG and WG) above 10 km (ambient temperature below -30°C) were relatively small, although the maximum heights exceeded 15 km (ambient temperature about -65°C) at its peak (Fig. 30). This indicates that relatively small and/or short-lasting volumes of solid hydrometeors with high rime accretion rates resulted in positively charged graupel and positive CG strikes in this reflectivity core (Fig. 34b). On the other hand, reflectivity core B4 had large volumes of graupel up to >10 km and maintained this condition for a longer period than reflectivity core B2 (Fig. 33). This indicates that relatively large and long-lasting solid hydrometeor volumes with high rime accretion rates provided more opportunity to produce positive CG strikes in this reflectivity core (Fig. 34c).

From these facts, it is considered that high echo tops and maximum graupel volume heights are a necessary condition for positive CG strikes in reflectivity cores. In the thunderclouds analyzed here, positive CG strikes increased as graupel volumes became larger and longer lasting. These results can be explained by the noninductive charging mechanism of graupel particles (Saunders and Peck 1998); i.e., stronger reflectivity cores containing larger graupel particles have larger rime accretion rates at high altitudes, resulting in more opportunities for graupel particles to become positively charged. It is reasonable to assume that positively charged graupel particles in thunderclouds would be neutralized by the induced negative charge on the ground

through positive CG lighting strikes.

These findings in the application of the HC method show the appropriate performance of the HC method for isolated summer thunderclouds. To summarize construction (Section 3), validation (Section 4), and application parts (Section 5), the HC method for X-pol is effectively validated and is appropriate for the application to summer thunderclouds under Japan moist environment, which may contain solid hydrometeors (snow aggregates, ice crystals and graupel particles) with little or no hail. The HC method showed considerable performance to reveal the microphysical structures of thunderclouds and is expected to be applied to severe weather phenomena provided by convection with various hydrometeors (e.g., thunderclouds, supercells, meso-scale convective systems). When more precise microphysical observations with high temporal resolution are realized by phased array polarimetric radar in the future, more vivid space-time distribution of solid hydrometeors will be revealed with the more precise understanding of the phenomena.

7. Summary and conclusions

In this study, a hydrometeor classification (HC) method for X-band polarimetric radar (X-pol) was developed by reconstruction of previous studies and validated for solid hydrometeors (snow aggregates, ice crystals, and graupel). Then, it was applied to isolated summer thunderclouds in order to demonstrate its performance.

The HC method for X-pol is suitable for the observation of solid hydrometeors under moist environment producing little or no hail because X-pol has good capability of observing these solid hydrometeors. It identifies the most likely hydrometeor type at each radar sampling volume from eight categories: (1) drizzle, (2) rain, (3) wet snow aggregates, (4) dry snow aggregates (DS), (5) ice crystals (IC), (6) dry graupel (DG), (7) wet graupel (WG), and (8) rain–hail mixture (RH). The HC method uses radar reflectivity Z_h , differential reflectivity Z_{dr} , specific differential phase K_{dp} , and correlation coefficient ρ_{hv} as its main inputs, together with temperature, which can be obtained by soundings or numerical models, with some consideration of relative humidity as supplemental information. Membership functions (MBFs) for Z_h , Z_{dr} , K_{dp} , and ρ_{hv} were constructed by combining and reconstructing previous studies, and for temperature taking account of relative humidity for some hydrometeor categories.

Then, the HC method was validated against observations of solid hydrometeors (DG, DS, and IC). To validate the HC method for discriminating between DG and DS, ground observational data from a system that images the hydrometeors were used. DG was identified in the region where the values of K_{dp} and Z_{dr} were near-zero or negative, Z_h was relatively large ($\gtrsim 25$ dBZ) and ρ_{hv} was high ($\gtrsim 0.99$). On the other hand, dry

snow aggregates were identified in the region where the values of K_{dp} and Z_{dr} were near zero or positive, Z_h was relatively small ($\lesssim 25$ dBZ) and ρ_{hv} was moderate ($\gtrsim 0.98$). These HC results agreed well with hydrometeor types observed on the ground, both for graupel- and snow-dominant periods.

To validate the HC method for DS and IC, in situ observational data from balloon-borne instruments (hydrometeor videosondes: HYVISs) were used and compared the results of the HC for the dominant hydrometeor types observed with HYVIS. Above the freezing level, the results of HC were consistent with HYVIS observations except at one point where IC was identified by HC while dry snow aggregates were observed with HYVIS. A possible reason for the identification of IC by HC is that the number concentration of dry snow aggregates was very low and the Z_h value (< 20 dBZ) was much lower than the upper threshold of the Z_h MBF for DS. It is considered to be reasonable that the HC identified such a small Z_h area as IC. Through the validation using HYVIS, the HC results for DS and IC above the freezing level are consistent with the HYVIS observations.

Below the melting level, WG was identified by the HC at some points although raindrops were observed with HYVIS. At these points, the value of Z_h was relatively large and ρ_{hv} values were relatively low (< 0.97). Because these polarimetric characteristics are common for wet graupel and large oblate raindrops, it is difficult to distinguish these hydrometeors by HC at present. This problem may be solved if the three-dimensional distribution of DG, which may melt and become WG near the melting level, is obtained with high temporal and spatial resolution radar data. This will

be realized with phased-array polarimetric radars in the future.

Although the HC method was not validated for RH, it is considered that the partial applicability of the HC method for hail. Because of significant attenuation for X-pol, it is difficult to identify hail farther away from the radar behind the strong reflectivity core resulting from hail closer to the radar. However, it may be possible to detect the outer edge of the hail region by observing from different sides of the hail shaft with a network of X-pols, such as the Collaborative Adaptive Sensing of the Atmosphere (CASA) in the USA (McLaughlin et al. 2009) and the X-band Polarimetric Radar Information Network (XRAIN) in Japan (Maesaka et al. 2011). Thus, in the future, using a dense network of observations, the HC method could be applied to detect and locate hail.

To summarize the development part, the HC method for X-pol is valid under moist environments producing little or no hail, such as occur in East Asia, and could have applicability to HC in situations including hail as more detailed observations become available in the future.

Then, the HC method for X-pol was applied to two isolated summer thunderclouds in Japan to demonstrate its performance. The space–time distributions of solid hydrometeor volumes for dry snow (DS), ice crystal (IC), dry graupel (DG), and wet graupel (WG) in thunderclouds were examined. Cloud-to-ground (CG) lightning locations and polarities were obtained from the Lightning Location System (LLS) operated by Chubu Electric Power Co., Inc., which covers the observational area of the X-pol.

The analysis was conducted for two isolated summer thunderclouds in Japan; one on

26 July 2010 that produced almost solely negative CG strikes in reflectivity cores, and the other on 25 August 2010 that produced some positive CG strikes. Both of these thunderclouds had typical features of isolated summer thunderstorm; large volumes of graupel (DG and WG) were identified above the -10°C level in reflectivity cores when negative CG strikes occurred, and large volume of DS and IC were identified in the anvil area when positive CG strikes occurred.

All of the reflectivity cores in the thunderclouds examined here produced negative CG strikes. This includes reflectivity cores that also had positive CG strikes (PRCs) and those without positive CG strikes (NRCs). Compared with NRCs, PRCs had greater 30 and 40 dBZ echo top heights and maximum graupel volume heights (DG and WG). This result indicates that PRCs contained larger graupel particles with higher reflectivity values at higher altitudes than NRCs, implying high rime accretion rates and positive charged graupel.

Among PRCs, reflectivity cores with the first and second highest echo tops and graupel volume heights had 2 and 10 positive CG strikes, respectively. Echo top heights in the former increased and decreased rapidly. On the other hand, the latter had large volumes of graupel above the -45°C level and these volumes were maintained for a longer time than the former. This indicates that when high and relatively long-lasting graupel volumes occur alongside high rime accretion rates, there is more opportunity for graupel to acquire a positive charge, resulting in positive CG strikes in reflectivity cores. Thus, high echo top and maximum graupel volume heights, implying high rime accretion rates, are prerequisites for positive CG strikes in reflectivity cores. Positive

CG strikes increased with the volume and duration of high rime accretion rates.

The application of the HC to summer thunderclouds demonstrate the performance of the HC method developed in this study and the effectiveness of examining the space–time distribution of solid hydrometeors in thundercloud reflectivity cores at high spatial and temporal resolution using polarimetric radar. This approach can enhance our understanding of the charge distribution in thunderclouds through CG lightning activity, and contribute to future understanding of lightning neutralization mechanisms associated with solid hydrometeor distribution in thunderclouds.

To summarize the development and application parts, the HC method for X-pol is effectively validated and is appropriate for the application to summer thunderclouds under Japan moist environment, which may contain solid hydrometeors (snow aggregates, ice crystals and graupel particles) with little or no hail. The HC method showed considerable performance to reveal the microphysical structures of thunderclouds and is expected to be applied to severe weather phenomena provided by convection with various hydrometeors (e.g., thunderclouds, supercells, meso-scale convective systems). When more precise microphysical observations with high temporal resolution are realized by phased array polarimetric radar in the future, more vivid space-time distribution of solid hydrometeors will be revealed with the more precise understanding of the phenomena.

Acknowledgements

I would like to express a deep gratitude to my supervisor, Prof. Hiroshi Uyeda, an emeritus professor of Nagoya University, for his passionate instruction and encouragement throughout my research life. I would like to express gratitude to my secondary supervisor, Prof. Kazuhisa Tsuboki, Prof. Nobuhiro Takahashi, and Dr. Taro Shinoda, ISEE, Nagoya University, for their fruitful discussions and their valuable suggestions. I thank to Dr. Sachie Kanada of ISEE for her fruitful discussion, suggestions and encouragement. I am grateful to Dr. Yukari Shusse of National Research Institute for Earth Science and Disaster Resilience, for her help in analysis of the data and providing fruitful advice on the polarimetric radar. I am also grateful to Dr. Tadayasu Ohigashi of ISEE for his arrangement of polarimetric radar observations in Horuriku, Okinawa, and Tokai for the validation and applications of the HC method. I extend my thanks to members of Laboratory of Meteorology, ISEE, Nagoya University for their assistance with the observations and data analyses. I would like to thank Dr. Ken-ichiro Muramoto and Dr. Mamoru Kubo of Kanazawa University for the data acquisition of ground based imaging system for the validation observations in Hokuriku. I also thank to Mr. Hiroto Takehuchi of Nagoya University for providing graupel/snow particle number counting data of the Hokuriku ground observations. I am grateful to Chubu Electric Power Co., Inc. for providing data from their Lightning Location System for the summer thundercloud observations in Tokai. This study was supported by Research Fellow of Japan Society for the Promotion of Science (JSPS) Grants-in-Aid for Scientific Research (10J08853) and the Ministry of Education,

Culture, Sports, Science and Technology, Japan, program: “Formation of a virtual laboratory for diagnosing the earth's climate system”. The observations were supported by JSPS Grant-in-Aid for Young Scientists (B) (20740271, led by Dr. Tadayasu Ohigashi), JSPS Grant-in-Aid for Scientific Research (S) (22226010, led by Prof. Eiichi Nakakita), (B) (22340136, led by Prof. Kazuhisa Tsuboki), and (A) (24253006, led by Prof. Hiroshi Uyeda) and Program to Disseminate Tenure Tracking System in University of Tsukuba “Study on precipitation and meteorological disasters” (Dr. Yasutaka Wakazuki). Grid Analysis and Display System (GrADS) software was used to draw the figures.

References

- Al-Sakka, H., A. Boumahmoud, B. Fradon, S. J. Frasier, and P. Tabary, 2013: A new fuzzy logic hydrometeor classification scheme applied to the French X-, C-, and S-band polarimetric radars. *J. Appl. Meteor. Climatol.*, **52**, 2328–2344.
- Aydin, K., T. A. Seliga, and V. Balaji, 1986: Remote sensing of hail with a dual linear polarization radar. *J. Climate Appl. Meteor.*, **25**, 1475–1484.
- Beard, K. V., and C. Chuang, 1987: A new model for the equilibrium shape of raindrops. *J. Atmos. Sci.*, **44**, 1509–1524.
- Bechini, R., L. Baldini, V. Chandrasekar, 2013: Polarimetric radar observations in the ice region of precipitating clouds at C-band and X-band radar frequencies. *J. Appl. Meteor. Climatol.*, **52**, 1147–1169.
- Bringi, V. N., and V. Chandrasekar, 2001: *Polarimetric Doppler Weather Radar: Principles and Applications*. Cambridge University Press, 636 pp.
- Brooks, I. M., C. P. R. Saunders, R. P. Mitzeva, and S. L. Peck, 1997: The effect on thunderstorm charging of the rate of rime accretion by graupel. *Atmos. Res.*, **43**, 277–295.
- Carey, L. D., and S. A. Rutledge, 1996: A multiparameter radar case study of the microphysical and kinematic evolution of a lightning producing storm. *Meteorol. Atmos. Phys.*, **59**, 33–64.
- Carey, L. D., and S. A. Rutledge, 2000: The relationship between precipitation and lightning in tropical island convection: A C-band polarimetric radar study. *Mon. Wea. Rev.*, **128**, 2687–2710.

- Chandrasekar, V., R. Keränen, S. Lim, and D. Moisseev, 2013: Recent advances in classification of observations from dual polarization weather radars. *Atmos. Res.*, **119**, 97–111.
- Cressman, G. P., 1959: An operational objective analysis system. *Mon. Wea. Rev.*, **87**, 367–374.
- Dolan, B., and S. A. Rutledge, 2009: A theory-based hydrometeor identification algorithm for X-band polarimetric radars. *J. Atmos. Oceanic Technol.*, **26**, 2071–2088.
- Dolan, B., S. A. Rutledge, S. Lim, V. Chandrasekar, and M. Thurai, 2013: A robust C-band hydrometeor identification algorithm and application to a long-term polarimetric radar dataset. *J. Appl. Meteor. Climatol.*, **52**, 2162–2186.
- Doviak, R. J., and D. S. Zrnić, 1993: Doppler Radar and Weather Observations. Academic Press, 562 pp.
- Fuquay, D. M., 1982: Positive cloud-to-ground lightning in summer thunderstorm. *J. Geophys. Res.*, **87**, 7131–7140.
- Gorgucci, E., G. Scarchili, and V. Chandrasekar, 1994: A robust estimator of rainfall rate using differential reflectivity. *J. Atmos. Oceanic Technol.*, **11**, 586–592.
- Hall, M. P. M., S. M. Cherry, J. W. F. Goddard, and G. R. Kennedy, 1980: Rain drop sizes and rainfall rate measured by dual-polarization radar. *Nature*, **285**, 195–198.
- Hall, M. P. M., J. W. F. Goddard, and S. M. Cherry, 1984: Identification of hydrometeors and other targets by dual-polarization radar. *Radio Sci.*, **19**, 132–140.
- Houze, R. A., Jr., 1993: *Cloud Dynamics*. Academic Press, CA, 573 pp.

- Höller, H., V. N. Bringi, J. Hubbert, M. Hagan, and P. F. Meischner, 1994: Life cycle and precipitation formation in a hybrid-type hailstorm revealed by polarimetric and Doppler radar measurements. *J. Atmos. Sci.*, **51**, 2500–2522.
- Ishizaka, M., H. Motoyoshi, S. Nakai, T. Shiina, T. Kumakura, and K. Muramoto, 2013: A new method for identifying the main type of hydrometeors contributing to snowfall from measured size-fall speed relationship. *J. Meteor. Soc. Japan*, **91**, 747–762.
- Jameson, A. R., 1992: The effect of temperature on attenuation correction schemes in rain using polarization propagation differential phase shift. *J. Appl. Meteor.*, **31**, 1106–1118.
- Keenan, T. D., 2003: Hydrometeor classification with a C-band polarimetric radar. *Aust. Meteor. Mag.*, **52**, 23–31.
- Kennedy, P. C., and S. A. Rutledge, 2011: S-band dual-polarization radar observations of winter storms. *J. Appl. Meteor. Climatol.*, **50**, 844–858.
- Khvorostyanov, V. I., and J. A. Curry, 2005: Fall velocities of hydrometeors in the atmosphere: Refinements to a continuous analytical power law. *J. Atmos. Sci.*, **62**, 4343–4357.
- Kikuchi, K., T. Kameda, K. Higuchi c, A. Yamashita, and working group members for new classification of snow crystals, 2013: A global classification of snow crystals, ice crystals, and solid precipitation based on observations from middle latitudes to polar regions. *Atmos. Res.*, **132–133**, 460–472.
- Knight, C. A., and N. C. Knight, 1973: Conical graupel. *J. Atmos. Sci.*, **30**, 118–124.

- Kubo, M., K. Seto, K. Muramoto, Y. Fujiyoshi, T. Shinoda and T. Ohigashi, 2009: Shape classification of snow particle into snowflake and graupel using image processing. Preprints, *ICCAS-SICE, 2009*, 5451–5456.
- Lang, T. J., and S. A. Rutledge, 2002: Relationship between convective storm kinematics, precipitation, and lightning. *Mon. Wea. Rev.*, **130**, 2492–2506.
- Larsen, H. R., and E. J. Stansbury, 1974: Association of lightning flashes with precipitation cores extending to height 7 km. *J. Atmos. Terr. Phys.*, **36**, 1547–1553.
- Lim, S., V. Chandrasekar, and V. N. Bringi, 2005: Hydrometeor classification system using dual-polarization radar measurements: Model improvements and in situ verification. *IEEE Trans. Geosci. Remote Sens.*, **43**, 792–801.
- Liu, H., and V. Chandrasekar, 2000: Classification of hydrometeors based on polarimetric radar measurements: Development of fuzzy logic and neuro-fuzzy systems, and in situ verification. *J. Atmos. Oceanic Technol.*, **17**, 140–164.
- Locatelli, J. D., and P. V. Hobbs, 1974: Fall speeds and masses of solid precipitation particles. *J. Geophys. Res.*, **79**, 2185–2197.
- López, R. E., and J.-P. Aubagnac, 1997: The lightning activity of a hailstorm as a function of changes in its microphysical characteristics inferred from polarimetric radar observations. *J. Geophys. Res.*, **102**, 16 799–16 813.
- Maesaka, T., M. Maki, K. Iwanami, S. Tsuchiya, K. Kieda, and A. Hoshi, 2011: Operational rainfall estimation by X-band MP radar network in MLIT, Japan. Preprints, *35th Conf. on Radar Meteorology*, Pittsburgh, PA, Amer. Meteor. Soc., P11.142. [Available online at

https://ams.confex.com/ams/35Radar/webprogram/Manuscript/Paper191685/35RADAR_Maesaka.pdf.]

- Magono, C., and C. W. Lee, 1966: Meteorological classification of natural snow crystals. *J. Fac. Sci., Hokkaido Univ., Series VII, Geophysics*, **2**, 321–335.
- Marshall, T. C., W. D. Rust, W. P. Winn, and K. E. Gilbert, 1989: Electrical structure in two thunderstorm anvil clouds. *J. Geophys. Res.*, **94**, 2171 - 2181.
- Marzano, F. S., D. Scaranari, M. Celano, P. P. Alberoni, G. Vulpiani, and M. Montopoli, 2006: Hydrometeor classification from dual polarized weather radar: Extending fuzzy logic from S-band to C-band. *Adv. Geosci.*, **7**, 109–114.
- Marzano, F. S., D. Scaranari, M. Montopoli, and G. Vulpiani, 2008: Supervised classification and estimation of hydrometeors from C-band dual-polarized radars: A Bayesian approach. *IEEE Trans. Geosci. Remote Sens.*, **46**, 85–98.
- Matsumoto, S., K. Ninomiya, and S. Yoshizaki, 1971, Characteristic features of “Baiu” front associated with heavy rainfall. *J. Meteor. Soc. Japan*, **49**, 267-281.
- Matsuo, T., and Y. Sasyo, 1981: Melting of snowflakes below freezing level in the atmosphere. *J. Meteor. Soc. Japan*, **59**, 10–25.
- Matsuo, T., Y. Sasyo, and Y. Sato, 1981: Relationship between types of precipitation on the ground and surface meteorological elements. *J. Meteor. Soc. Japan*, **59**, 462–476.
- McLaughlin, D., D. Pepyne, V. Chandrasekar, B. Philips, J. Kurose, M. Zink, K. Droegemeier, S. Cruz-Pol, F. Junyent, J. Brotzge, D. Westbrook, N. Bharadwaj, Y. Wang, E. Lyons, K. Hondl, Y. Liu, E. Knapp, M. Xue, A. Hopf, K. Kloesel, A.

- DeFonzo, P. Kollias, K. Brewster, R. Contreras, B. Dolan, T. Djaferis, E. Insanic, S. Frasier, and F. Carr, 2009: Short-wavelength technology and the potential for distributed networks of small radar systems. *Bull. Amer. Meteor. Soc.*, **90**, 1797–1817.
- Michimoto, K., 1991: A study of radar echoes and their relation to lightning discharge of thunderclouds in the Hokuriku district, Part I: Observation and analysis of thunderclouds in summer and winter. *J. Meteorol. Soc. Japan.*, **69**, 327–336.
- Mizuno, H., 1992: Statistical characteristics of graupel precipitation over the Japan Island. *J. Meteor. Soc. Japan*, **70**, 115–120.
- Momozawa, K., F. Suzuki, H. Tsuji, and Y. Onozuka, 2012: Evaluation of the new LS7001 network in the Chube Region of Japan. Proc. 22nd international Lightning Detection Conference / 4th International Lightning Meteorology Conference. [Available online at <http://www.vaisala.com/en/events/ildcilmc/Documents/Network%20Performance/Evaluation%20of%20the%20New%20LS7001%20Network%20in%20the%20Chubu%20Region%20of%20Japan.pdf>].
- Murakami, M., and T. Matsuo, 1990: Development of the hydrometeor videosonde. *J. Atmos. Oceanic Tech.*, **7**, 613–620.
- Muramoto, K., 1995: Determination of shape and fall velocity of raindrops by image processing. *IEICE Trans. Inf. Syst.*, **E78-D(8)**, 1051-1057.
- Ninomiya, K., 1984: Characteristics of Baiu front as a predominant subtropical front in the summer northern hemisphere. *J. Meteor. Soc. Japan*, **62**, 880–894.

- Ninomiya, K., and T. Akiyama, 1992: Multi-scale features of Baiu, the summer monsoon over Japan and the East Asia. *J. Meteor. Soc. Japan*, **70**, 467–495.
- Ohigashi, T., K. Tsuboki, Y. Shusse, and H. Uyeda, 2014: An intensification process of a winter broad cloud band on a flank of the mountain region along the Japan-Sea coast. *J. Meteor. Soc. Japan*, **92**, 71–93.
- Oue, M., H. Uyeda, and Y. Shusse, 2010: Two types of precipitation particle distribution in convective cells accompanying a Baiu frontal rainband around Okinawa Island, Japan. *J. Geophys. Res.*, **115**, D02201, doi:10.1029/2009JD011957.
- Oue, M., T. Ohigashi, K. Tsuboki, and E. Nakakita, 2015: Vertical distribution of precipitation particles in Baiu frontal stratiform intense rainfall around Okinawa Island, Japan. *J. Geophys. Res. Atmos.*, **120**, 5622–5637.
- Park, H., A. V. Ryzhkov, D. S. Zrnic, and K.-E. Kim, 2009: The hydrometeor classification algorithm for the polarimetric WSR-88D: Description and application to an MCS. *Wea. Forecasting*, **24**, 730–748.
- Rasmussen, R. M., and A. J. Heymsfield, 1987: Melting and shedding of graupel and hail. Part I: Model physics. *J. Atmos. Sci.*, **44**, 2754–2763.
- Reynolds, S. E., and M. Brook, 1956: Correlation of the initial electric field and the radar echo in thunderstorms. *J. Meteor.*, **13**, 376–380.
- Rust, W. D., W. L. Tayloy, and D. R. MacGorman, 1981a: Research on electrical properties of severe thunderstorms in the Great Plains. *Bull. Amer. Meteor. Soc.*, **62**, 1286–1293.
- Rust, W. D., D. R. MacGorman, and R. T. Arnold, 1981b: Positive cloud-to-ground

- lightning flashes in severe storms. *Geophys. Res. Lett.*, **8**, 791-794.
- Sachidananda, M., and D. S. Zrnić, 1986: Differential propagation phase shift and rainfall rate estimation. *Radio Sci.*, **21**, 235–247.
- Saunders, C. P. R., W. D. Keith, and R. P. Mitzeva, 1991: The effect of liquid water on thunderstorm charging. *J. Geophys. Res.*, **96**, 11007–11017.
- Saunders, C. P. R., and S. L. Peck, 1998: Laboratory studies of the influence of the rime accretion rate on charge transfer during graupel/crystal collisions. *J. Geophys. Res.*, **103**, 13949–13956.
- Seliga, T. A., and V. N. Bringi, 1976: Potential use of radar differential reflectivity measurements at orthogonal polarizations for measuring precipitation. *J. Appl. Meteor.*, **15**, 69–76.
- Seliga, T. A., and V. N. Bringi, 1978: Differential reflectivity and differential phase shift: Application in radar meteorology. *Radio Sci.*, **13**, 271–275.
- Shusse, Y., K. Nakagawa, N. Takahashi, S. Satoh, and T. Iguchi, 2009: Characteristics of polarimetric radar variables in three types of rainfalls in a baiu front event over the East China Sea. *J. Meteor. Soc. Japan*, **87**, 865–875.
- Snyder, J. C., H. B. Bluestein, G. Zhang, and S. J. Frasier, 2010: Attenuation correction and hydrometeor classification of high-resolution, X-band, dual-polarized mobile radar measurements in severe convective storms. *J. Atmos. Oceanic Technol.*, **27**, 1979–2001.
- Stolzenburg, M., 1994: Observation of high flash densities of positive lightning in summertime thunderstorms. *Mon. Wea. Rev.*, **122**, 1740–1750.

- Stolzenburg, M., and T. C. Marshall, 1998: Charged precipitation and electric field in two thunderstorms. *J. Geophys. Res.*, **103(D16)**, 19,777–19,790, doi:10.1029/98JD01675.
- Straka, J. M., 1996: Hydrometeor fields in a supercell storm as deduced from dual-polarization radar. Preprints, *18th Conf. on Severe Local Storms*, San Francisco, CA, Amer. Meteor. Soc., pp. 551–554.
- Straka, J. M., and D. S. Zrnić, 1993: An algorithm to deduce hydrometeor types and contents from multi-parameter radar data. Preprints, *26th Int. Conf. on Radar Meteorology*, Norman, OK, Amer. Meteor. Soc., pp. 513–515.
- Straka, J. M., D. S. Zrnić, and A. V. Ryzhkov, 2000: Bulk hydrometeor classification and quantification using polarimetric radar data: Synthesis of relations. *J. Appl. Meteor.*, **39**, 1341–1372.
- Suzuki, K., K. Shimizu, T. Ohigashi, K. Tsuboki, S. Oishi, S. Kawamura, K. Nakagawa, K. Yamaguchi, and E. Nakakita, 2012: Development of a new videosonde observation system for in-situ precipitation particle measurements. *SOLA*, **8**, 1-4, doi:10.2151/sola.2012-001.
- Suzuki, K., M. Matsuo, E. Nakano, S. Shigeto, K. Yamaguchi, and E. Nakakita, 2014: Graupel in the different developing stages of Baiu monsoon clouds observed by videosondes. *Atmos. Res.*, **142**, 100-110.
- Takahashi, T., 1978: Riming electrification as a charge generation mechanism in thunderstorms. *J. Atmos. Sci.*, **35**, 1536–1548.
- Takahashi, T., 1990: Near absence of lightning in tropical rainfall producing

- Micronesian thunderstorms. *Geophys. Res. Lett.*, **17**, 2381–2384.
- Tessendorf, S. A., L. J. Miller, K. C. Wiens, and S. A. Rutledge, 2005: The 29 June 2000 supercell observed during STEPS. Part I: Kinematics and microphysics. *J. Atmos. Sci.*, **62**, 4127–4150.
- Thurai, M., G. J. Huang, and V. N. Bringi, 2007: Drop shapes, model comparisons, and calculations of polarimetric radar parameters in rain. *J. Atmos. Oceanic Technol.*, **24**, 1019–1032.
- Thompson, E. J., S. A. Rutledge, B. Dolan, V. Chandrasekar, and, B. L. Cheong, 2014: A dual-polarization radar hydrometeor classification algorithm for winter precipitation. *J. Atmos. Oceanic Technol.*, **31**, 1457–1481.
- Vivekanandan, J., D. S. Zrnic, S. M. Ellis, R. Oye, A. V. Ryzhkov, and J. Straka, 1999: Cloud microphysics retrieval using S-band dual-polarization radar measurements. *Bull. Amer. Meteor. Soc.*, **80**, 381–388.
- Wakimoto, R. M., and V. N. Bringi, 1988: Dual-polarization observations of microbursts associated with intense convection: the 20 July storm during the MIST Project. *Mon. Wea. Rev.*, **116**, 1521–1539.
- Wang, Y., and V. Chandrasekar, 2009: Algorithm for estimation of the specific differential phase. *J. Atmos. Oceanic Technol.*, **26**, 2565–2578.
- Wiens, K. C., S. A. Rutledge, and S. A. Tessendorf, 2005: The 29 June 2000 supercell observed during STEPS. Part II: Lightning and charge structure. *J. Atmos. Sci.*, **62**, 4151–4177.
- Williams, E. R., M. E. Weber, and R. E. Orville, 1989: The relationship between

lightning type and convective state of thunderclouds. *J. Geophys. Res.*, **94**, 13213–13220.

Workman, E. J., and S. E. Reynolds, 1949: Electrical activity as related to thunderstorm cell growth. *Bull. Amer. Meteor. Soc.*, **30**, 142–144.

Yamada, H., H. Uyeda, K. Kikuchi, M. Maki, and K. Iwanami, 2004: Dual-Doppler radar observations on factors causing differences in the structure of snow clouds during winter monsoon surges. *J. Meteor. Soc. Japan*, **82**, 179–206.

Tables and Figures

Table 1. Specifications of the Nagoya University X-pol.

Transmitted frequency	9415 MHz / 9375 MHz *
Antenna size	2.0 m
Beam width	1.2°
Transmitter	Type Solid state component
	Peak power 200 W
Pulse width	1 μ s (within 4.8 km)
	29.1 μ s (beyond 4.8 km, using pulse compression)
Transmission	45 H&V simultaneous or H only or V only
Max range	61.8 km
Range gate spacing	150 m
Beam spacing	1.17° in azimuth (PPI)
	0.36° in elevation (RHI)
Rotation rate	3.0 rpm (PPI) , 0.6 rpm (RHI)
PRF	2000 Hz / 1600 Hz (dual PRF)
Number of pulse integration	130/104 (PPI), 200/160 (RHI)
Nyquist velocity	15.9 ms ⁻¹ / 12.7 ms ⁻¹

* Either of two Nagoya University X-pols, which have the same specifications except for transmitted frequencies, was used for each observation.

Table 2. Parameters for temperature MBFs. See text for details of T_1 and T_2 , the temperatures at which solid hydrometeors begin to melt (Eq. (11)) and snow aggregates completely melt (Eq. (12)), respectively.

Hydrometeor	$m-a$	$m+a$	m	a	B
DZ	T_1	50	$(T_1+50)/2$	$(50-T_1)/2$	29.9
RN	T_2	50	$(T_2+50)/2$	$(50-T_2)/2$	29.9
WS	T_1	T_2	$(T_1+T_2)/2$	$(T_2-T_1)/2$	3.9
DS	-50	T_1	$(-50+T_1)/2$	$(T_1-(-50))/2$	29.9
IC	-100	T_1	$(-100+T_1)/2$	$(T_1-(-100))/2$	58.6
DG	-100	T_1	$(-100+T_1)/2$	$(T_1-(-100))/2$	58.6
WG	-15	10	-2.5	12.5	12.6
RH	-10	25	7.5	17.5	12.6

Table 3. List of previous studies used to determine the lower and upper thresholds of MBFs.

Hydrometeor	Z_h , Z_{dr} , K_{dp} , and ρ_{hv}	Temperature
DZ	D09	Matsuo and Sasyo (1981)
RN	D09	Matsuo et al. (1981)
WS	L00	Matsuo and Sasyo (1981) and Matsuo et al. (1981)
DS	D09	Matsuo and Sasyo (1981)
IC	D09, Kennedy and Rutledge (2011), and Bechini et al. (2013)	Matsuo and Sasyo (1981)
DG	D09 and Yamada et al., (2004)	Matsuo and Sasyo (1981)
WG	D09	Tessendorf et al. (2005)
RH	S10	Keenan (2003)

Table 4. List of reflectivity cores of Thunderclouds A and B in 2010.

No.	Generation Time	Duration [min]	Nnumber		Maximum height [km]			
			+CG	−CG	30dBZ	40dBZ	DG	WG
A1	2042 JST 26 JUL	30	0	22	10.5	8.0	11.0	9.0
A2	2106 JST 26 JUL	24	1	27	11.5	8.5	12.0	9.5
A3	2106 JST 26 JUL	24	0	6	9.5	7.5	10.5	8.0
A4	2112 JST 26 JUL	12	0	4	9.5	8.5	9.5	9.0
B1	1554 JST 25 AUG	18	2	8	12.5	9.5	13.0	11.0
B2	1600 JST 25 AUG	24	2	58	16.5	16.0	16.0	11.0
B3	1606 JST 25 AUG	30	2	60	13.0	11.0	13.0	11.0
B4	1624 JST 25 AUG	36	10	60	14.5	11.0	15.5	11.0
B5	1642 JST 25 AUG	30	1	23	13.5	11.0	13.5	11.0
B6	1654 JST 25 AUG	42	3	88	13.5	11.0	14.0	11.0

Table 5. Time series of 6-minute accumulated numbers of positive CG strike numbers in each reflectivity core (A1–A4) and the anvil area of Thundercloud A from 2054 to 2124 JST, 26 July 2010.

	2054	2100	2106	2112	2118	2124
A1	0	0	0			
A2			0	1	0	0
A3			0	0	0	0
A4				0	0	0
Anvil	0	0	0	0	2	0

Table 6. Same as Table 5, but for each reflectivity core (B1–B6) and the anvil area of Thundercloud B from 1600 to 1700 JST, 25 August 2010.

	1600	1606	1612	1618	1624	1630	1636	1642	1648	1654	1700
B1	0	1	1								
B2	0	0	1	1	0						
B3		0	0	0	1	0	1				
B4					0	1	4	4	0	1	0
B5								0	0	1	0
B6										0	1
Anvil	0	0	5	9	5	19	15	4	0	0	0

Table 7. Same as Table 6, but from 1706 to 1736 JST, 25 August 2010.

	1706	1712	1718	1724	1730	1736
B1						
B2						
B3						
B4						
B5	0	0				
B6	0	1	1	0	0	0
Anvil	0	0	0	0	0	0

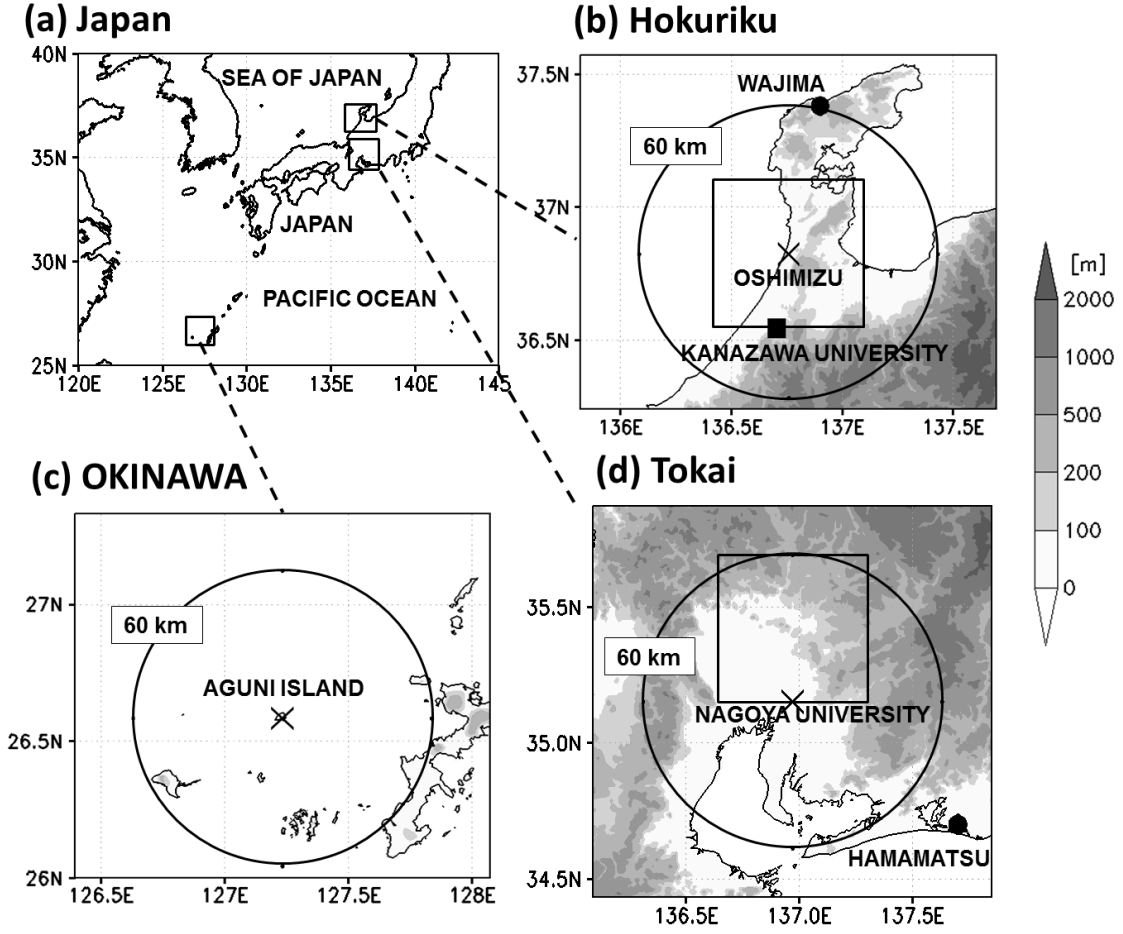


Fig. 1. The observational ranges of the Nagoya University X-pol for validation of the HC method using (b) ground observations in Hokuriku and (c) in situ observations in Okinawa described in Sections 4, and (d) application to summer thunderclouds in Tokai described in Section 5. Crosses indicate the locations of the X-pol (Oshimizu for Hokuriku observation, Aguni Island for Okinawa observation, and Nagoya University for Tokai observation). The solid square and circle in (b) indicate the locations of the imaging system at Kanazawa University and the sounding point at Wajima, respectively. The square frame in (b) indicates the range of PPI area shown in Fig. 3. The solid circle in (d) indicates the locations of sounding point at Hamamatsu. The square frame in (d) denotes the area of Figs. 19 and 22.

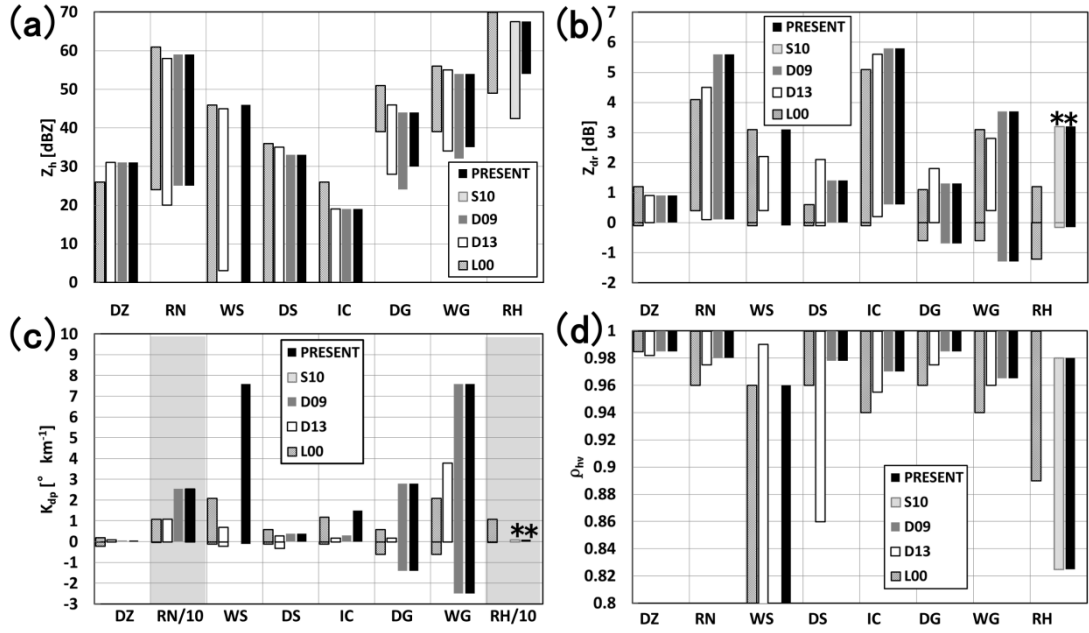


Fig. 2. The lower and upper thresholds of half-value ranges of MBFs for (a) Z_h , (b) Z_{dr} , (c) K_{dp} , and (d) ρ_{hv} in L00, D13, D09, S10, and the present study for the eight hydrometeor categories listed in the text. Values of K_{dp} divided by 10 for RN and RH are shown in (c) because these hydrometeors have a large range of K_{dp} values. Note that upper thresholds of MBFs of RH for Z_{dr} and K_{dp} in S10 and the present study (asterisks) are functions of Z_h and are shown for $Z_h = 60$ dBZ in (b) and (c). See Table 3 in S10 for details.

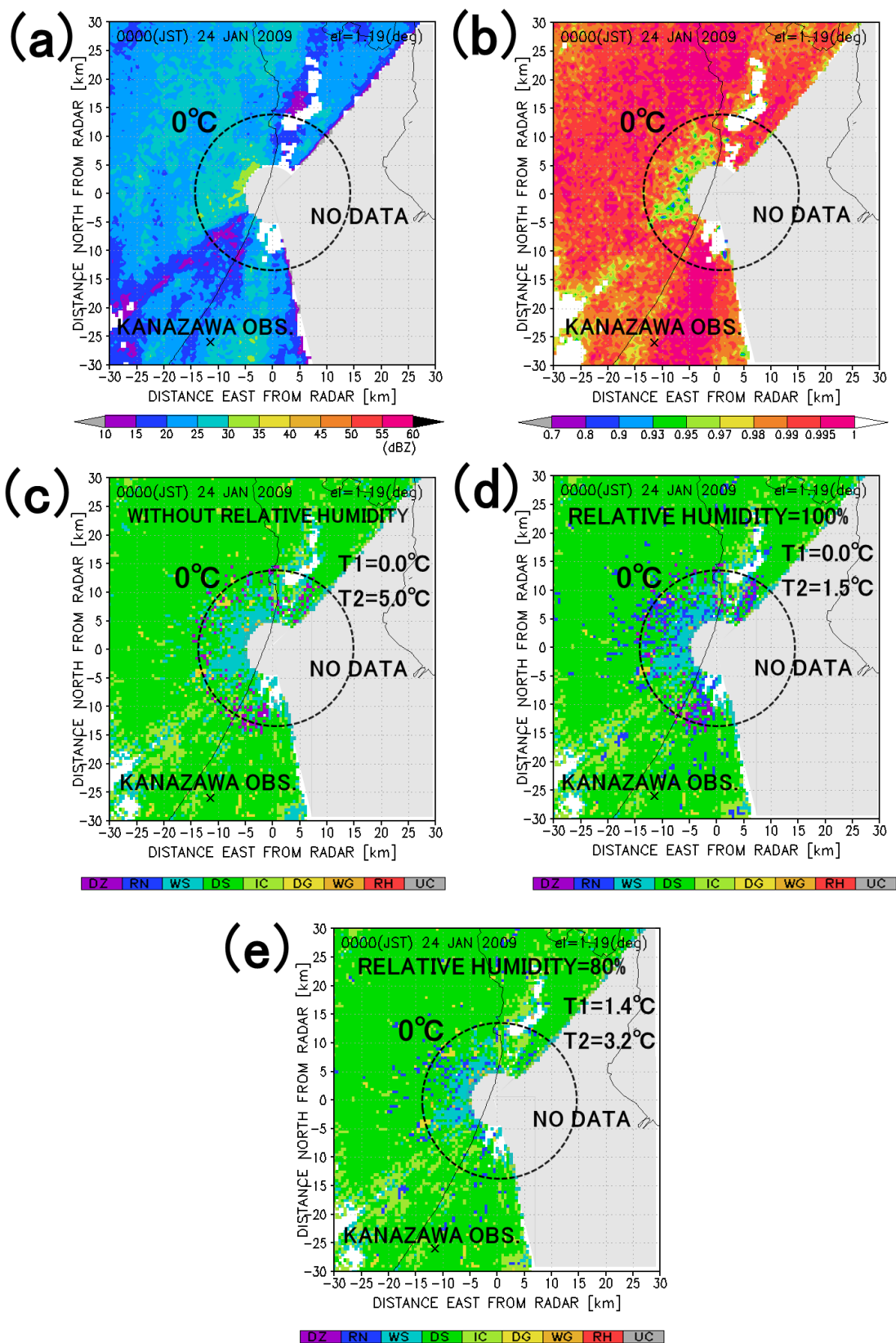


Fig. 3. (a) Z_h , (b) ρ_{hv} and results of HC (c) without considering relative humidity, and considering surface relative humidity of (d) 100% and (e) 80% in PPI (elevation of 1.2°) at 0000 JST 24 January 2009 (depicted in $0.5 \text{ km} \times 0.5 \text{ km}$ resolutions). Dotted lines denote the isotherms of 0°C estimated from surface temperature at Kanazawa local meteorological observatory (KANAZAWA OBS.: crosses) and mesoscale reanalysis data from the Japan Meteorological Agency. The gray-shaded areas denote no-data areas due to beam blanking to avoid beam reflection from near buildings.

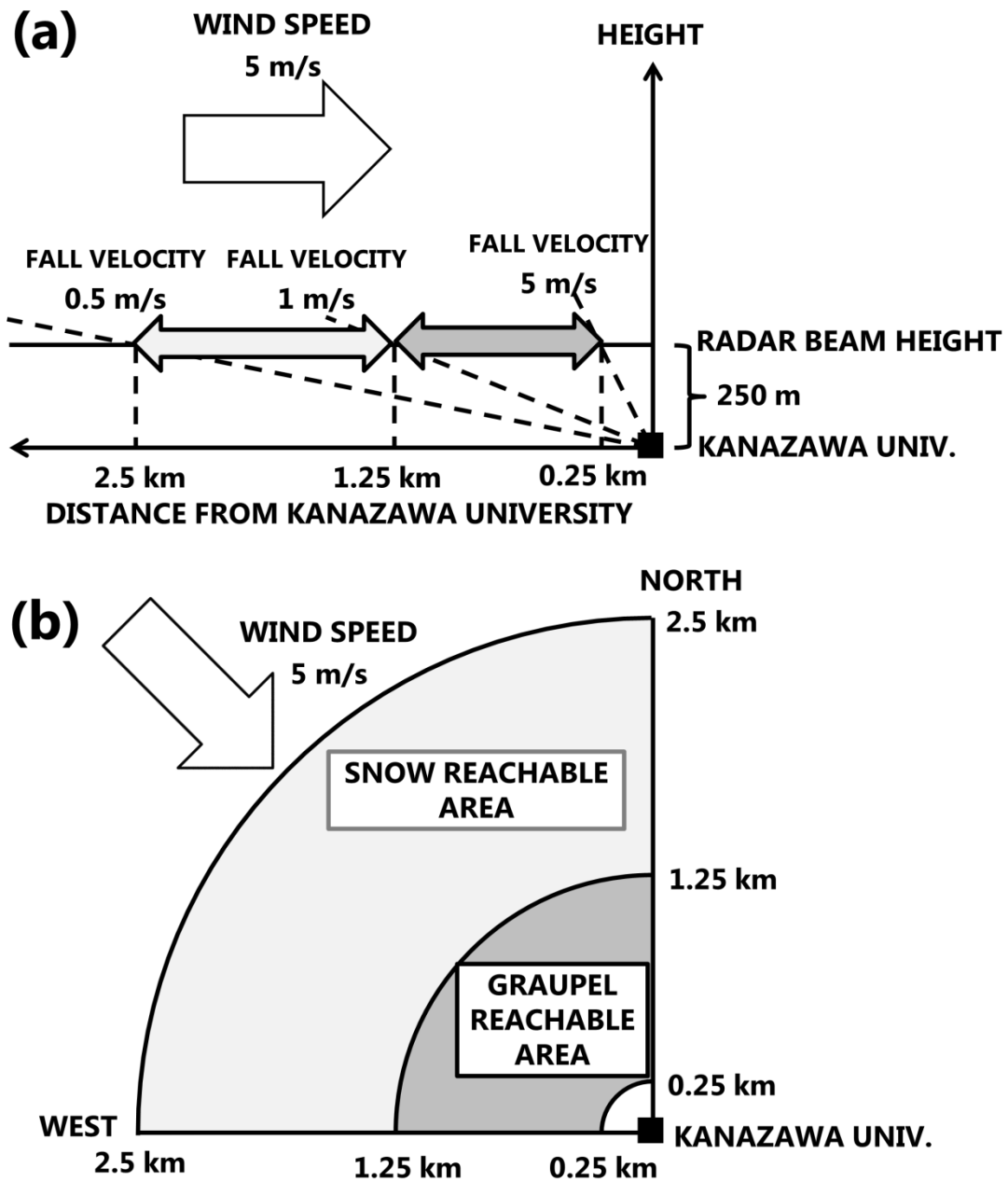


Fig. 4. Schematic illustration of graupel (dark gray) and snow (light gray) reachable areas to the imaging system at Kanazawa University in (a) vertical cross section along the wind direction and (b) horizontal cross section at radar beam height (about 250 m above the imaging system at Kanazawa University) in the case of 15 January 2009. The wind speed was $\sim 5 \text{ m s}^{-1}$ during the analysis period. Fall velocities of graupel and snow

particles are assumed to be $1\text{--}5 \text{ m s}^{-1}$ and $0.5\text{--}1 \text{ m s}^{-1}$, respectively. The tracks of falling graupel and snow particles are shown by the dotted lines in (a). Graupel particles in the range shaded dark gray and snow aggregates in the range shaded light gray can fall into the imaging system at Kanazawa University. The wind direction is assumed to fluctuate within $\pm 45^\circ$ from a northwesterly direction.

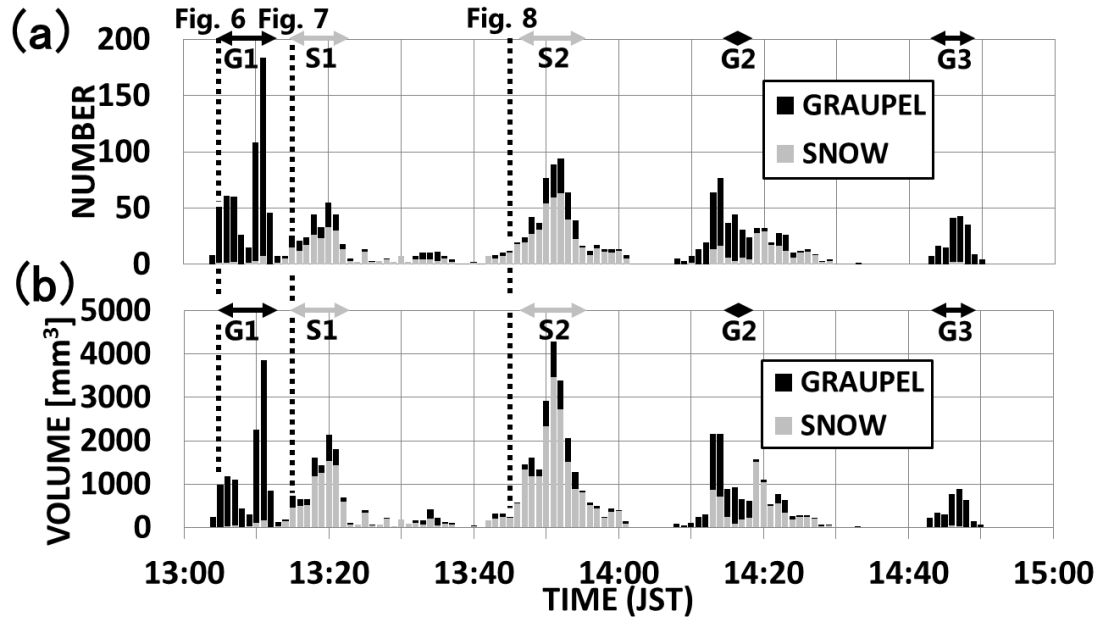


Fig. 5. Time series of 1-minute accumulated (a) numbers and (b) total equivalent volumes of graupel (black bars) and snow (gray bars) observed with the ground-based imaging system at Kanazawa University from 1300 to 1500 JST 15 January 2009. Horizontal black and gray arrows indicate periods when graupel (Periods G1, G2, and G3) and snow (Periods S1 and S2) were dominant, respectively. Vertical dotted lines indicate times of PPI scans shown in Figs. 6, 7, and 8.

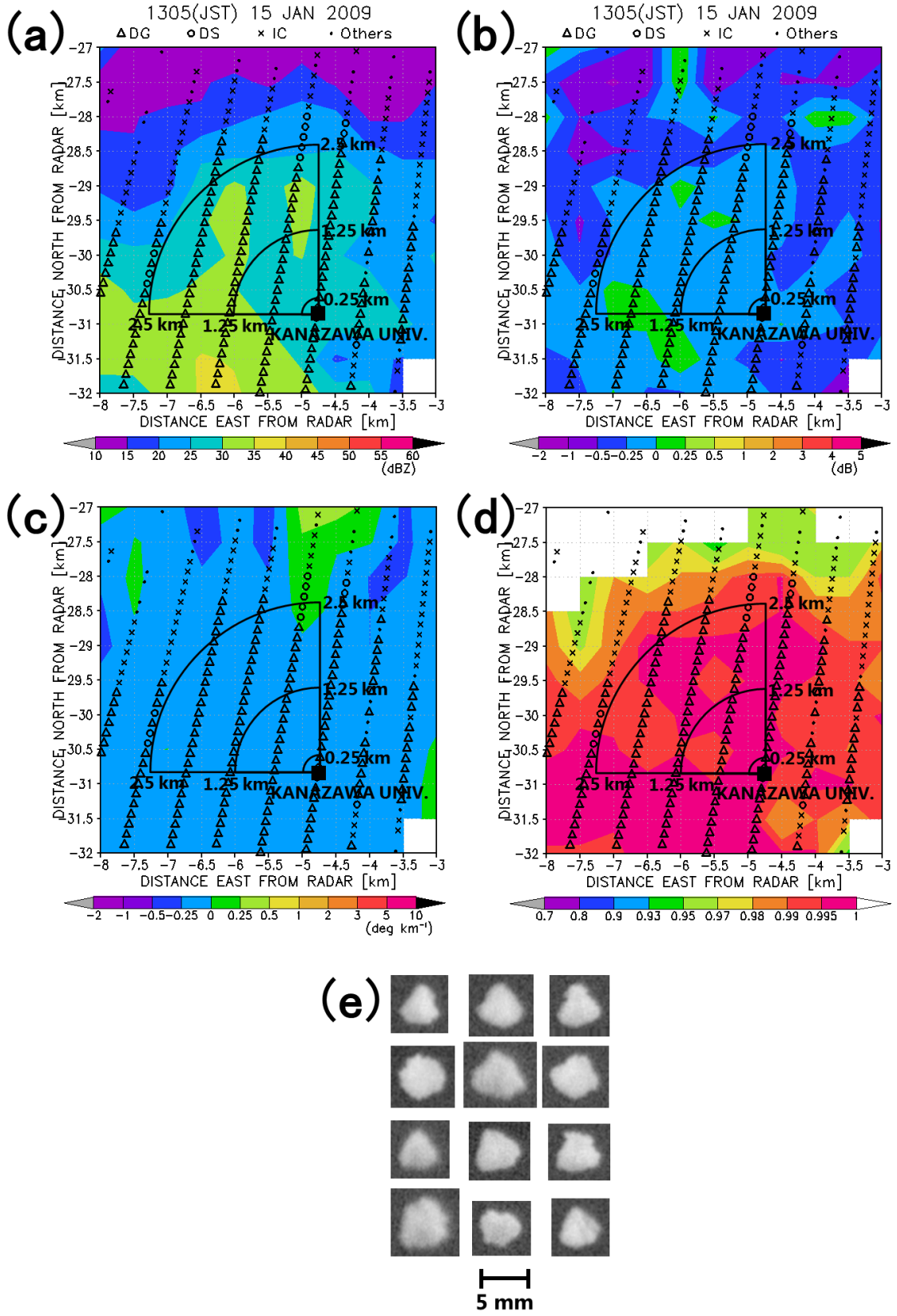


Fig. 6. (a) Z_h , (b) Z_{dr} , (c) K_{dp} , and (d) ρ_{hv} (depicted in 0.5 km \times 0.5 km resolutions)

superposed on the result of HC for all radar sampling volumes in PPI at the lowest elevation (0.6°) at 1305 JST 15 January 2009 and (e) examples of hydrometeor images obtained by ground observation at Kanazawa University during the graupel-dominant period (Period G1: 1305 to 1312 JST). The solid squares in (a), (b), (c), and (d) indicate the location of Kanazawa University. Color shadings in (a)–(d) represent the Z_h , Z_{dr} , K_{dp} , and ρ_{hv} values. Black triangles, circles, cross marks, and dots represent the results of HC: DG, DS, IC, and the others, respectively. The ranges of graupel and snow reachable areas described in Fig. 4 are shown as sectors.

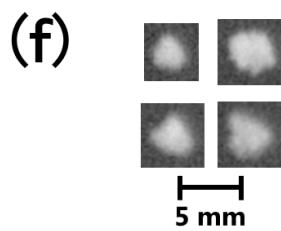
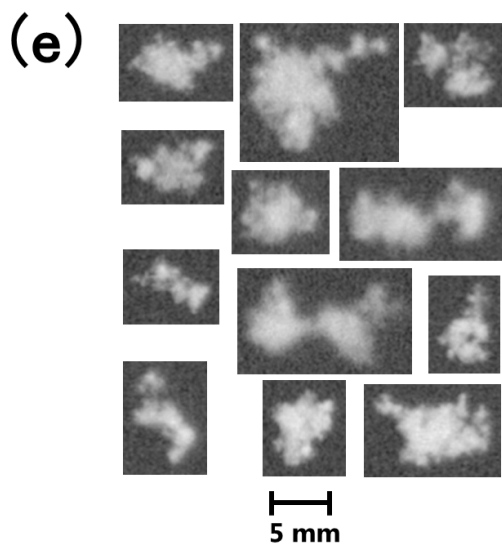
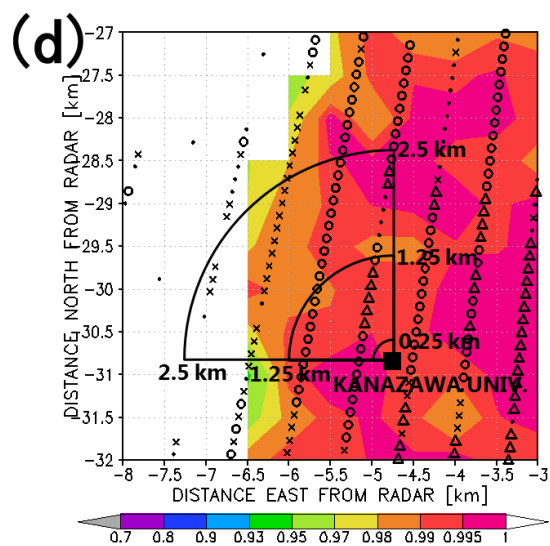
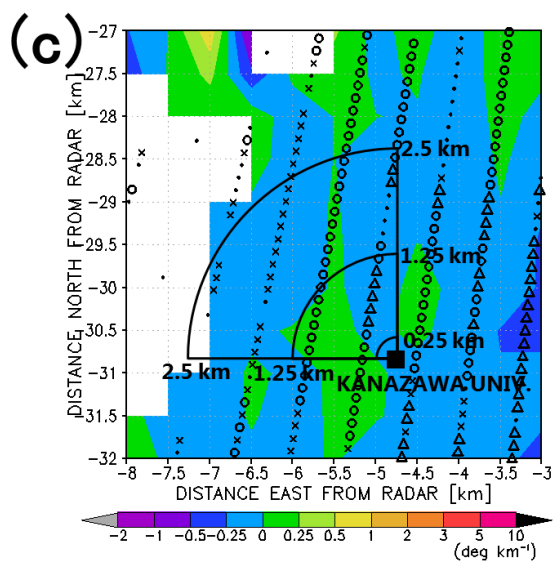
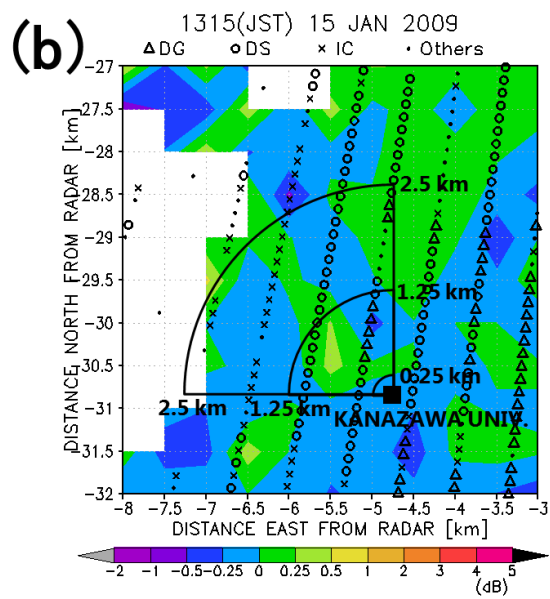
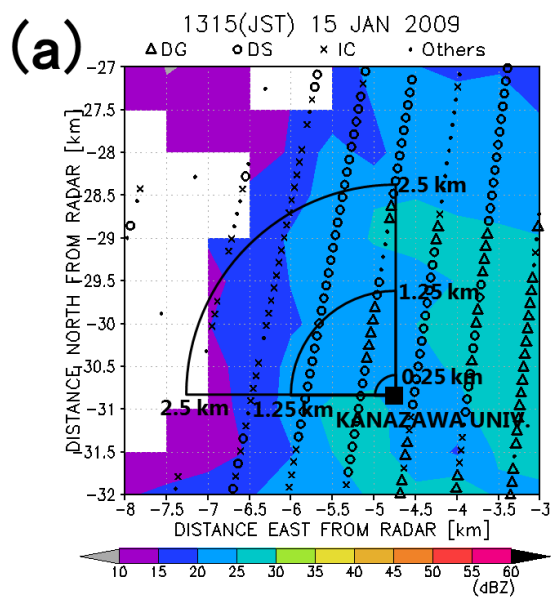


Fig. 7. Same as Fig. 6 but at 1315 JST 15 January 2009 for (a), (b), (c), and (d), and examples of images of (e) snow and (f) graupel particles obtained by ground observation during the snow-dominant period (Period S1: 1315 to 1322 JST).

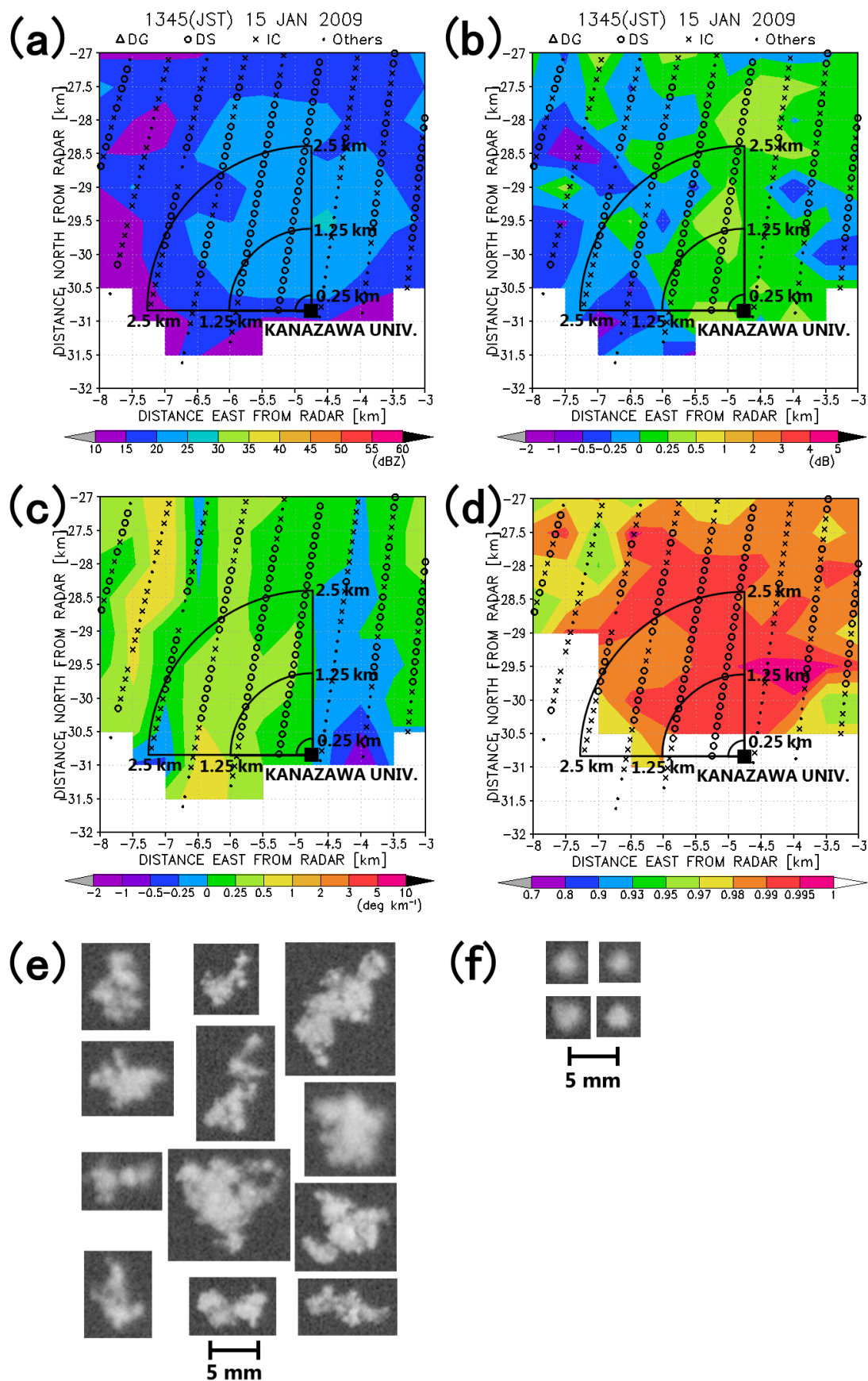


Fig. 8. Same as Fig. 7 but at 1345 JST 15 January 2009 for (a), (b), (c), and (d), and (e) and (f) examples of hydrometeor images during the snow-dominant period (Period S2: 1347 to 1355 JST).

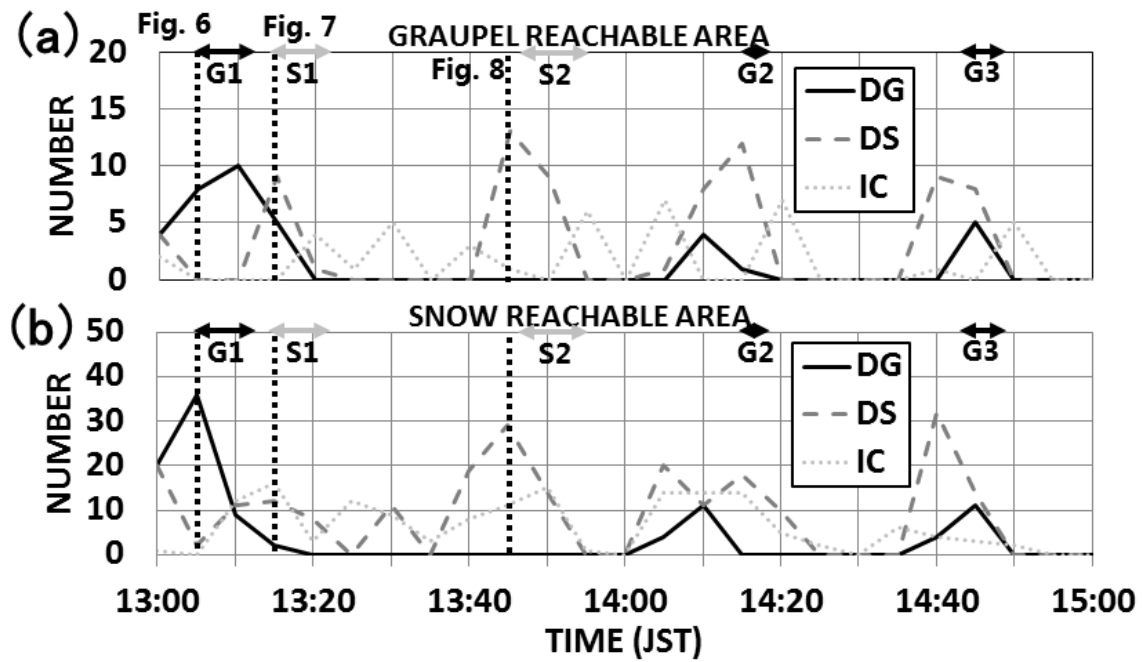


Fig. 9. Time series of numbers of radar sampling volumes for each hydrometeor type in (a) graupel and (b) snow reachable areas from 1300 to 1500 JST 15 January 2009, the same period as Fig. 5. The solid and dashed lines represent numbers of radar sampling volumes identified by HC as DG and DS, respectively. The number of radar sampling volumes identified as IC is also shown by the dotted line, as a reference. Horizontal black and gray arrows indicate periods when graupel (Periods G1, G2 and G3) and snow (Periods S1 and S2), respectively, were dominant at Kanazawa University, as Fig. 5. Vertical dotted lines indicate times of PPI scans shown in Figs. 6, 7, and 8.

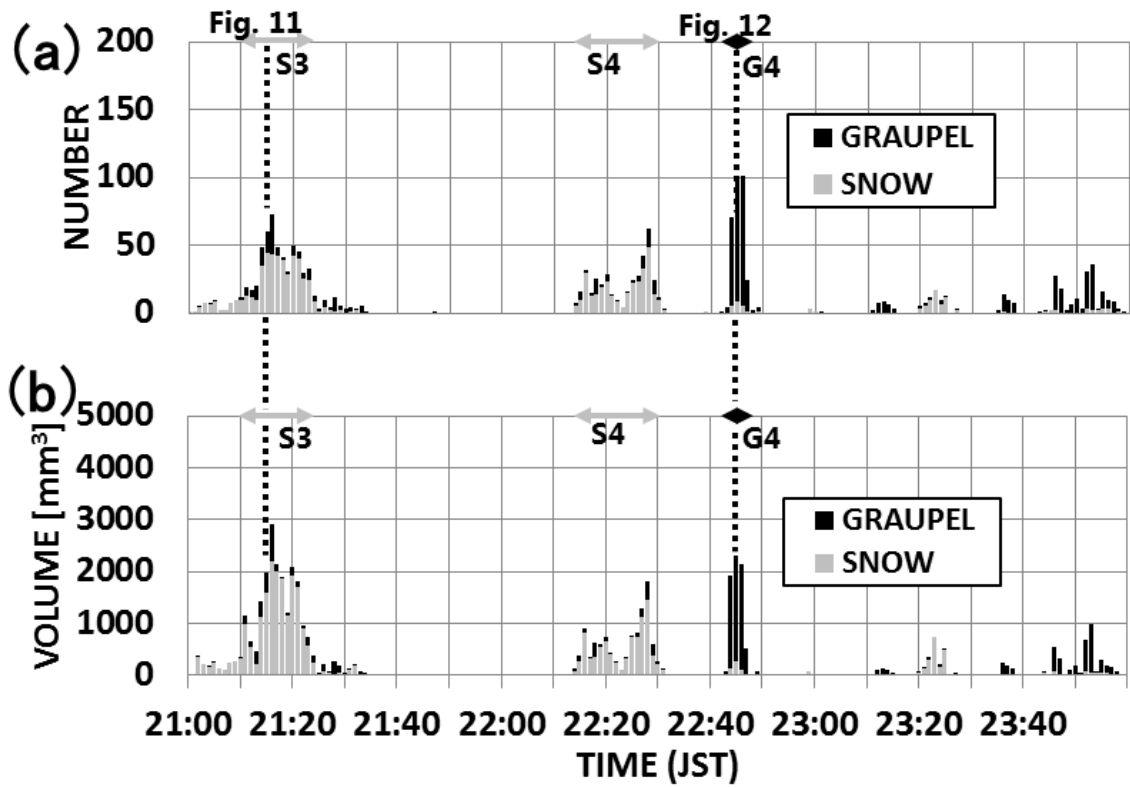


Fig. 10. Same as Fig. 5 but from 2100 to 2359 JST 16 February 2009. Horizontal black and gray arrows indicate periods when graupel (Periods G4) and snow (Periods S3 and S4) were dominant, respectively. Vertical dotted lines indicate times of PPI scans shown in Figs. 11 and 12.

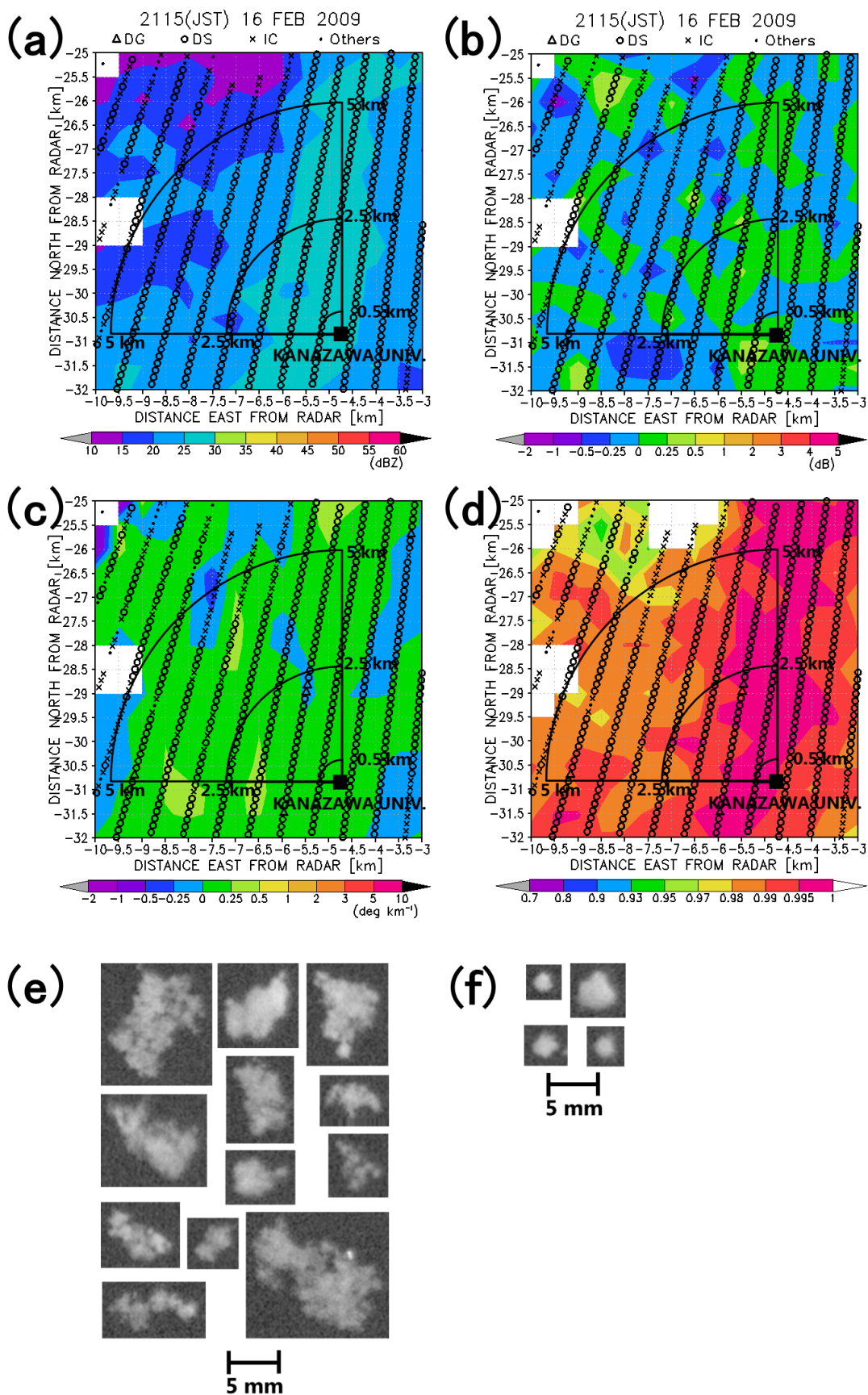


Fig. 11. Same as Fig. 7 but at 2115 JST 16 February 2009 for (a), (b), (c), and (d), and examples of images of (e) snow and (f) graupel particles obtained by ground observation during the snow-dominant period (2115 to 2119 JST during Period S3). The ranges of the graupel and snow reachable areas were calculated in the same way as in Fig. 4 but the wind speed was $\sim 10 \text{ m s}^{-1}$.

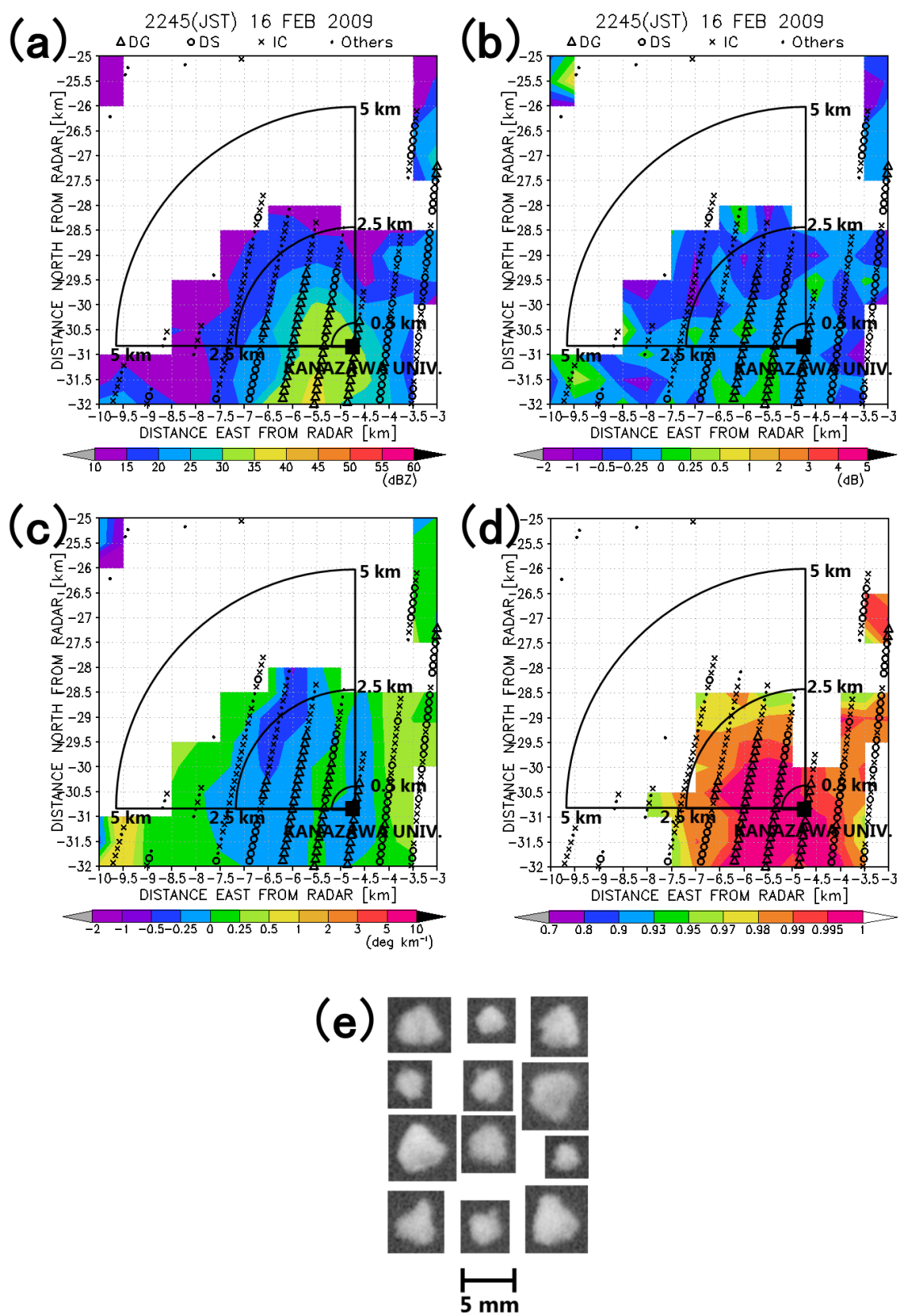


Fig. 12. Same as Fig. 6 but at 2245 JST 16 February 2009 for (a), (b), (c), and (d), and

(e) examples of graupel particles obtained by ground observation during the graupel-dominant period (2245 to 2249 JST during Period G4). The ranges of the graupel and snow reachable areas were calculated in the same way as in Fig. 4 but the wind speed was $\sim 10 \text{ m s}^{-1}$.

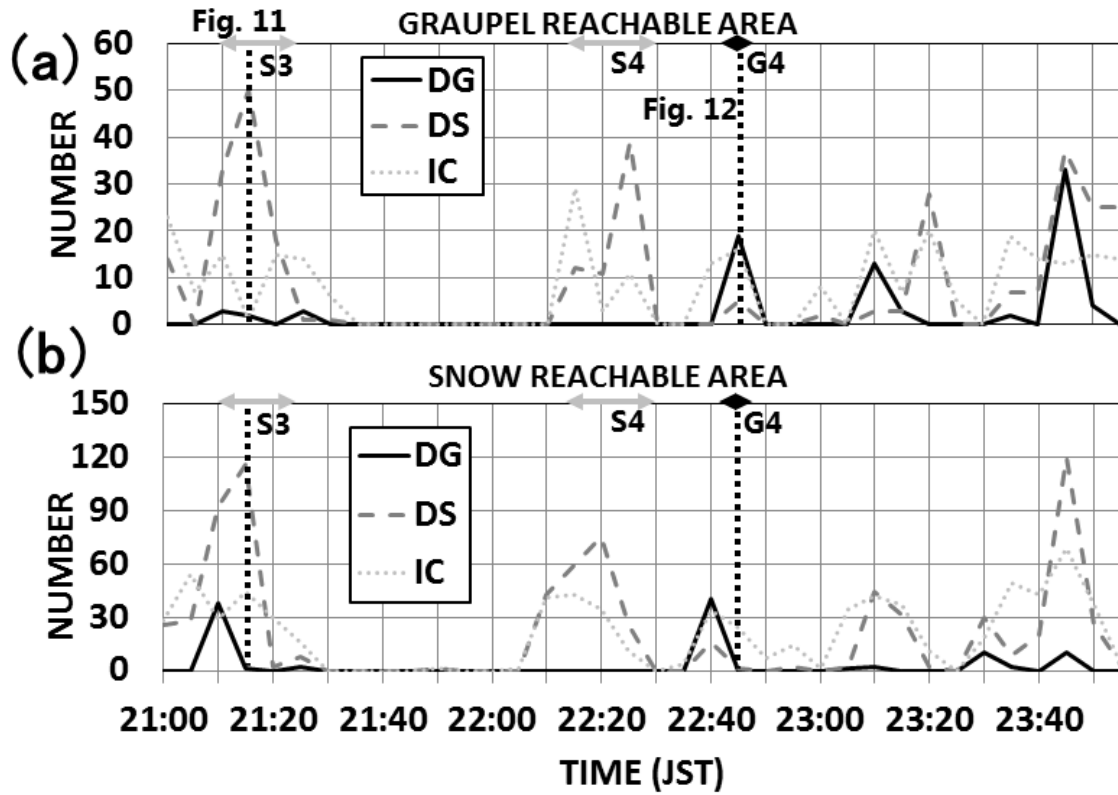


Fig. 13. Same as Fig. 9 but from 2100 to 2355 JST 16 February 2009, the same period as Fig. 10. The ranges of the graupel and snow reachable areas were calculated in the same way as in Fig. 4 but the wind speed was $\sim 10 \text{ m s}^{-1}$. Horizontal black and gray arrows indicate periods when graupel (Periods G4) and snow (Periods S3 and S4) were dominant, respectively, as Fig. 10. Vertical dotted lines indicate times of PPI scans shown in Figs. 11 and 12.

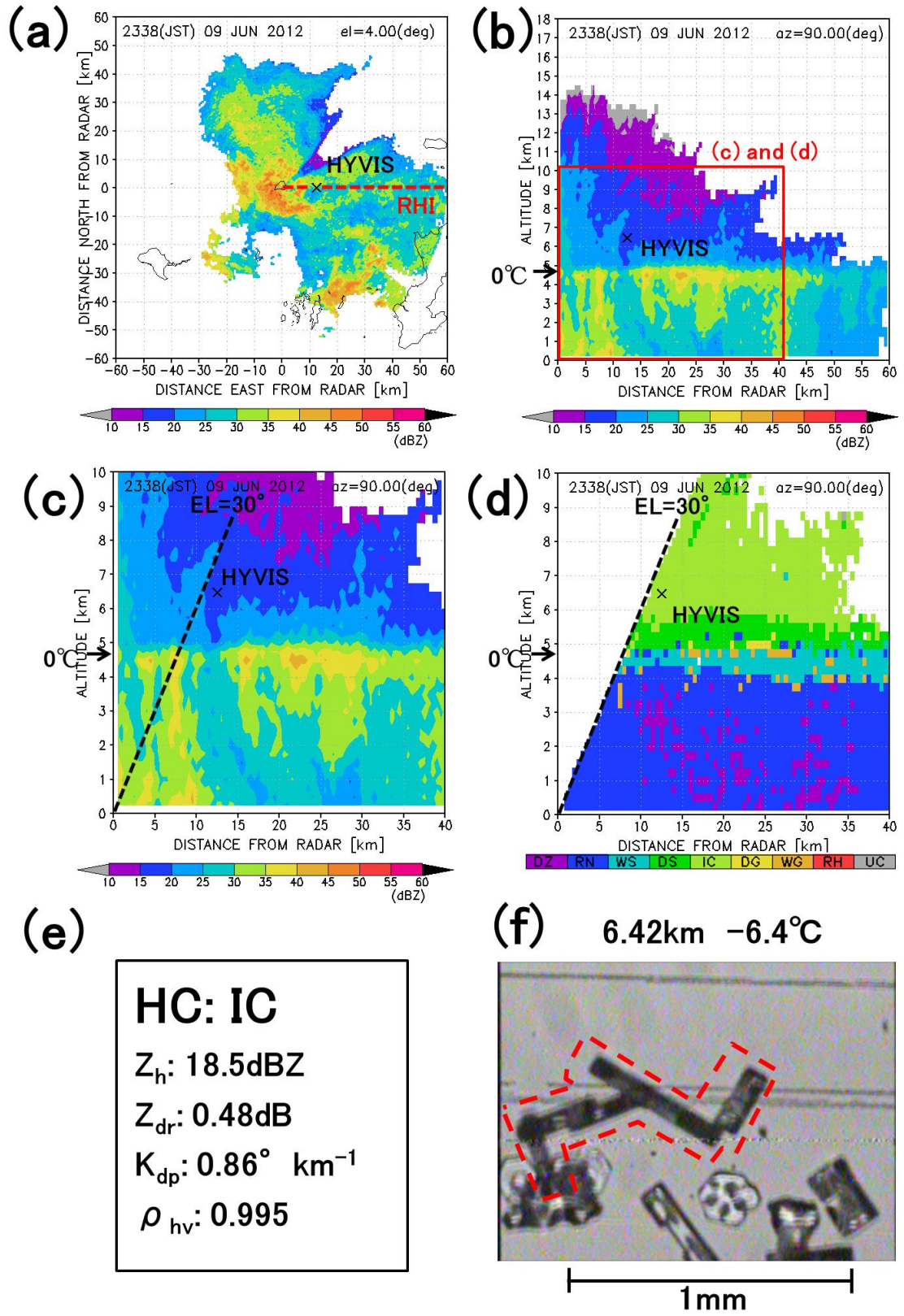


Fig. 14. Z_h in (a) PPI at elevation 4° and (b) RHI in the direction of the HYVIS, (c) and

(d) Z_h and HC result in RHI for the near range, (e) the result of HC obtained from averaged radar variables over a $1 \text{ km} \times 1 \text{ km} \times 0.2 \text{ km}$ volume centered on the HYVIS and (f) a sample HYVIS image of the dominant hydrometeor type observed at 2338 JST 9 June 2012 (HYVIS #3). The PPI and RHI images in (a), (b), (c), and (d) are depicted in $0.5 \text{ km} \times 0.5 \text{ km}$ resolutions. The red square frame in (b) indicates the range of (c) and (d). Note that the region where the elevation angle is greater than 30° is masked for the result of HC in (d) to avoid the effect of high elevation angle for differential variables (Z_{dr} and K_{dp}), as mentioned in Section 3. The red-dashed line in (f) indicates the representative hydrometeor obtained from the HYVIS image (snow aggregates composed of column particles).

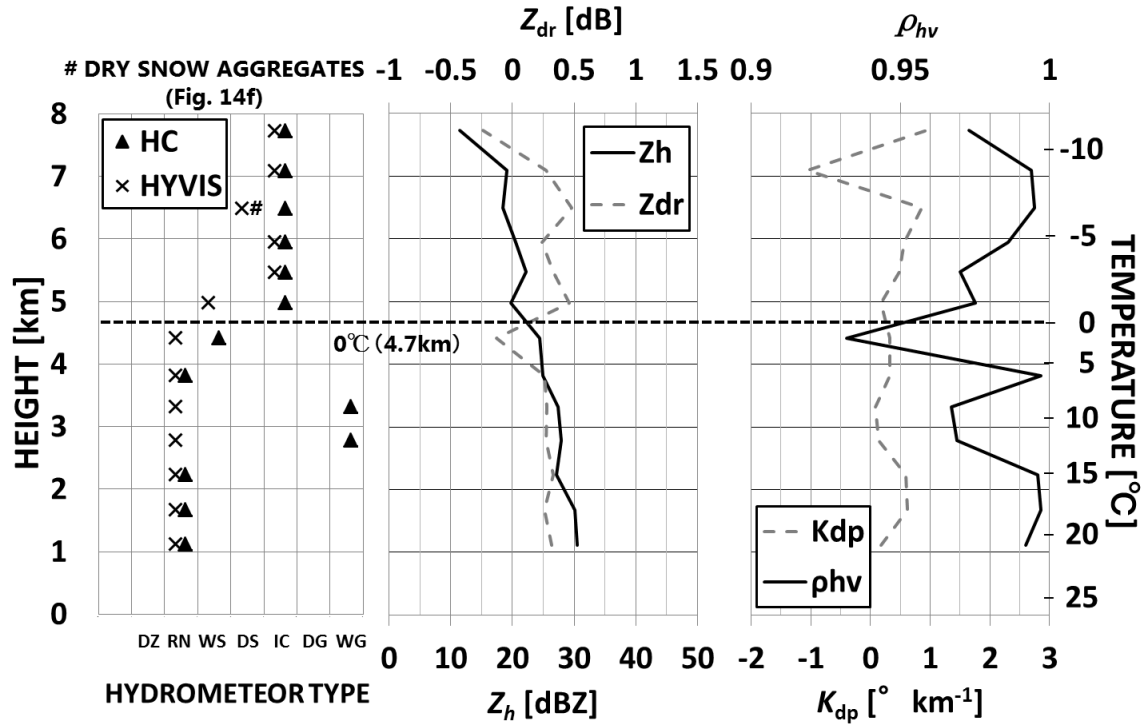


Fig. 15. Results of the comparison between HC and HYVIS #3 observations (left), and vertical profiles of Z_h , Z_{dr} (center), and K_{dp} , and ρ_{hv} (right) on 9 June 2012. The solid and dashed lines represent (center panel) Z_h and Z_{dr} , and (right panel) represent ρ_{hv} , and K_{dp} , respectively. Temperature observed by HYVIS is also presented in the vertical axis of the right panel. The image of hydrometeors observed with HYVIS at the point indicated by the # is shown in Fig. 14f.

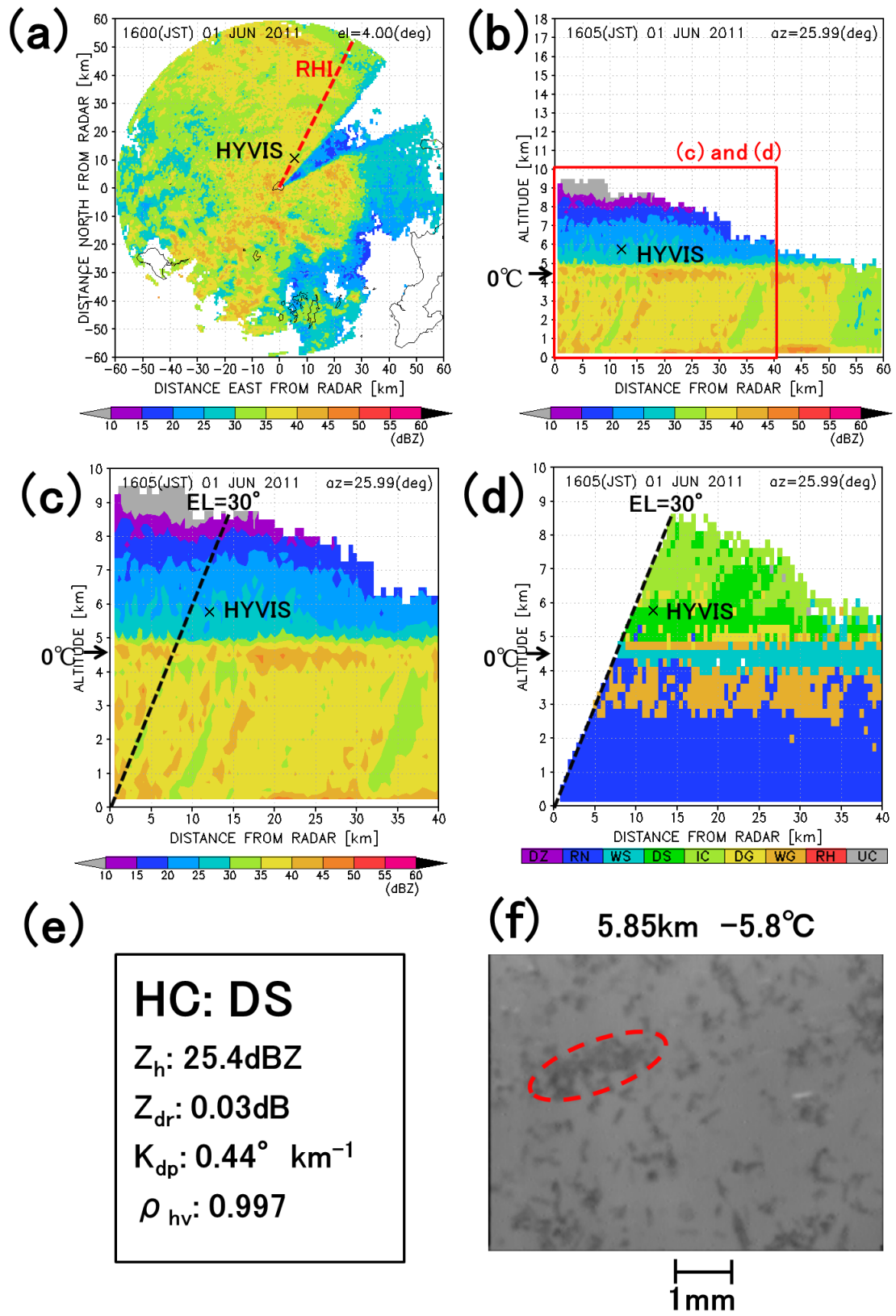


Fig. 16. Same as Fig. 14 but at 1605 JST 1 June 2011 (HYVIS #1). The red-dashed line

in (f) indicates the representative hydrometeor obtained from the HYVIS image (snow aggregates).

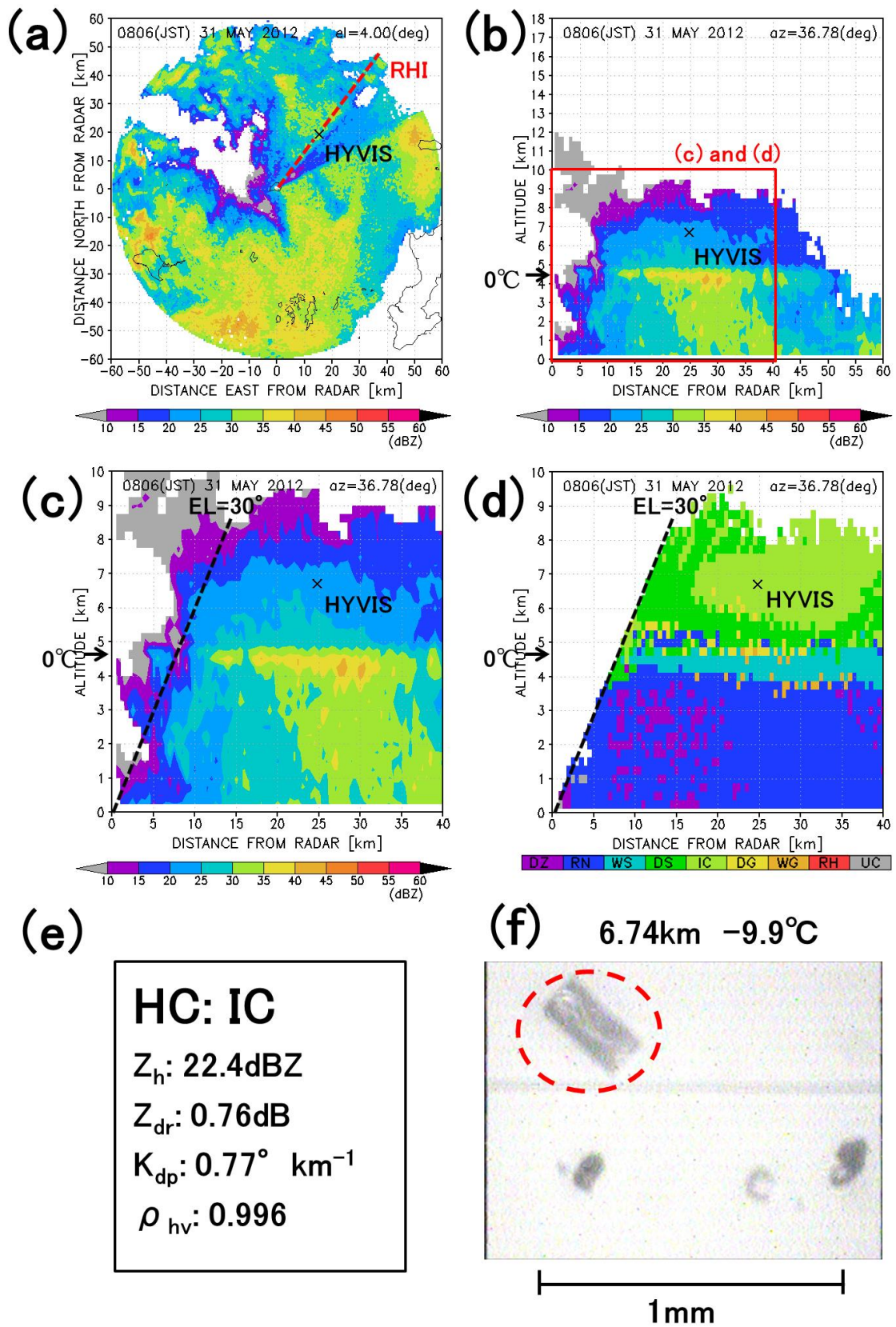


Fig. 17. Same as Fig. 14 but at 0806 JST 31 May 2012 (HYVIS #2). The red-dashed line in (f) indicates the representative hydrometeor obtained from the HYVIS image (non-aggregated column particle).

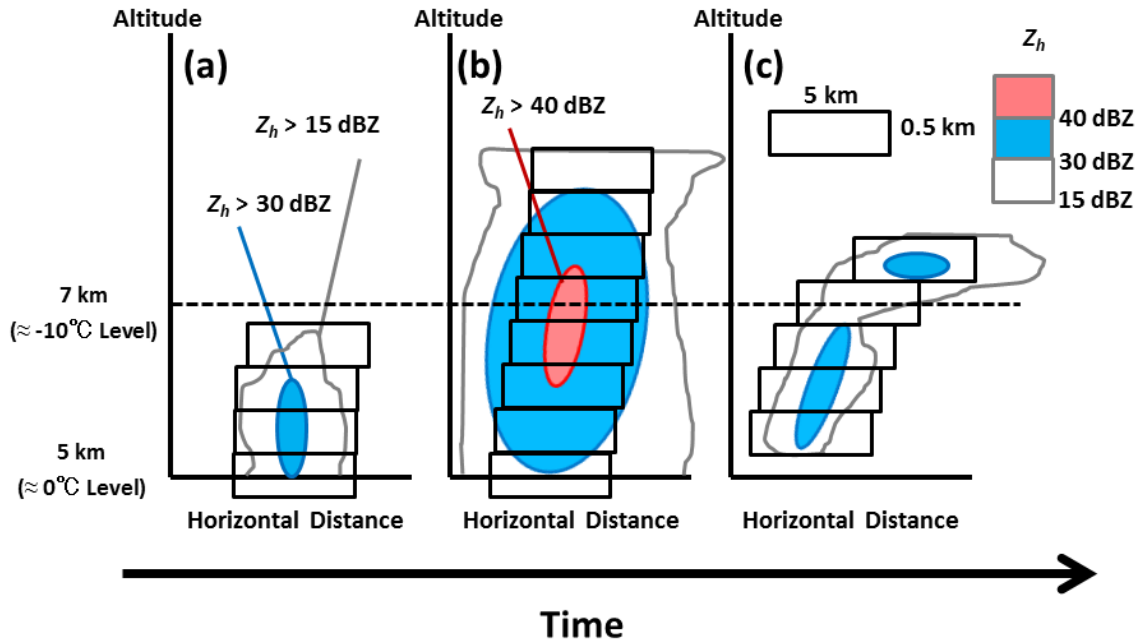


Fig. 18. Schematic illustration showing method for detecting and tracking reflectivity cores. The reflectivity core is first delineated as the 5×5 km horizontal area centered on a local maximum reflectivity greater than 40 dBZ at 7 km (just above the -10°C level) in (b). The reflectivity core is then defined as solid above the 0°C level with a horizontal area (5×5 km) centered on a local maximum at each height; vertical continuity is assessed by visual analysis. The reflectivity core is tracked forwards (c) and backwards (a) in time until maximum reflectivity above the 0°C level falls below 30 dBZ.

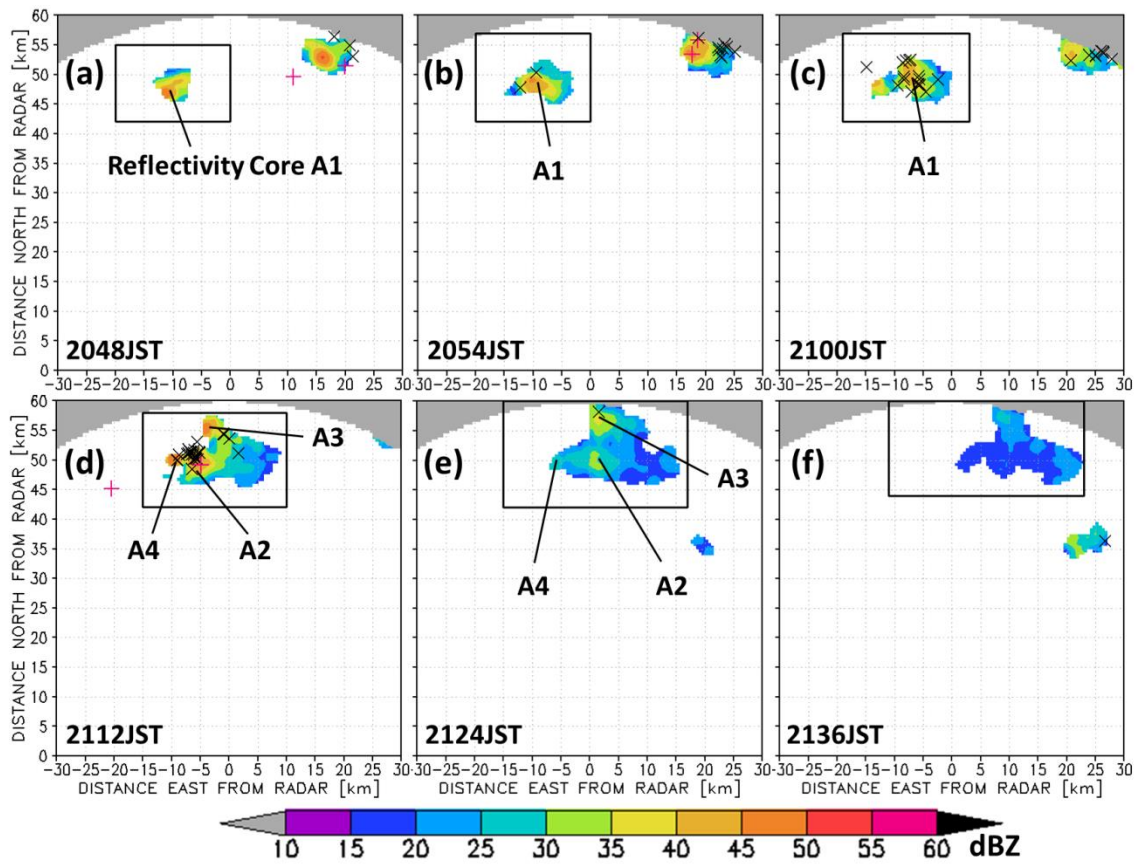


Fig. 19. Time series of radar reflectivity at 7 km at: (a) 2048 JST, (b) 2054 JST, (c) 2100 JST, (d) 2112 JST, (e) 2124 JST, and (f) 2136 JST on 26 July 2010. The target thundercloud for analysis (A) is encompassed by the black frame, which also indicates the area in which CG numbers were counted. The black “x” and pink “+” symbols represent locations of negative and positive CG strikes, respectively. See text of Section 5.2 and Fig. 18 for details on the detection and tracking of the reflectivity core.

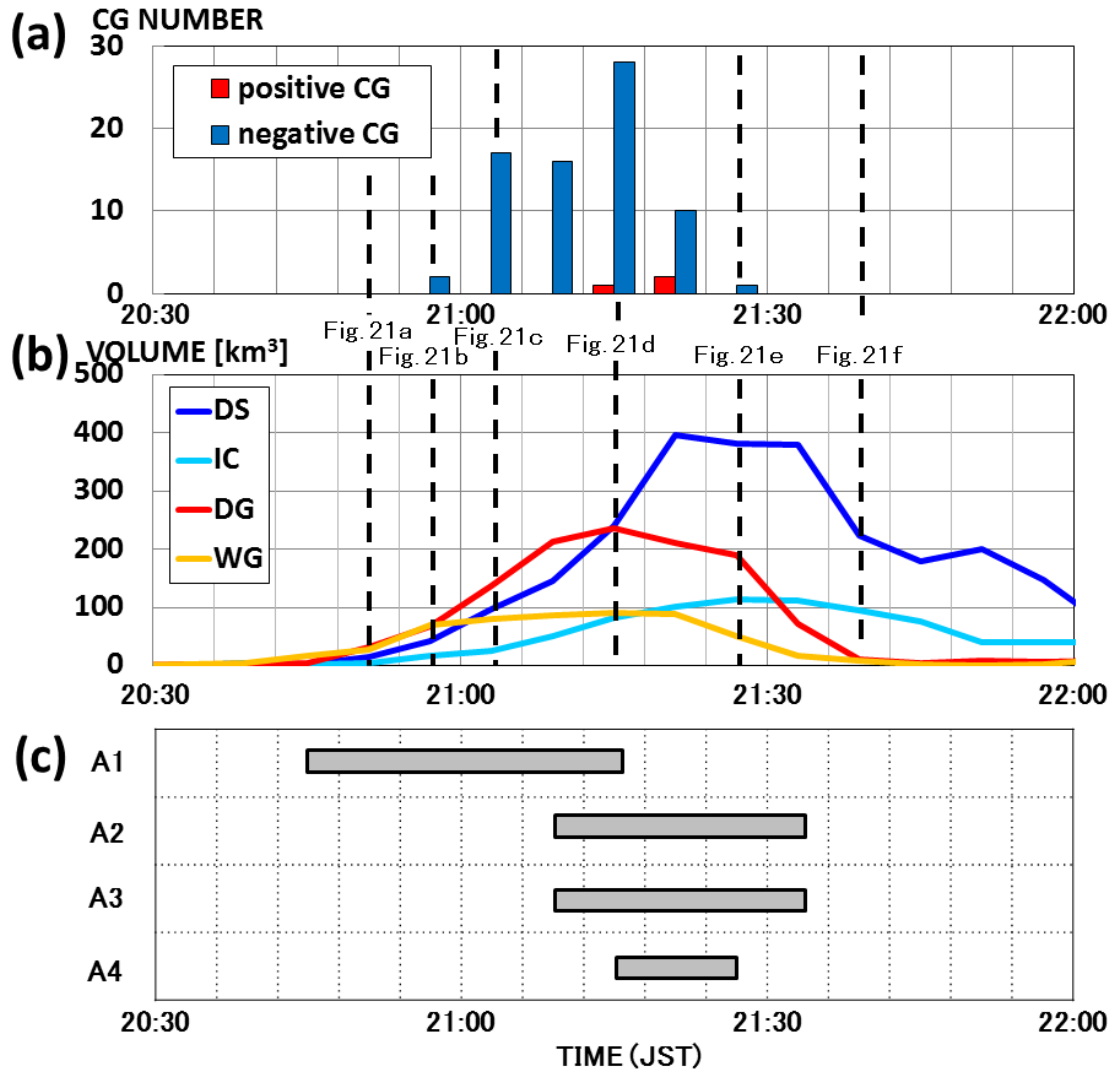


Fig. 20. Time series of: (a) 6-minute accumulated positive and negative CG strike numbers, (b) volume of DS, IC, DG, and WG above the 0°C level, and (c) duration of reflectivity cores in Thundercloud A from 2030 to 2200 JST on 26 July 2010. Vertical dashed lines indicate vertical distributions shown in Fig. 21.

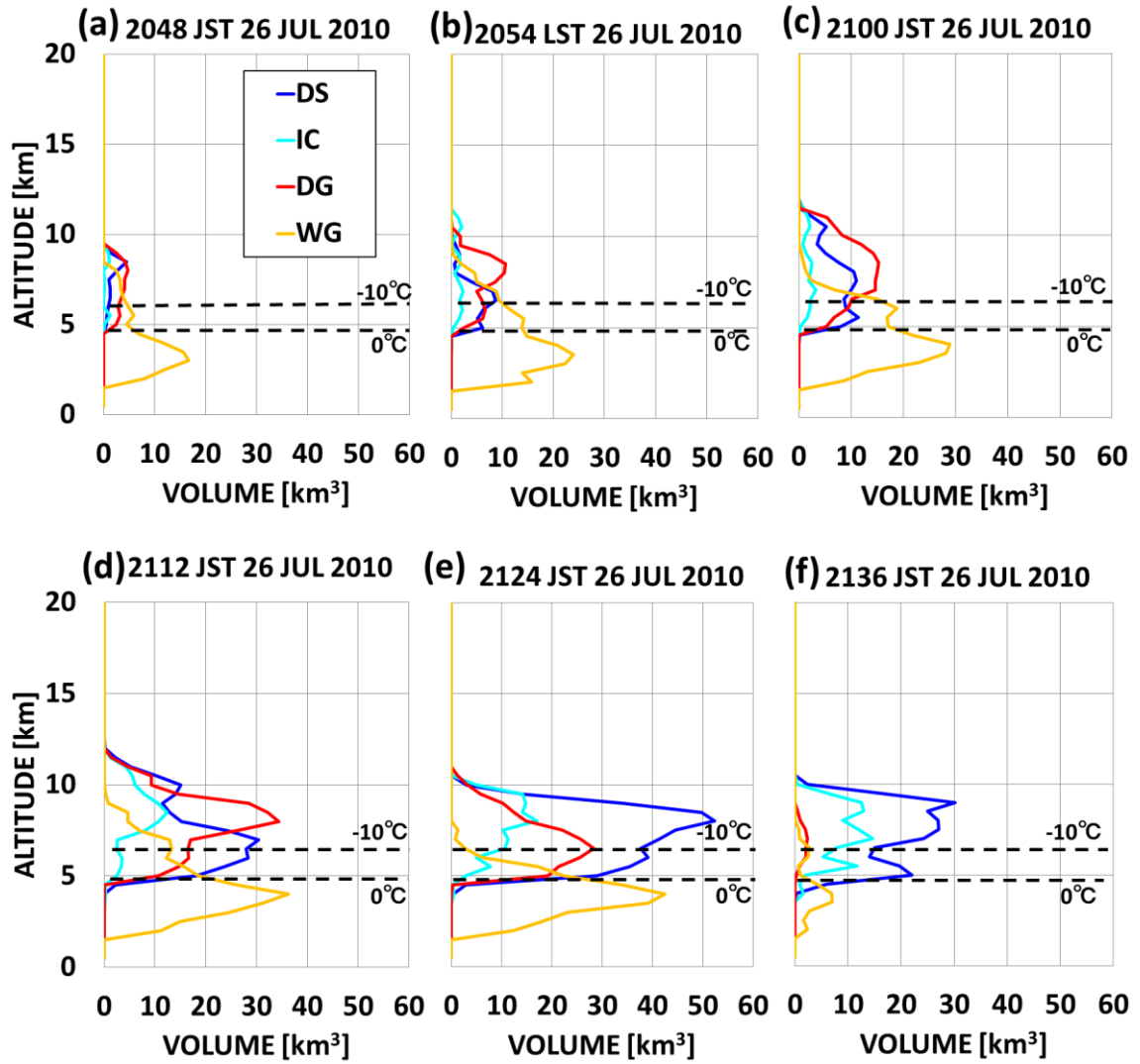


Fig. 21. Time series of vertical distribution of DS, IC, DG, and WG volumes in Thundercloud A at: (a) 2048 JST, (b) 2054 JST, (c) 2100 JST, (d) 2112 JST, (e) 2124 JST, and (f) 2136 JST on 26 July 2010.

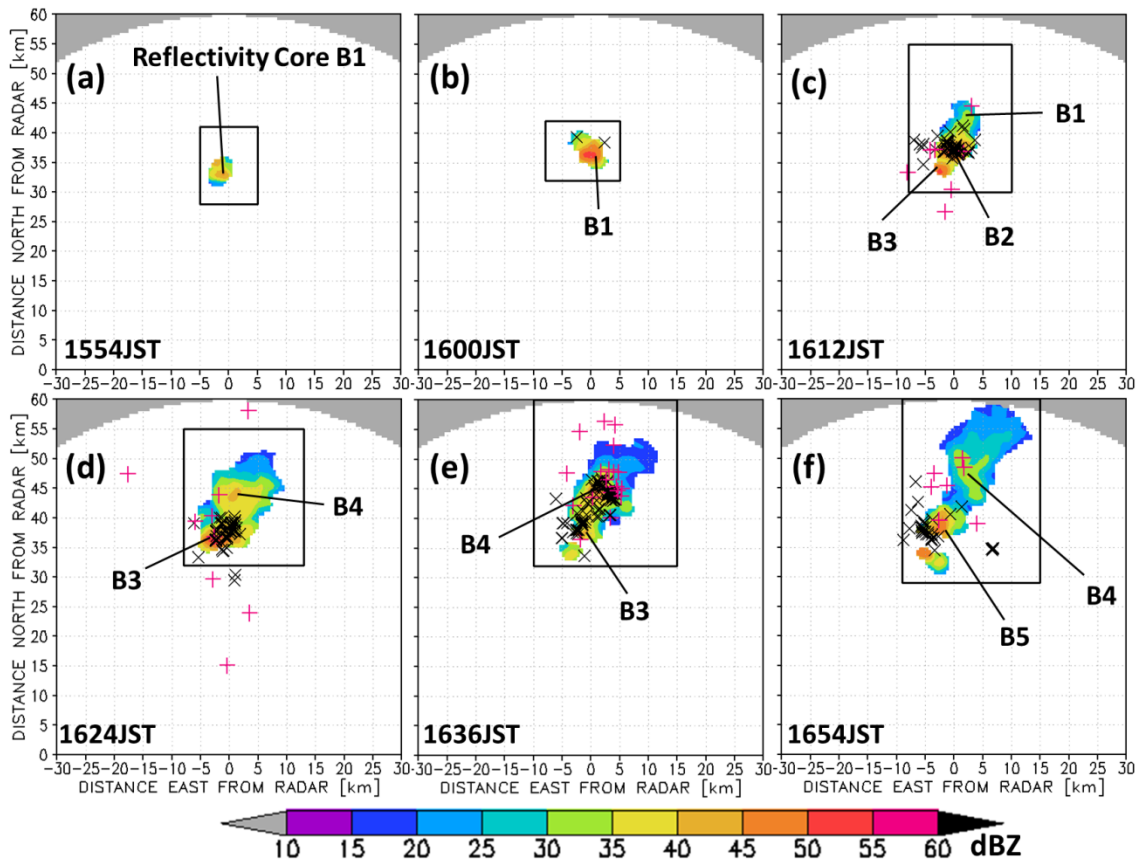


Fig. 22. Same as Fig. 19, but for thundercloud B at: (a) 1554 JST, (b) 1600 JST, (c) 1612 JST, (d) 1624 JST, (e) 1636 JST, and (f) 1654 JST on 25 August 2010.

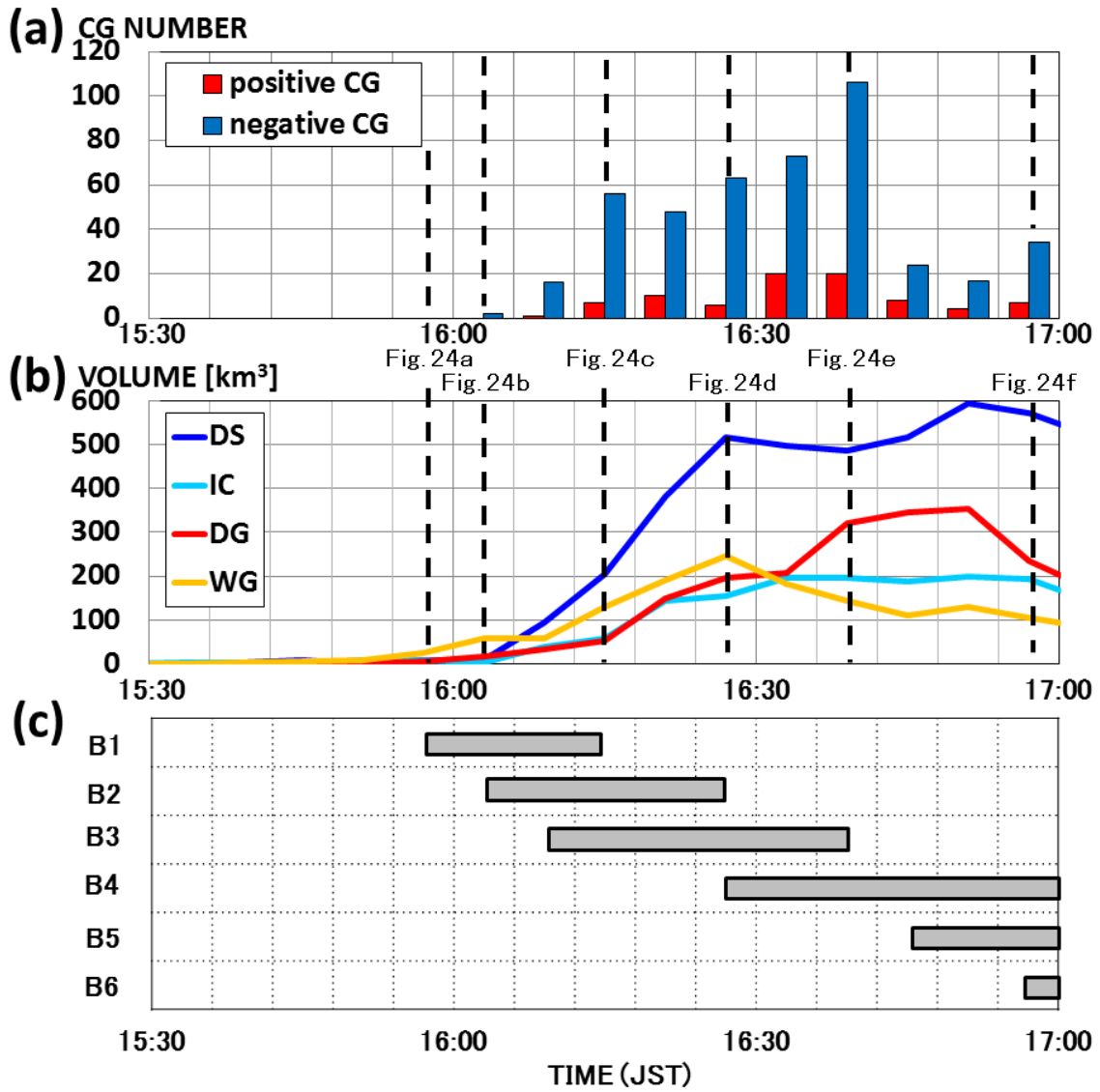


Fig. 23. Same as Fig. 20, but for Thundercloud B from 1530 to 1700 JST on 25 August 2010. Vertical dashed lines indicate the times of the vertical distributions shown in Fig. 24.

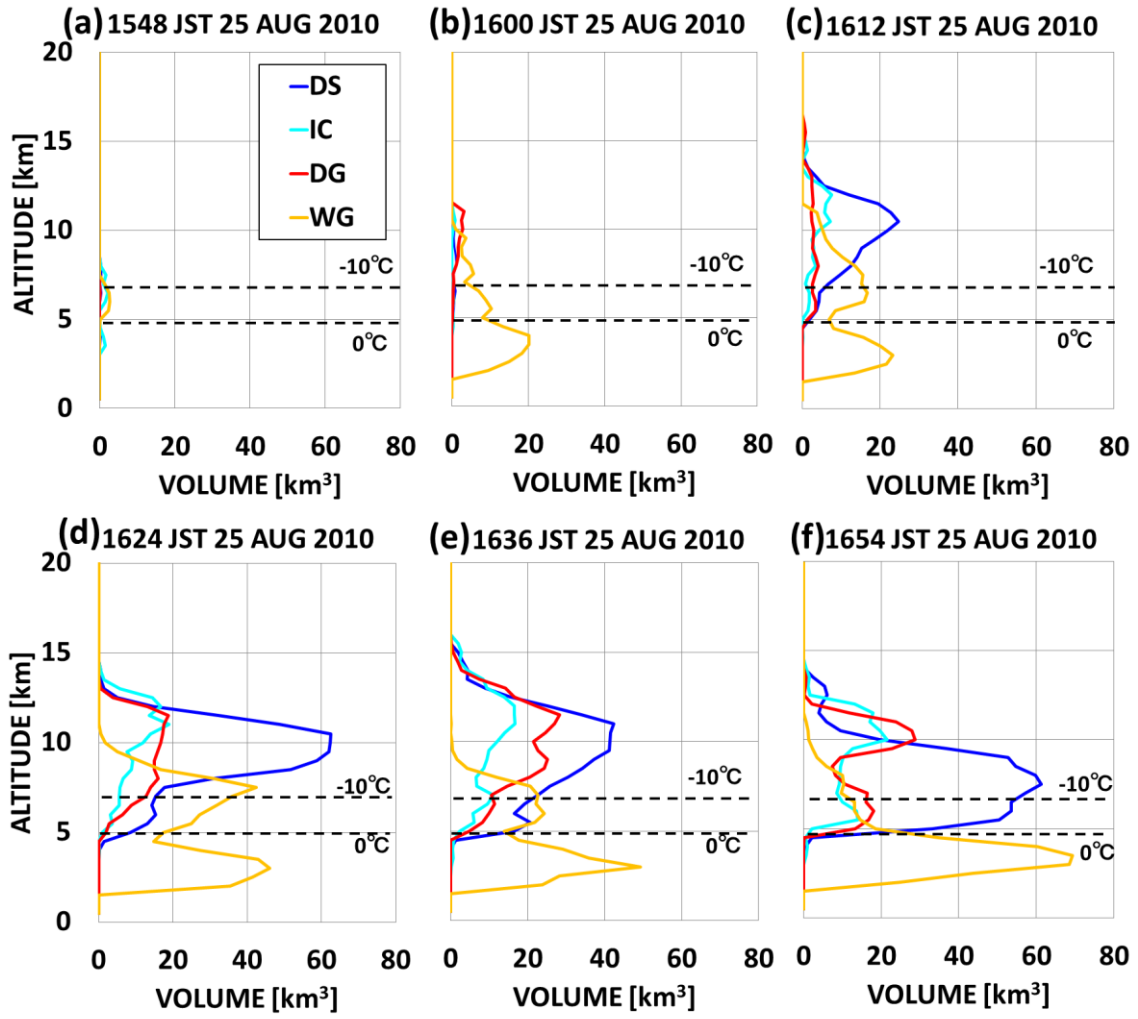


Fig. 24. Same as Fig. 21, but for Thundercloud B at: (a) 1554 JST, (b) 1600 JST, (c) 1612 JST, (d) 1624 JST, (e) 1636 JST, and (f) 1654 JST on 25 August 2010.

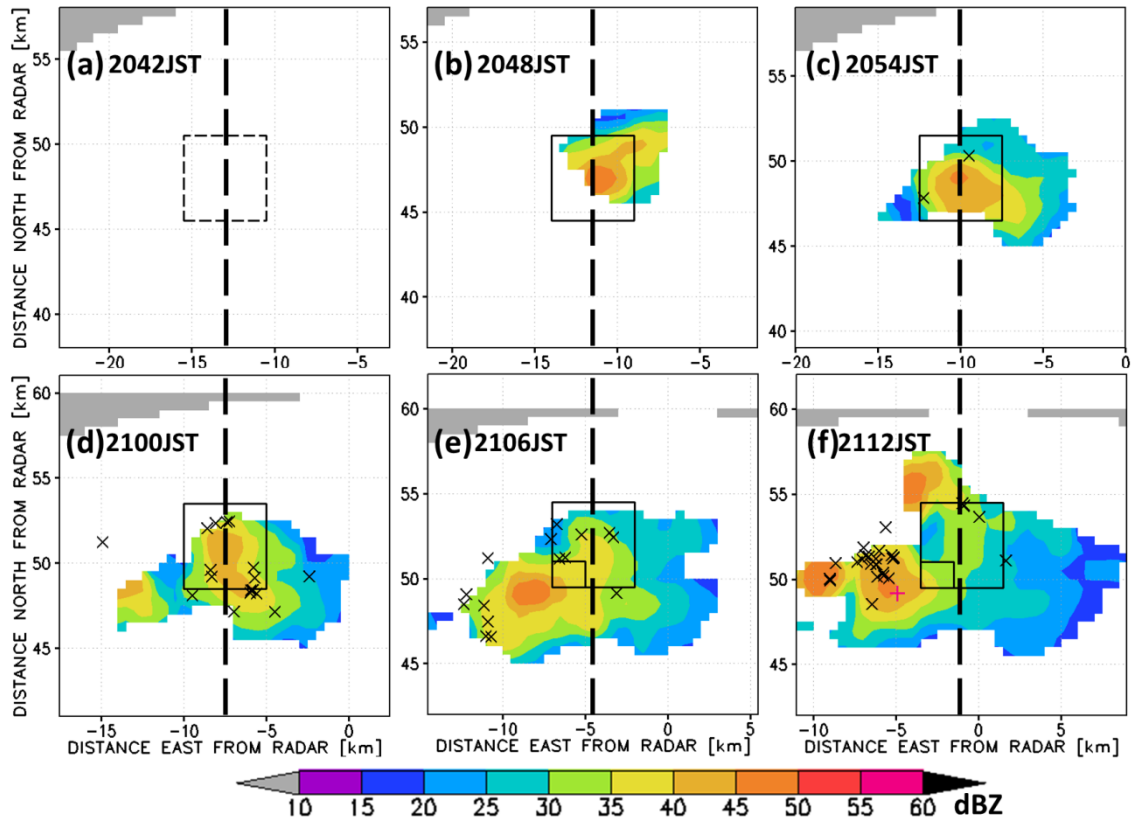


Fig. 25. Enlarged image of the time series of radar reflectivity at 7 km for reflectivity core A1 every 6 minutes from 2042 to 2112 JST on 26 July 2010. Reflectivity core A1 is shown by black solid squares at each time except for 2042 JST, when it is indicated by a black dashed square (reflectivity core A1 did not reach 7 km in height at this point). Smaller rectangles mark areas were excluded from the analysis to avoid contamination from other reflectivity cores. Black “x” and pink “+” symbols represent locations of negative and positive CG strikes, respectively. Vertical black dashed lines show the positions of vertical cross-sections in Fig. 27.

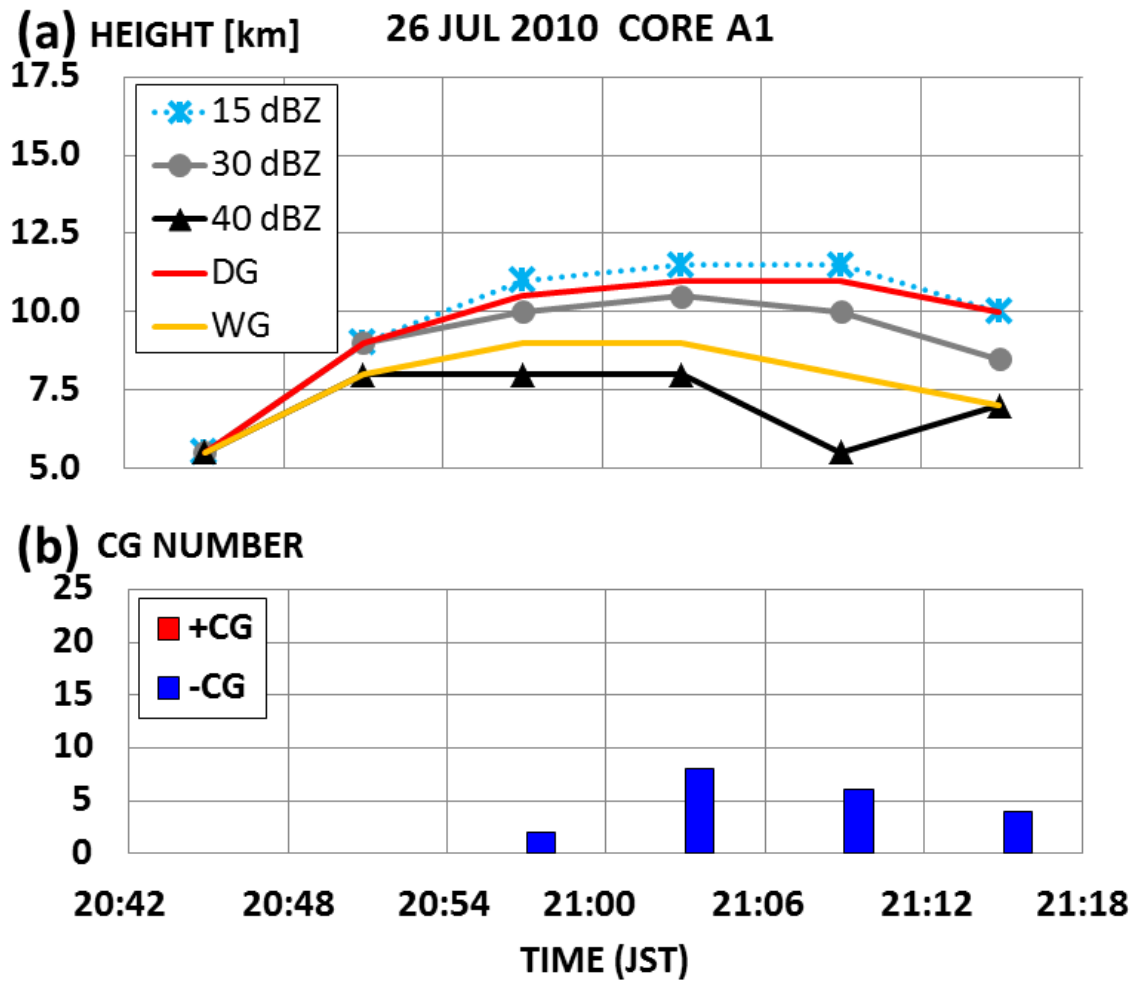


Fig. 26. Time series of: (a) the echo top heights at 15, 30, and 40 dBZ, maximum DG and WG volume heights, and (b) the numbers of positive and negative CG strikes for reflectivity core A1 from 2042 to 2112 JST on 26 July 2010.

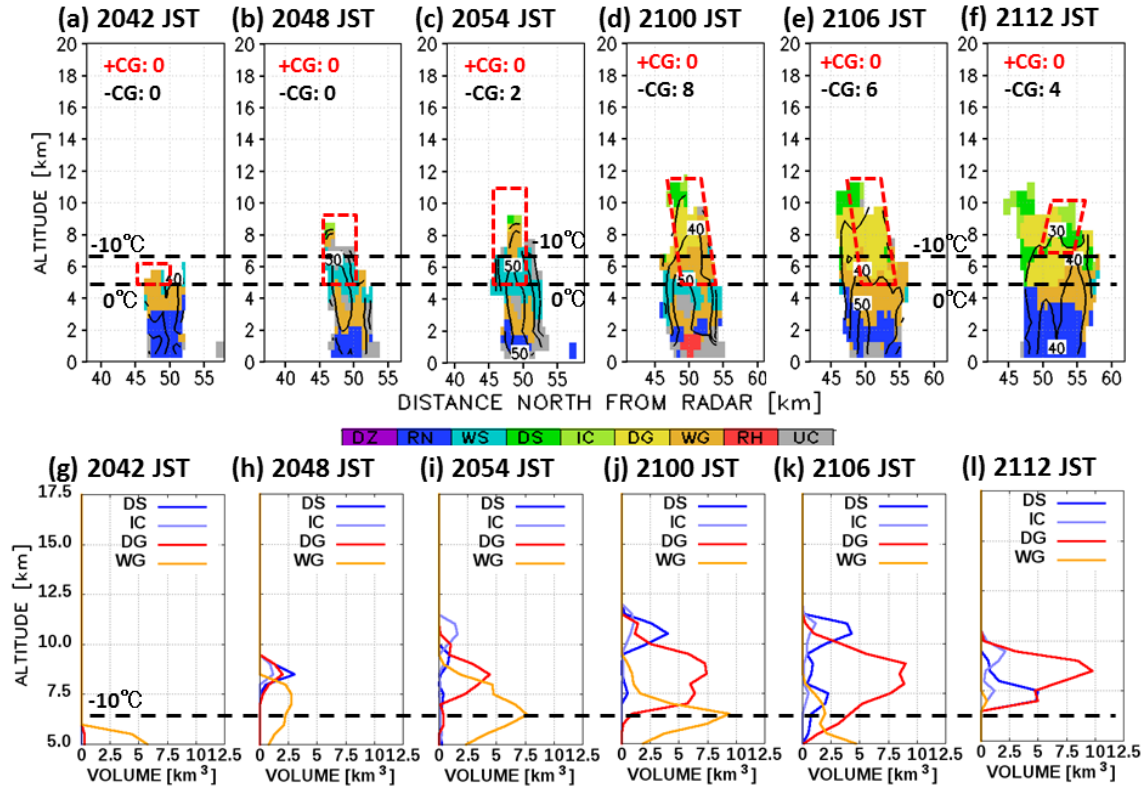


Fig. 27. Top: Time series of HC cross sections in a north–south direction along the center line of reflectivity core A1 (denoted in Fig. 25). Bottom: Vertical distributions of DS, IC, DG, and WG volumes above the 0°C level (4.9 km in height) for reflectivity core A1 every 6 minutes from 2042 to 2112 JST on 26 July 2010. Red dashed boxes in upper panels indicate the cross section of reflectivity core A1. Horizontal black dashed lines in each panel indicate the 0°C and –10°C levels. The 30, 40, and 50 dBZ radar reflectivity contours are overlaid on the HC results in (a)–(f). The numbers of positive and negative CG strikes counted in reflectivity core A1 are also indicated in (a)–(f).

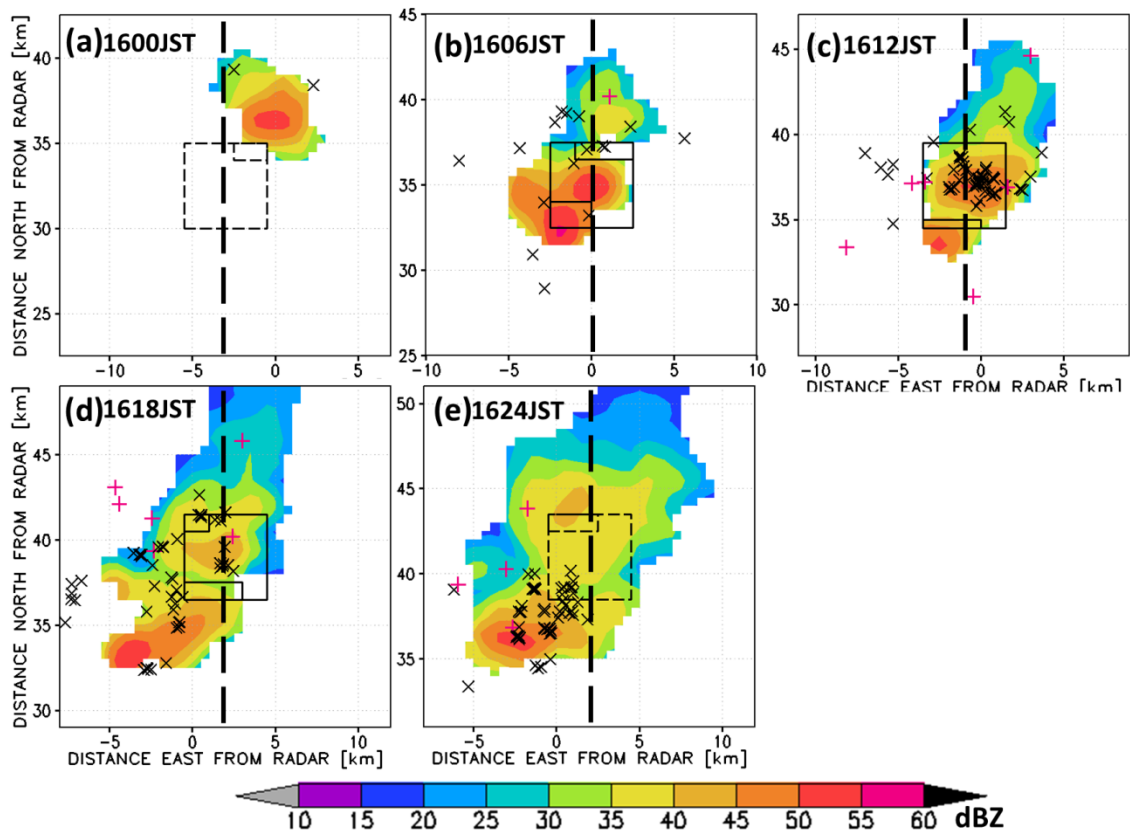


Fig. 28. Same as Figure 25, but for reflectivity core B2 every 6 minutes from 1600 to 1624 JST on 25 August 2010. Vertical black dashed lines show the positions of vertical cross-sections in Figure 30.

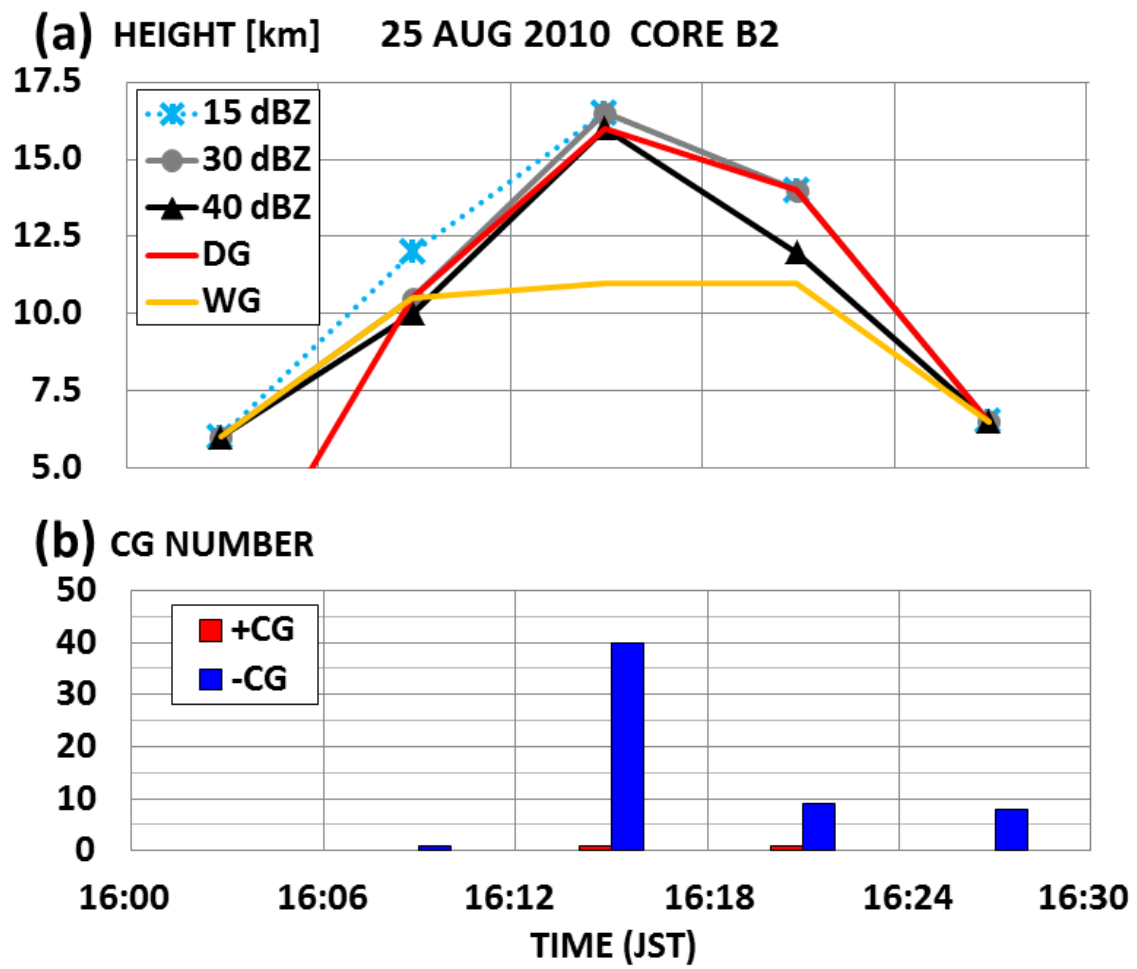


Fig. 29. As Fig. 26, but for reflectivity core B2 from 1600 to 1624 JST on 25 August 2010.

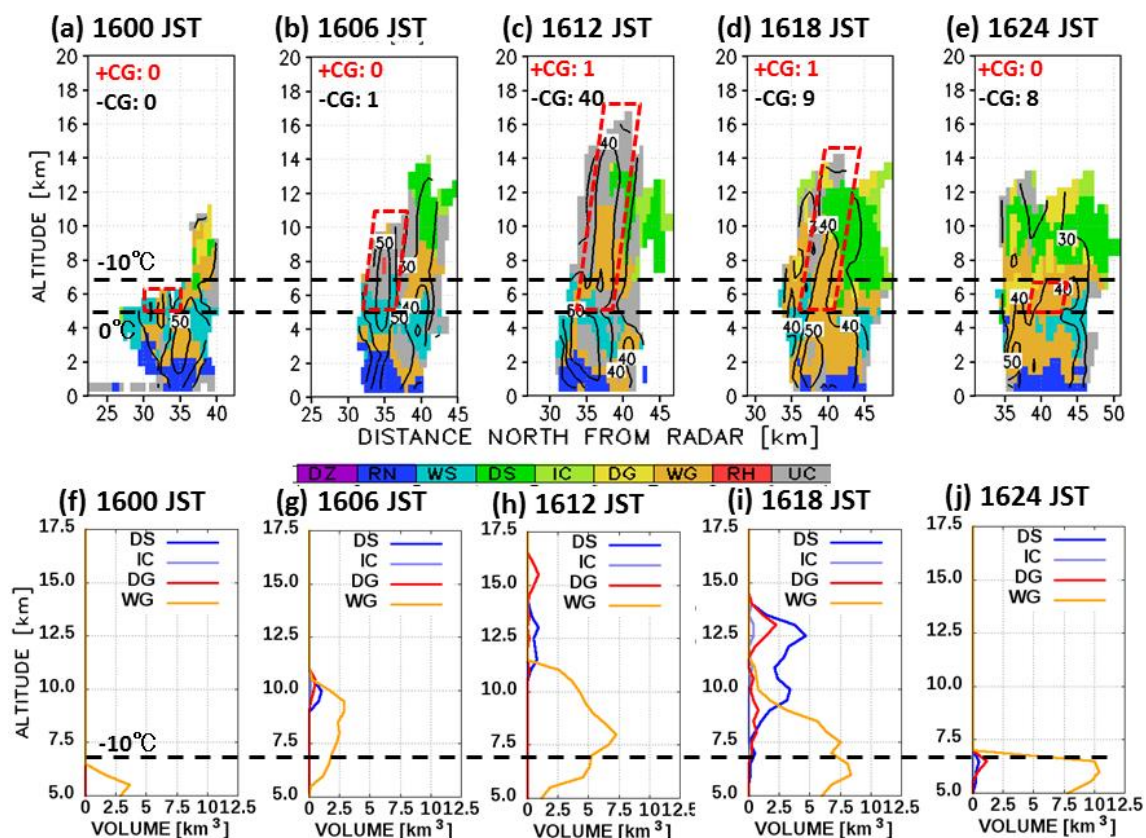


Fig. 30. Same as Fig. 27, but for reflectivity core B2 every 6 minutes from 1600 to 1624

JST on 25 August 2010.

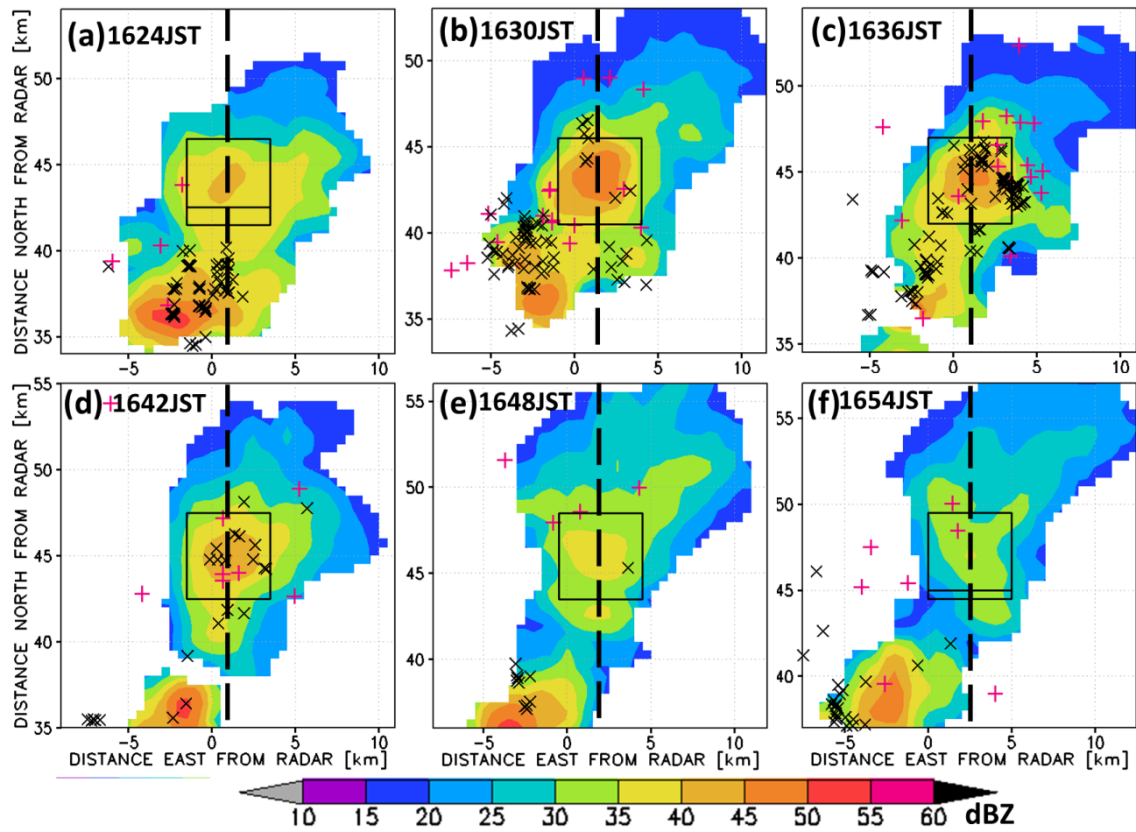


Fig. 31. Same as Fig. 25, but for reflectivity core B4 every 6 minutes from 1624 to 1654 JST on 25 August 2010. Vertical black dashed lines show the positions of vertical cross-sections in Fig. 33.

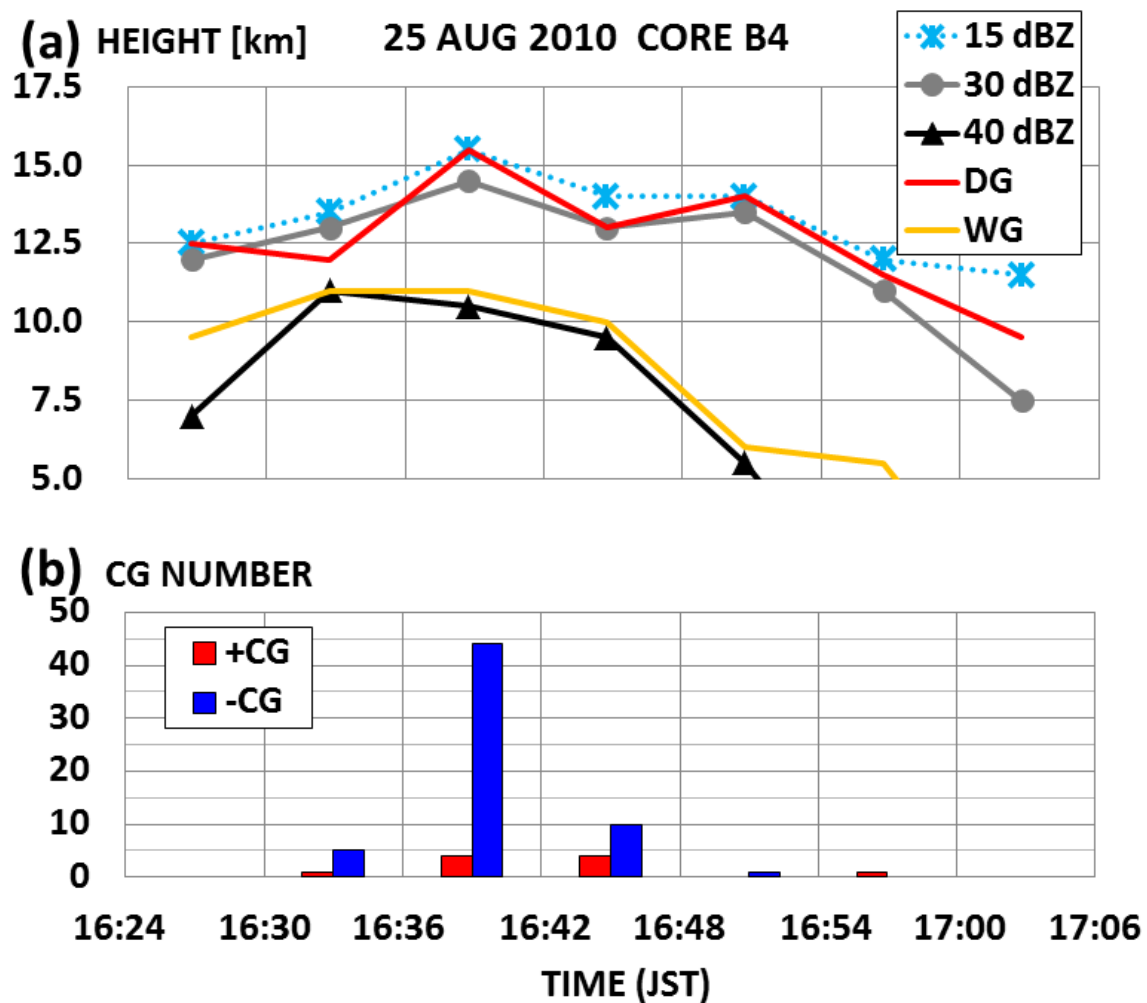


Fig. 32. Same as Fig. 26, but for reflectivity core B4 from 1624 to 1700 JST on 25 August 2010.

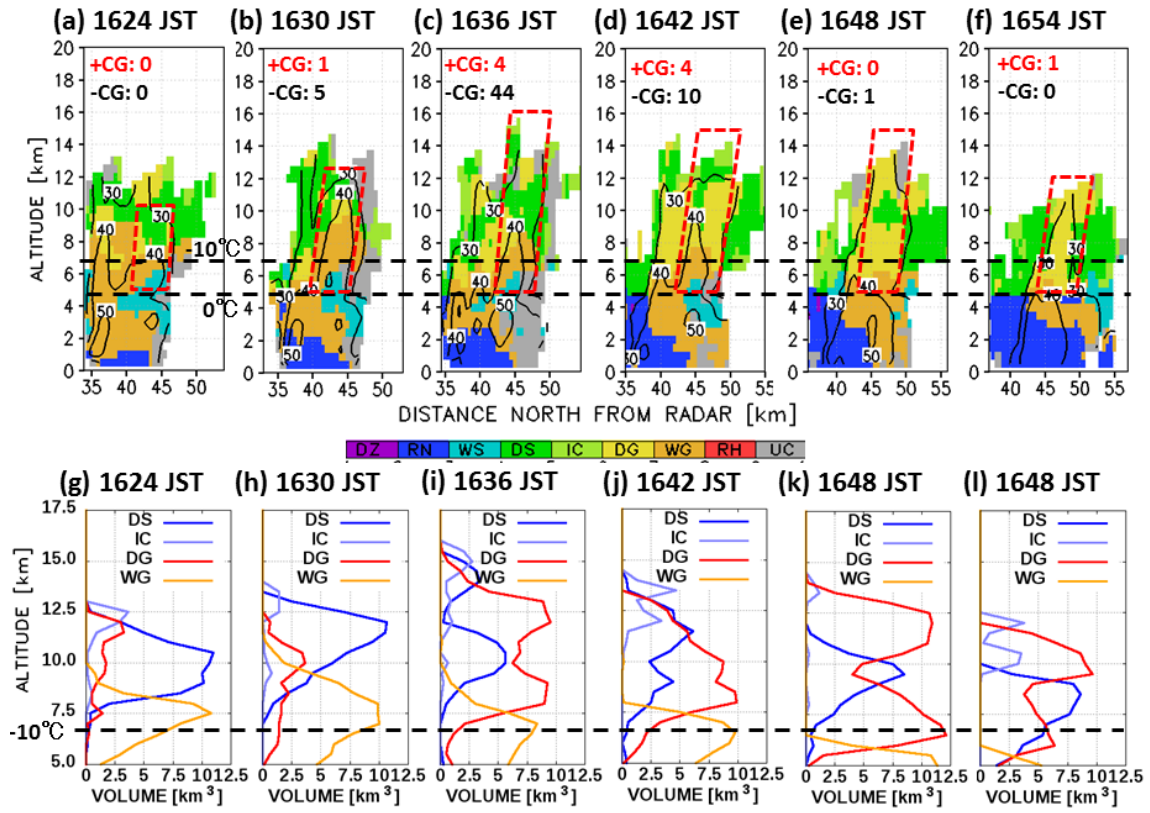


Fig. 33. Same as Fig. 27, but for reflectivity core B4 every 6 minutes from 1624 to 1654 JST on 25 August 2010.

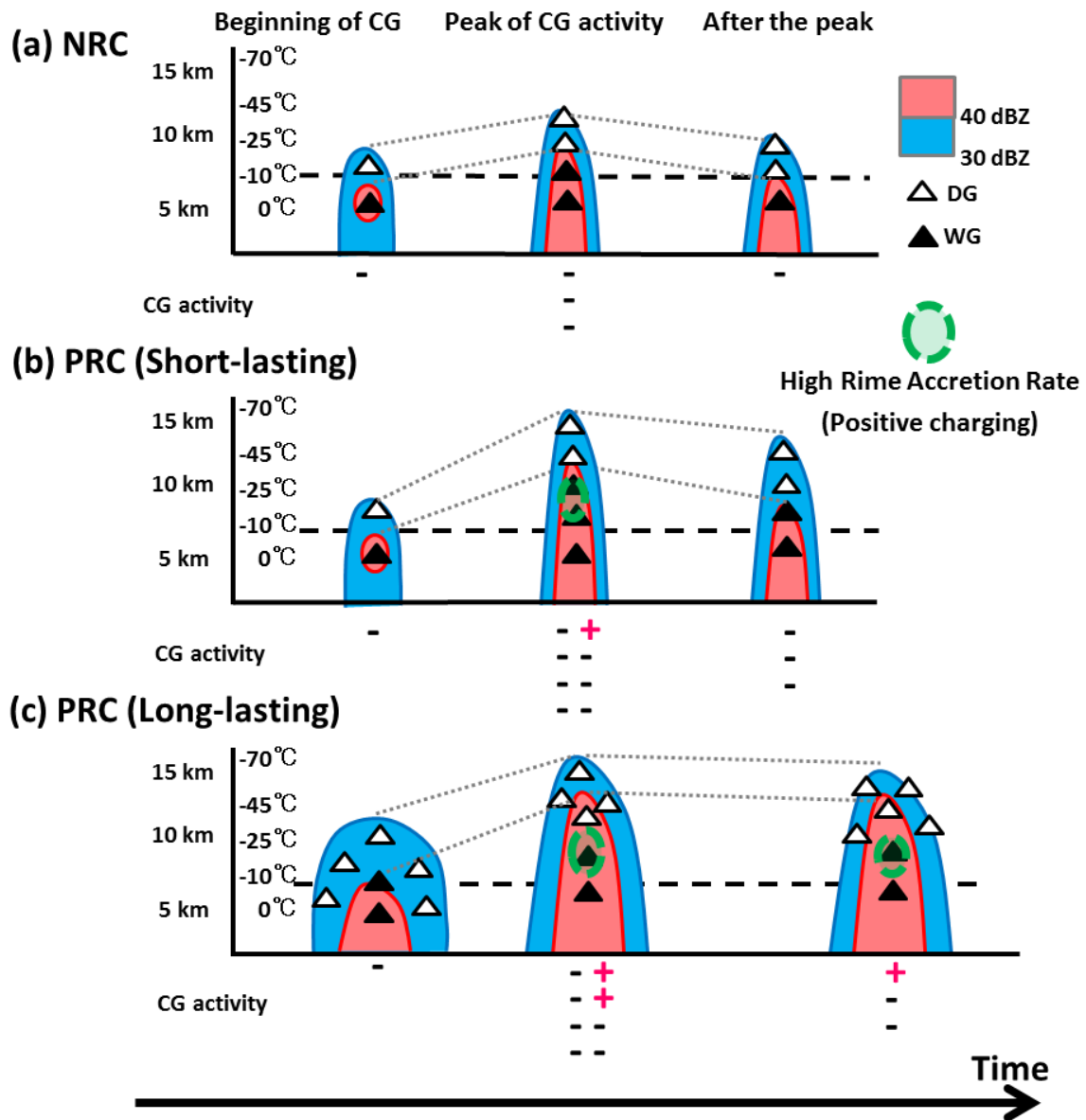


Fig. 34. Conceptual diagram of: (a) NRC, (b) relatively short-lasting PRC with a few positive CG strikes, and (c) relatively long-lasting PRC with several positive CG strikes. Colors show radar reflectivity and horizontal dashed lines indicate the -10°C level. The distributions of DG and WG are indicated by open and closed triangles, respectively. The inferred high rime accretion rate area, resulting in positively charged graupel particles and positive CG strikes, is shaded green enclosed by green dashed ellipses.

Positive and negative CG strikes for each stage are indicated by “+” and “–” symbols, respectively.